Astronomy Letters, Vol. 30, No. 4, 2004, pp. 209–217. Translated from Pis'ma v Astronomicheskiĭ Zhurnal, Vol. 30, No. 4, 2004, pp. 243–252.

Optical and Infrared Monitoring of BL Lac in 1999–2001

V. A. Hagen-Thorn[1], V. M. Larionov[1]*, E. G. Larionova[1], N. A. Kudryavtseva[1], A. V. Tikhonov[1], A. V. Hagen-Thorn[1], A. A. Arkharov[2], A. Di Paola[3], and F. d'Alessio[3]

[1] *Astronomical Institute, St. Petersburg State University, Universitetskiĭ pr. 28, Petrodvorets, 198504 Russia*

[2] *Pulkovo Astronomical Observatory, Russian Academy of Sciences, Pulkovskoe shosse 65, St. Petersburg, 196140 Russia*

[3] *INAF—Rome Astronomical Observatory, Via Frascati 33, Monteporzio Catone (Rome), I-00040 Italy*

Received July 10, 2003

Abstract—We present the results of our multicolor observations of BL Lac in the period 1999–2001. We show that the spectral energy distribution of the variable component in the range from K to B had remained unchanged for three years. The power-law spectrum is indicative of its synchrotron nature. © *2004 MAIK "Nauka/Interperiodica".*

Key words: *BL Lac, multicolor observations.*

INTRODUCTION

BL Lac is one of the most intensively observed blazars. It has been monitored photographically (mainly in the B band) since the 1960s at several observatories, in particular, at the Astronomical Institute of St. Petersburg State University (AI SPbSU). A combined light curve of BL Lac for the period 1968–1991 was constructed and repeatedly studied for periodicity (Hagen-Thorn *et al.* 1997, 2002a). With the advent of CCD detectors in the 1990s, most of the monitoring observations have been carried out in the V and R bands.

Multicolor ($UBVRI$) observations made, in particular, during international observing programs, are available for certain time intervals. Their analysis shows (see, e.g., Hagen-Thorn *et al.* 1990, 2000) that sources with power-law spectra are responsible for the variability on intermediate time scales (from weeks to months). These sources are most likely of a synchrotron nature, because BL Lac almost always exhibits a high polarization of its light (Hagen-Thorn *et al.* 2002b).

However, many questions still remain to be answered. The connection between the optical and infrared variable sources is not quite clear; the details of the spectroscopic variability and the time scales of these variations have not been ascertained. Multicolor monitoring can give answers to these questions. At the AI SPbSU, the monitoring of BL Lac, which was forcedly interrupted in 1991, was resumed in 1999 as multicolor monitoring. Here, we present the results of our 1999–2001 observations and their analysis.

OBSERVATIONS AND DATA REDUCTION

We performed the optical $BVRI$ observations of BL Lac with a CCD photometer of the AI SPbSU equipped with an ST-7 camera attached to the 20-cm (1999) and 70-cm (2000–2001) telescopes at the Crimean Astrophysical Observatory. To derive equations for transforming instrumental magnitudes to the standard BVR_cI_c system, we used the observations of comparison stars for the object 4U0115 + 63 that spanned a wide range of color indices and that were accurately measured by Negueruela *et al.* (1997). The magnitudes of the comparison stars for BL Lac (nos. 12, 16, 17, and 21) were taken from a paper by Gonzales-Perez *et al.* (2001), who also gave a finding chart.

To increase the photometric accuracy, we sequentially obtained several images (typically four or five) in each of the color bands and added them up when matching the stellar images with a subpixel accuracy. The frame reduction procedure consisted of flat fielding, the construction of a background surface for the whole frame, background subtraction, and flux summation within an 8″ field, irrespective of the seeing. The latter had a negligible effect on our estimates, because the size of a bright point source was always much smaller than the size of our field. We estimated the accuracy of our results from the scatter of data for the entire set of standard stars. In reducing the frames, we used original software developed by one

*E-mail: vml@VL1104.spb.edu

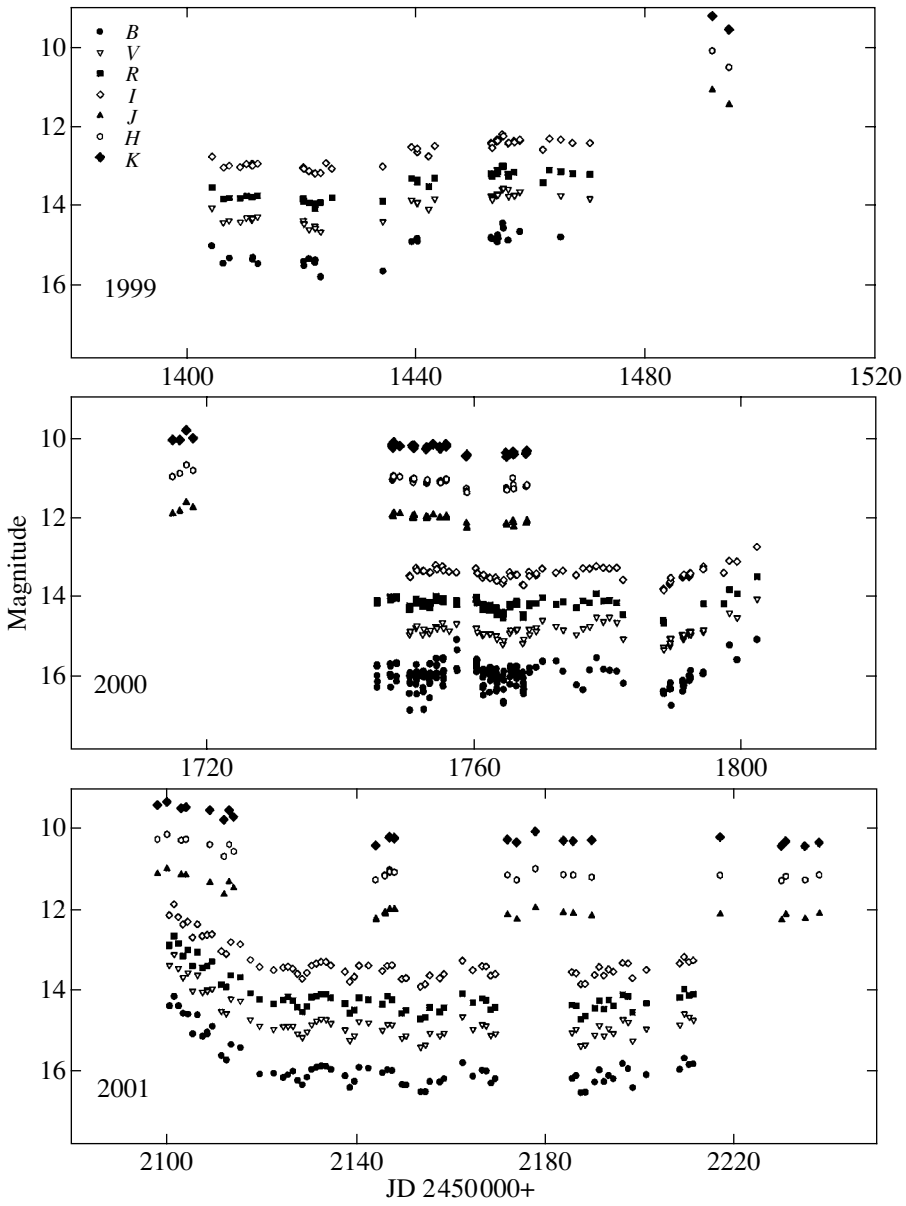

Fig. 1. Results of the optical and infrared photometry for BL Lac in 1999–2001.

of us. The error of individual magnitude estimates did not exceed $0^m.03$ in the B band and $0^m.02$ in the remaining color bands (in 1999, during our observations with the 20-cm telescope, the photometric error was $0^m.06$ in the B band and $0^m.04$ in the remaining bands).

We carried out the infrared (JHK) observations with the 1.1-m Pulkovo Astronomical Observatory (Russian Academy of Sciences) telescope installed at the Campo Imperatore Observatory (Italy) and equipped with the SWIRCAM camera. The instrumental system proved to be so close to the standard system that no corrections for the system were required. The magnitudes of the comparison stars were taken from the same paper by Gonzales-Perez *et al.* 2001). The frame reduction procedure and the corresponding software were the same as those for the optical observations.

RESULTS

The results of our optical observations are summarized in Table 1[1] and presented graphically in Fig. 1. We see that the variability amplitude is larger

[1] Table 1 is published in electronic form only and is accessible via ftp cdsarc.u-strasbg.fr/pub/cats/J (130.79.128.5) or http://cdsweb.u-strasbg.fr/pub/cats/J.

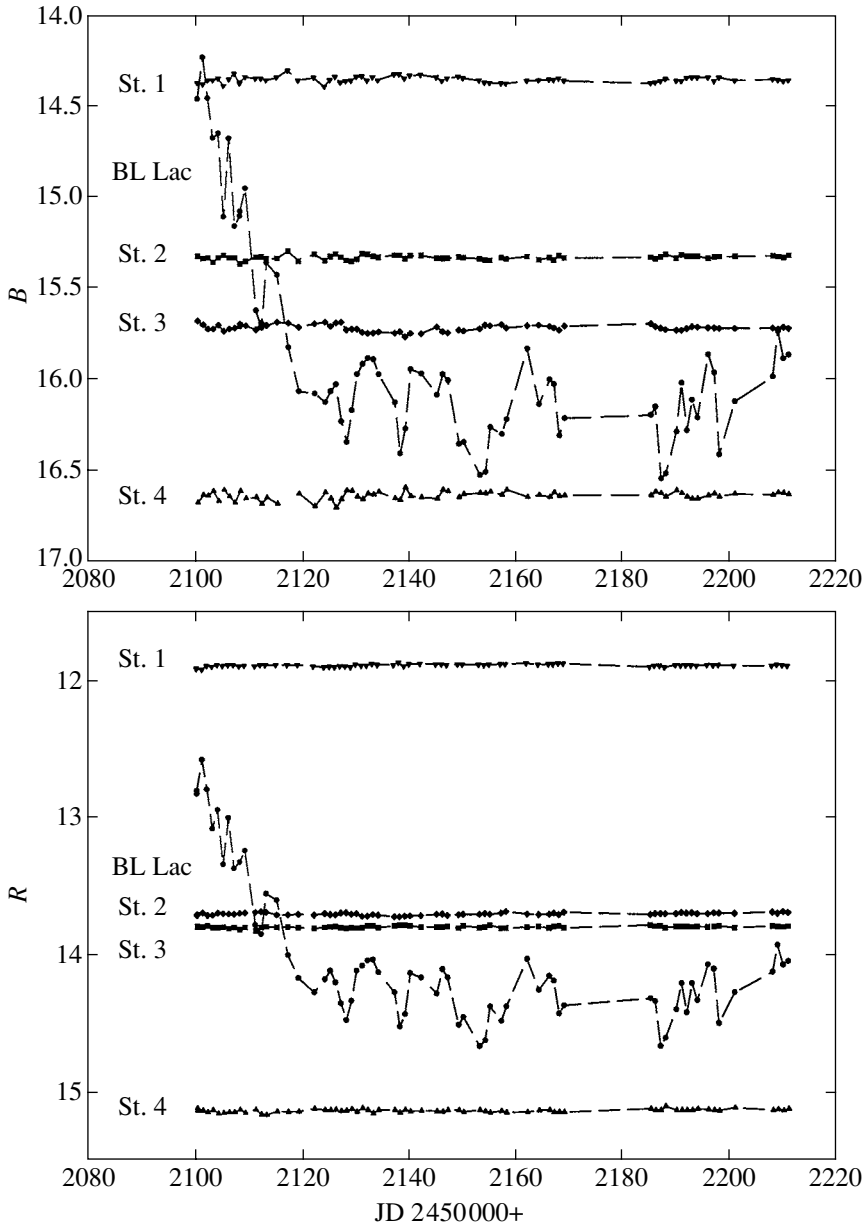

Fig. 2. B- and R-band photometry for BL Lac and the comparison stars in 2001.

at short wavelengths; for the three-year period, it is $2^m.69$ in B, $2^m.33$ in V, $2^m.11$ in R, and $2^m.07$ in I. For its comparison with the observational errors, Fig. 2 shows (as an example) the B and R light curves of BL Lac for 2001. The light curves of the comparison stars are also shown here. As we see from the figure, all the brightness variations of BL Lac should be accepted as real.

Our IR observations are given in Table 2 and graphically shown in Fig. 1. They are more scanty, but, in general, the tendency for the variability amplitude to decrease with increasing wavelength and the general run of the light curves are in agreement with the optical data.

An examination of Fig. 1 indicates that the brightness variations in all bands are synchronous; therefore, we will describe only the R light curve. After the giant outburst of BL Lac in 1997, when the brightness of the object reached $R = 12^m.40$, BL Lac was still rather bright (between $13^m.9$ and $13^m.0$) in 1999, with its brightness peaking shortly before the end of our observations. At the beginning of the 2000 observing season, BL Lac was fainter (between $14^m.4$ and $14^m.0$) and exhibited no activity in August, during an international observing program (Villata

Table 2. Infrared photometry for BL Lac

JD 2450000+	*J*	JD 2450000+	*H*	JD 2450000+	*K*
1491.8500	11.10	1491.8500	10.12	1491.8600	9.24
1494.7500	11.47	1494.7500	10.53	1494.7600	9.58
1715.0100	11.89	1715.0200	10.96	1715.0200	10.05
1716.0900	11.82	1716.0900	10.89	1716.0900	10.05
1717.0600	11.61	1717.0700	10.68	1717.0700	9.80
1718.0700	11.73	1718.0700	10.82	1718.0700	10.00
1747.8600	11.93	1747.8600	11.06	1747.8700	10.22
1747.9400	11.97	1747.9500	11.03	1747.8800	10.17
1747.9400	11.97	1748.0300	10.96	1747.9500	10.25
1748.0700	11.88	1748.0400	11.00	1748.0500	10.17
1748.9900	11.89	1748.0700	10.97	1748.0800	10.12
1750.8900	12.00	1748.9800	10.98	1748.9800	10.22
1750.9000	11.96	1750.8900	11.05	1750.8900	10.20
1750.9400	12.03	1750.9400	11.10	1750.9700	10.25
1751.0300	12.00	1750.9700	11.12	1751.0300	10.24
1751.0900	11.95	1751.0300	11.03	1751.0900	10.26
1751.1200	11.94	1751.0900	11.04	1751.1200	10.20
1752.9500	11.98	1751.1200	11.02	1752.9600	10.29
1753.0000	12.02	1752.9600	11.13	1753.0100	10.25
1753.0700	12.01	1753.0100	11.14	1753.0600	10.27
1753.1100	11.98	1753.0600	11.11	1753.9800	10.17
1753.9900	11.93	1753.1100	11.06	1754.9600	10.24
1754.9700	12.00	1754.9600	11.11	1755.0600	10.28
1755.0500	12.00	1755.0600	11.08	1755.1100	10.27
1755.1100	12.02	1755.1100	11.13	1755.9200	10.22
1755.9100	11.99	1755.9200	11.08	1755.9300	10.17
1755.9300	12.00	1755.9300	11.04	1755.9900	10.21
1755.9800	11.96	1755.9900	11.04	1758.9500	10.47
1758.9600	12.13	1758.9600	11.28	1758.9600	10.47
1758.9700	12.26	1758.9700	11.34	1759.0300	10.44
1759.0300	12.24	1759.0300	11.37	1764.9000	10.39
1764.9100	12.14	1764.9100	11.25	1764.9900	10.48
1764.9900	12.19	1764.9900	11.30	1765.9200	10.38
1765.9100	12.07	1765.0400	11.32	1765.9900	10.36
1766.0000	12.12	1765.9200	11.02	1766.0600	10.42
1766.0500	12.23	1766.0000	11.18	1767.9000	10.40
1767.9100	12.14	1766.0600	11.29	1768.0400	10.34
1767.9500	12.10	1767.9100	11.23	2098.0200	9.38

Table 2. (Contd.)

JD 2450000+	J	JD 2450000+	H	JD 2450000+	K
1768.0400	12.07	1768.0400	11.19	2100.0400	9.29
2098.0200	11.07	2098.0200	10.22	2103.0200	9.46
2100.0300	10.95	2100.0300	10.10	2104.0000	9.43
2103.0200	11.10	2103.0200	10.24	2109.0100	9.51
2104.0100	11.11	2104.0000	10.22	2111.9900	9.75
2109.0100	11.30	2109.0000	10.36	2113.0700	9.50
2111.9800	11.58	2111.9900	10.64	2114.0000	9.68
2113.0600	11.28	2113.0600	10.35	2144.0600	10.39
2114.0000	11.43	2114.0000	10.52	2146.9500	10.19
2144.0100	12.20	2143.9800	11.24	2146.9800	10.18
2144.0400	12.23	2143.9900	11.24	2147.0000	10.19
2145.9600	12.04	2145.9600	11.12	2147.9600	10.22
2145.9700	12.05	2145.9800	11.14	2147.9800	10.22
2145.9900	12.06	2146.9300	10.99	2148.0000	10.20
2146.0000	12.05	2146.9600	11.06	2171.9600	10.25
2146.0100	12.08	2146.9800	11.04	2173.9200	10.32
2146.0200	12.06	2147.9500	11.06	2177.8800	10.06
2146.9500	11.98	2147.9700	11.06	2183.7700	10.28
2146.9700	11.98	2147.9900	11.05	2185.8700	10.29
2147.0000	11.97	2171.9600	11.13	2189.7700	10.27
2147.9600	11.97	2173.9200	11.25	2216.9200	10.20
2147.9700	11.98	2177.8700	10.97	2229.7900	10.42
2148.0000	11.96	2183.7700	11.12	2230.7100	10.31
2171.9600	12.11	2185.8700	11.13	2234.7300	10.43
2173.9100	12.22	2189.7700	11.18	2237.7300	10.34
2177.8700	11.94	2216.9100	11.14	2392.1400	10.09
2183.7700	12.06	2229.7800	11.28	2407.1300	10.27
2185.8600	12.08	2230.7100	11.18	2410.0800	10.37
2189.7600	12.14	2234.7300	11.26	2412.1300	10.28
2216.9100	12.11	2237.7300	11.14		
2229.7800	12.25	2392.1300	10.94		
2230.7100	12.12	2407.1300	11.10		
2234.7300	12.22	2410.0800	11.22		
2237.7200	12.10	2412.1300	11.11		
2392.1300	11.82				
2407.1300	12.02				
2410.0700	12.18				
2412.1200	12.06				

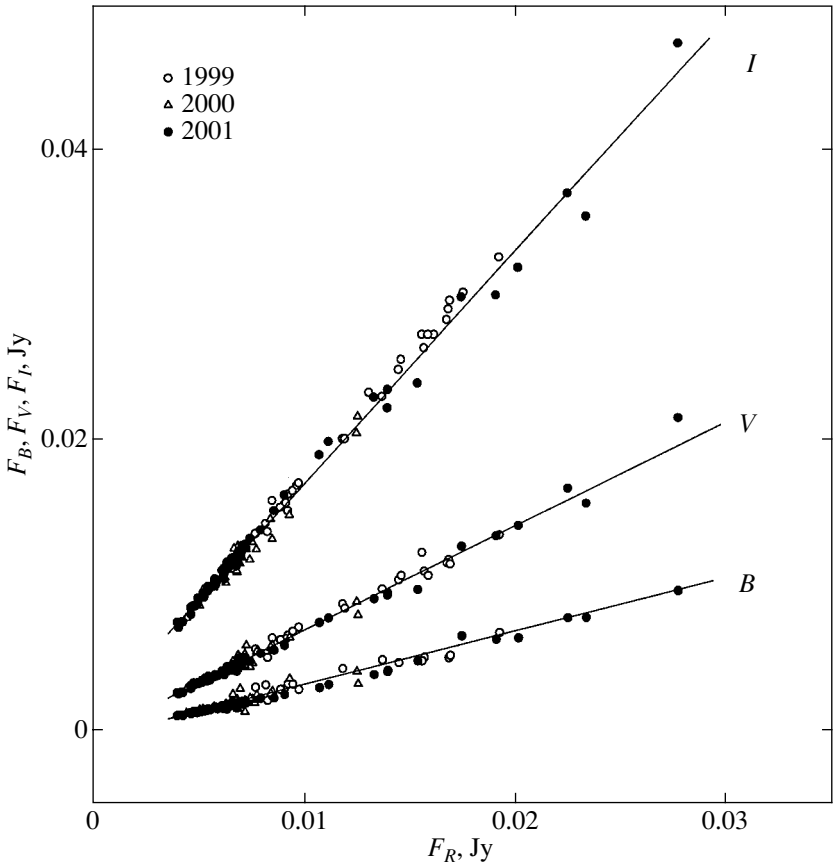

Fig. 3. Flux–flux diagrams for the optical wavelength range.

et al. 2002). However, an outburst began in the autumn, and the object brightened to $13^m.1$. BL Lac was very bright ($12^m.7$) at the beginning of the 2001 observing season. Subsequently, the object faded to $14^m.5$, but again brightened to $14^m.0$ by the end of the season (the brightness variations in 2001 are more clearly seen in Fig. 2).

ANALYSIS OF THE COLOR VARIABILITY

The technique for analyzing the color variability was described in detail by Hagen-Thorn and Marchenko (1999). Its essence is the construction of flux–flux (more precisely, flux density) diagrams for a pair of bands on which the data points, if the color characteristics of the variable component are invariable, must lie on straight lines whose slopes give the flux ratios of the *variable* component in the bands under consideration. Thus, multicolor observations of the variability yield the relative spectral energy distribution of the variable source.

If the spectral energy distribution of the variable source changes with time, then this technique makes it possible to establish whether these changes are present from deviations of the data points from the straight lines and to reach qualitative conclusions about the spectral evolution of the variable component, but does not allow its spectral energy distribution to be determined. In most cases, however, there are no deviations of the data points from the straight lines on fairly long time scales.

It is convenient to determine the energy distribution of the variable source separately for the optical and IR ranges. These distributions are then joined by using the flux–flux diagram on which the fluxes in one of the optical bands and one of the IR bands are compared.

The band in which the largest number of observations is available is usually taken as the main band in each of the ranges. In our case, these are the R and J bands. We will use the flux–flux diagram for these bands to join the spectra.

We transformed magnitudes to fluxes by using the calibration from Mead *et al.* (1990). After averaging all magnitude estimates in all bands for a given Julian date (here, we disregard the possible ultrafast variability), we constructed flux–flux diagrams for the optical (Fig. 3) and infrared (Fig. 4) spectral ranges. Different symbols indicate the data for different seasons. We immediately see that if there

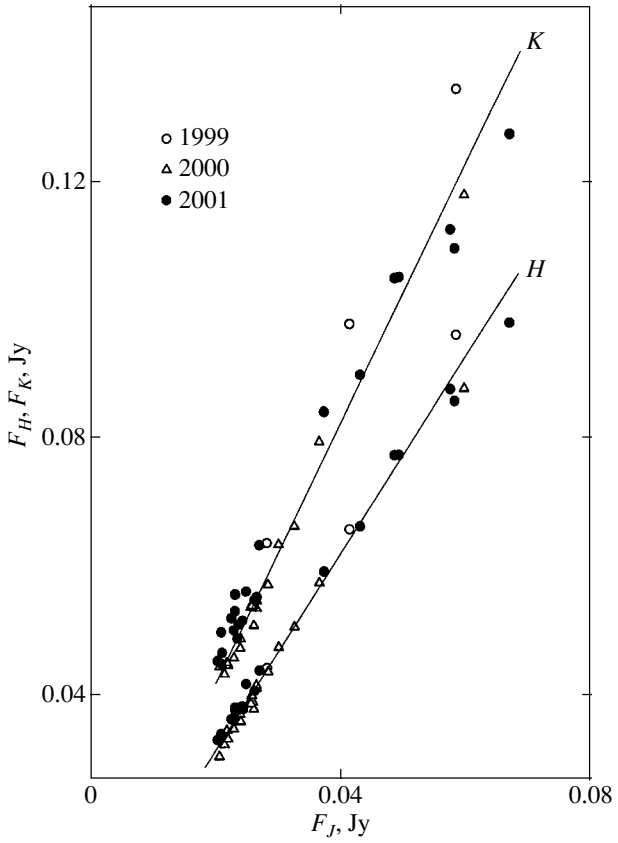

Fig. 4. Flux–flux diagrams for the infrared wavelength range.

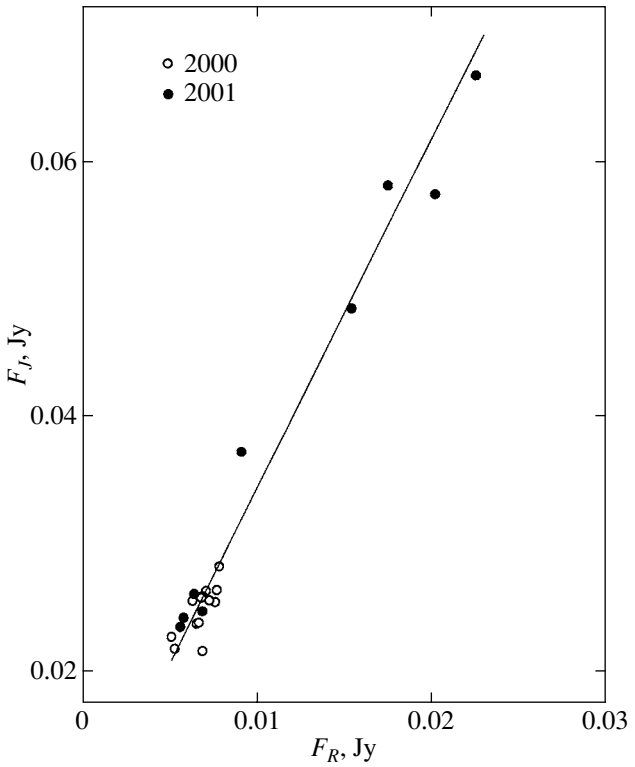

Fig. 5. Flux–flux diagram for the R and J bands.

are systematic differences between the data for different seasons, they are small. In general, the data points fall nicely on the straight lines. The correlation coefficients are close to unity in all cases (see Table 3). Drawing the straight lines by the orthogonal regression method, which is used when there are random errors in both quantities being compared, determines the *observed* relative spectral energy distribution of the variable component separately in the optical ($\alpha_{iR} = (F_i/F_R)^{\rm obs}_{\rm var}$ and IR ($\alpha_{iJ} = (F_i/F_J)^{\rm obs}_{\rm var}$) spectral ranges. By comparing the R and J fluxes (Fig. 5), we can find the flux ratio of the variable source in these bands, $(F_J/F_R)^{\rm obs}_{\rm var}$, and relate the IR spectrum to the optical spectrum. The results of our computations for the entire set of observational data are presented in Table 3. Column 3 gives the correlation coefficients in the flux–flux diagrams (for the H and K bands, r_{HJ} and r_{KJ}); column 4 contains the number of observations; column 5 lists the slopes of the straight lines, $\alpha_{iR} = (F_i/F_R)^{\rm obs}_{\rm var}$, and their 1σ errors; and column 6 contains the logarithms of these ratios, whose comparison with $\log\nu$ gives the *observed* relative spectral energy distribution of the variable source shown in Fig. 6 (filled circles). This distribution appears smooth, with a drop toward shorter wavelengths.

BL Lac has a low Galactic latitude ($b = -12^\circ$), and, according to Smith *et al.* (1989), the total visual extinction for it is $A_V = 1\overset{m}{.}33$. Therefore, the observed distribution should be corrected for the interstellar reddening. This can be done by introducing correction factors c_{iR} into the ratios $(F_i/F_R)^{\rm obs}_{\rm var}$, so that $(F_i/F_R)^{\rm corr}_{\rm var} = c_{iR}(F_i/F_R)^{\rm obs}_{\rm var}$.

The derived values of c_{iR} are listed in the last column of Table 4, where column 2 gives the effective wavelengths of the bands λ_e, column 3 gives the interstellar reddening curve $\tau_{\lambda e}$ for $R = A_V/E_{B-V} = 3.5$ from Cardelli *et al.* (1989), column 4 contains the extinction (in magnitudes), and column 5 lists the ratios of the corrected flux to the observed flux.

The reddening-corrected ratios $(F_i/F_R)^{\rm corr}_{\rm var}$ are listed in the next to last column of Table 3; the last column gives their logarithms. The reddening-corrected relative spectral energy distribution of the variable component is shown in Fig. 6 (open circles). We see that the distribution lost some of its smoothness (the points for the I and J bands deviate from the general pattern). This is probably due to the inaccurate reddening curve by Cardelli *et al.* (1989), since one can hardly assume that the true distribution

Table 3. Results of our analysis of the color variability

Band	$\log\nu$	r_{iR}	n	$(F_i/F_R)^{\rm obs}_{\rm var}\pm1\sigma$	$\log(F_i/F_R)^{\rm obs}_{\rm var}\pm1\sigma$	$(F_i/F_R)^{\rm corr}_{\rm var}$	$\log(F_i/F_R)^{\rm corr}_{\rm var}$
B	14.833	0.978	119	0.352 ± 0.010	-0.453 ± 0.013	0.640	−0.194
V	14.736	0.988	123	0.736 ± 0.007	-0.133 ± 0.004	0.883	−0.054
R	14.670	1.0	128	1.000	0.000	1.000	0.000
I	14.574	0.991	128	1.632 ± 0.006	0.213 ± 0.002	1.257	0.099
J	14.387	0.933	23	2.827 ± 0.033	0.451 ± 0.005	1.442	0.159
H	14.262	0.987	43	4.249 ± 0.043	0.628 ± 0.005	1.912	0.281
K	14.140	0.967	44	5.702 ± 0.050	0.756 ± 0.004	2.338	0.369

is not smooth and has just the shape that, together with the reddening curve, gives a smooth curve.

The corrected distribution in the range from K to V can be fitted by a straight line; i.e., the energy distribution may be considered to be a power law. Its spectral index is 0.65 ± 0.02. Of course, the spectral index depends on the adopted V-band extinction. We also used $A_V=1^m\!.33$ previously when analyzing the color variability of BL Lac (Hagen-Thorn *et al.* 1990, 2000). Thus, we can make a comparison with previous results for other time intervals.

DISCUSSION AND CONCLUSIONS

The power-law spectrum in the range from K to V and the high polarization commonly observed in BL Lac (Hagen-Thorn *et al.* 2002b) lead us to conclude that the source responsible for the variability of BL Lac in the period 1999–2001 has a synchrotron nature.

The point for the B band lies below the straight line. The high-frequency turnover may begin here, indicating that the frequency of the B band is close to critical ($\nu_{\rm c}=\text{const}\times H_\perp E^2_{\rm max}$). A similar fact was pointed out by Hagen-Thorn *et al.* (1990) when analyzing the data for 1983–1984.

Table 4. Corrections for the interstellar reddening

Band	λ_e, μm	τ_{λ_e}	A_i	$F^{\rm corr}/F^{\rm obs}$	c_{iR}
B	0.44	1.287	1.72	4.875	1.72
V	0.55	1.000	1.33	3.404	1.20
R	0.64	0.852	1.13	2.831	1.00
I	0.79	0.633	0.84	2.168	0.77
J	1.25	0.296	0.39	1.432	0.51
H	1.65	0.193	0.26	1.271	0.45
K	2.20	0.119	0.16	1.159	0.41

Our results concerning the color variability can be compared with those published previously for the weak outburst of 1983–1984 and the strong outburst of 1997 (Hagen-Thorn *et al.* 2000) only for the optical (the bands from B to I) spectral range. Here, the spectral index for 1999–2001 is $\alpha=1.25$. This value is approximately the same as that derived for the outburst of 1997 (in 1983–1984, the spectrum was much steeper, $\alpha=1.62$).

Hagen-Thorn *et al.* (1998) pointed out that the spectral slope for another blazar, OJ 287, changed from event to event, but within the events with a duration reaching several years, the spectral energy distribution remained unchanged. The same pattern probably also holds for BL Lac, and the 1999–2001 data pertain to the event that began in 1997. The constancy of the energy distribution in the course of smooth variations during the BL Lac observing campaign in 2000 was also noted by Villata *et al.* (2002).

Using the technique described by Hagen-Thorn *et al.* (2000), we estimated the flux from the constant component in the radiation from BL Lac in 1999–2001. Within the error limits, the results do not differ from those for 1997 (the $BVRI$ fluxes, in mJy, were found to be 0.26, 1.07, 2.15, and 4.20 from the 1999–2001 data and, respectively, 0.26, 0.96, 1.84, and 3.77 from the 1997 data). This result is consistent with the assumption that the lifetime of the variable component is several years.

CONCLUDING REMARKS

Although, in general, the spectrum in the K–V range can be fitted by a straight line, the difference between the individual spectral slopes for the optical ($\alpha=1.25$) and infrared ($\alpha=0.90$) spectral ranges does not allow us to ultimately resolve the question of whether the same variable source is acting in the IR and optical spectral ranges. More extensive (especially in the infrared) and better coordinated observations in these two spectral ranges are needed to resolve this question.

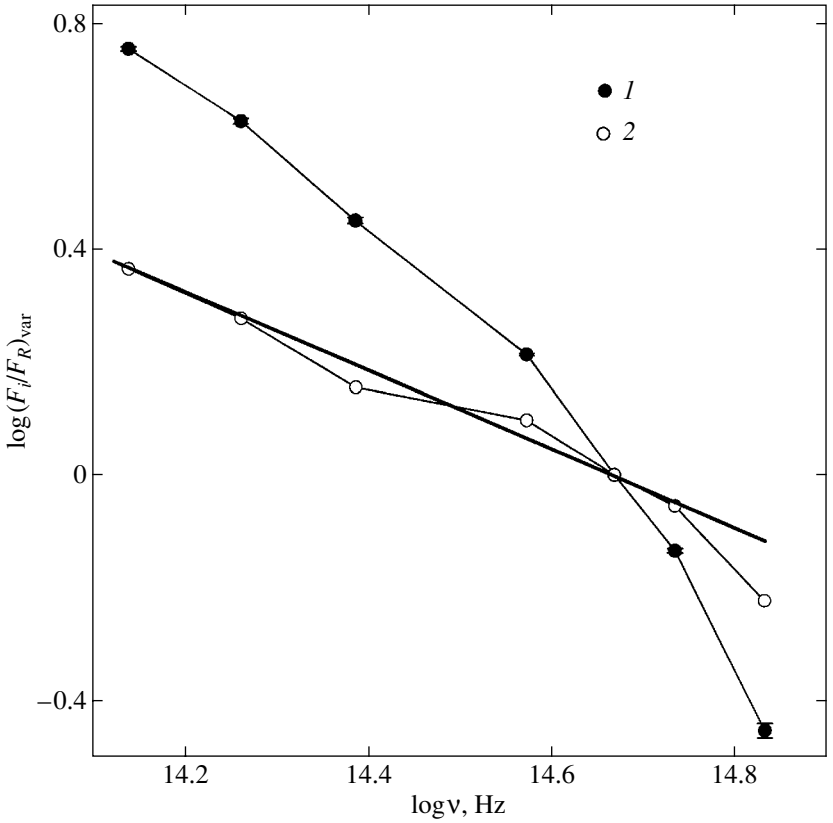

Fig. 6. Observed (*1*) and reddening-corrected (*2*) relative spectral energy distributions of the variable component.

ACKNOWLEDGMENTS

This study was supported by the federal Astronomy and Integration programs (projects no. 40.022.1.1.1001 and B0029, respectively). V.M. Larionov and A.A. Arkharov are grateful to the Rome and Teramo Observatories for the opportunity to carry out IR observations in Campo Imperatore.

REFERENCES

1. J. A. Cardelli, G. C. Clayton, and J. S. Mathis, Astrophys. J. **345**, 245 (1989).
2. J. N. Gonzales-Perez, M. R. Kidger, and F. Martin-Luis, Astron. J. **122**, 2055 (2001).
3. V. A. Hagen-Thorn and S. G. Marchenko, Baltic Astron. **8**, 575 (1999).
4. V. A. Hagen-Thorn, S. G. Marchenko, and O. V. Mikolaichuk, Astrofizika **32**, 429 (1990).
5. V. A. Hagen-Thorn, S. G. Marchenko, O. V. Mikolaichuk, and V. A. Yakovleva, Astron. Zh. **74**, 177 (1997) [Astron. Rep. **41**, 154 (1997)].
6. V. A. Hagen-Thorn, S. G. Marchenko, L. O. Takalo, *et al.*, Astron. Astrophys., Suppl. Ser. **133**, 353 (1998).
7. V. A. Hagen-Thorn, A. V. Gagen-Torn, S. G. Marchenko, and O. V. Mikolaichuk, Astrofizika **43**, 175 (2000).
8. V. A. Hagen-Thorn, V. M. Larionov, S. G. Jorstad, and E. G. Larionova, Astron. J. **124**, 3031 (2002a).
9. V. A. Hagen-Thorn, E. G. Larionova, S. G. Jorstad, C.-I. Björnsson, and V. M. Larionov, Astron. Astrophys. **385**, 55 (2002b).
10. A. R. J. Mead, K. R. Ballard, P. W. J. L. Brand, *et al.*, Astron. Astrophys., Suppl. Ser. **83**, 183 (1990).
11. I. Negueruela, J. E. Crove, M. J. Coe, *et al.*, Mon. Not. R. Astron. Soc. **284**, 859 (1997).
12. P. S. Smith, T. J. Balonek, R. Elston, and P. A. Heckert, Astrophys. J., Suppl. Ser. **64**, 459 (1987).
13. M. Villata, C. M. Raiteri, O. M. Kurtanidze, *et al.*, Astron. Astrophys. **390**, 407 (2002).

Translated by N. Samus'

Astronomy Letters, Vol. 30, No. 4, 2004, pp. 218–231. Translated from Pis'ma v Astronomicheskiĭ Zhurnal, Vol. 30, No. 4, 2004, pp. 253–267.

Phaseless VLBI Mapping of Compact Extragalactic Radio Sources

A. T. Bajkova*

Institute of Applied Astronomy, Russian Academy of Sciences, nab. Kutuzova 10, St. Petersburg, 191187 Russia

Received June 23, 2003

Abstract—The problem of phaseless aperture synthesis is of current interest in phase-unstable VLBI with a small number of elements when either the use of closure phases is not possible (a two-element interferometer) or their quality and number are not enough for acceptable image reconstruction by standard adaptive calibration methods. Therefore, we discuss the problem of unique image reconstruction only from the spectrum magnitude of a source. We suggest an efficient method for phaseless VLBI mapping of compact extragalactic radio sources. This method is based on the reconstruction of the spectrum magnitude for a source on the entire UV plane from the measured visibility magnitude on a limited set of points and the reconstruction of the sought-for image of the source by Fienup's method from the spectrum magnitude reconstructed at the first stage. We present the results of our mapping of the extragalactic radio source 2200+420 using astrometric and geodetic observations on a global VLBI array. Particular attention is given to studying the capabilities of a two-element interferometer in connection with the putting into operation of a Russian-made radio interferometer based on Quasar RT-32 radio telescopes.

Key words: *astronomical observing techniques, devices and instruments.*

INTRODUCTION

The situation with uncertainty in measuring the phase due to ionospheric and troposheric inhomogeneity is typical of phase-unstable interferometry. Phase errors, let alone the fact that the phase is unknown, significantly restrict the signal and image processing quality (Oppenheim and Lim 1981). Many studies that are systematized in the monographs by Stark (1987) and Thompson *et al.* (1986) are devoted to the influence of phase errors.

In VLBI, adaptive calibration methods, including hybrid and self-calibration methods that directly or indirectly use closure phases (Cornwell and Fomalont 1999; Thompson *et al.* 1986), are traditionally used to solve the phase retrieval problem. The number of equations for closure phases depends on the number of interferometer elements N and is $(N-1)(N-2)/2$ at each instant in time. The larger the number of interferometer elements and the more the visibility measurements on each baseline, the higher the phase retrieval accuracy. In contrast, at a small number of elements and a small number of measurements, the number of equations for closure phases may prove to be insufficient for high-quality phase retrieval. For a two-element ($N = 2$) interferometer, there are no equations for closure phases at all.

Phase retrieval errors can give rise to spurious features. Thus, for compact extragalactic radio sources with a typical core + jet structure, a spurious symmetric counterjet can appear on the map. We encounter such a situation, for example, when mapping using astrometric and geodetic observations on a global VLBI array (IRIS, NEOS, etc.), as these are distinguished by relatively poor UV-filling (Bajkova *et al.* 1997).

The necessity of mapping based on astrometric data arises from the need to improve the coordinates of reference sources by taking into account their structure on milliarcsecond (mas) angular scales (Bajkova 2002a). Clearly, because of their spectral and temporal variability, the mapping of sources and the astrometric reduction should be performed using the same data. In addition, since the observations are regular (each source has been observed once a week for many years), they are also of considerable interest in astrophysics, providing unique data for investigating the structural evolution of extragalactic sources on long time scales (Pyatunina *et al.* 1998).

Thus, apart from adaptive calibration methods, phaseless mapping methods using only the visibility magnitude can also be invoked to overcome the phase uncertainty in VLBI, provided that the signal-to-noise is high enough for the application of reconstruc-

*E-mail: bajkova@gao.spb.ru

tion algorithms (see the section titled Reconstruction Accuracy).

Interest in phaseless VLBI mapping is also being aroused by the fact that the Institute of Applied Astronomy (Russian Academy of Sciences) has recently put into operation a two-element interferometer based on RT-32 radio telescopes of the Quasar VLBI project at the Svetloe Observatory near St. Petersburg and at the Zelenchuk Observatory in the North Caucasus and that the first preliminary mapping results have already been obtained (Bajkova 2002b).

In this paper, we present the results of our study of the capabilities of a two-element interferometer designed to map sources that can be represented as a set of compact components. The results of this study can also be applied to ground-based–spaceborne radio interferometers with the high orbit of a space station (Finkelstein and Bajkova 1990).

The problem of aperture image synthesis without invoking phase information was first considered and solved by Baldwin and Warner (1976, 1978). However, these authors suggested methods that were applicable only in special cases where a source could be represented as a limited number of point components and, therefore, were not widely used in VLBI.

Here, our goal is to develop a more universal and efficient phaseless image synthesis method that can be used for the VLBI mapping of extragalactic radio sources, including those with a core + jet structure, that, apart from compact components (core), also contain extended components (jet); to study the capabilities of a two-element interferometer; and to demonstrate the potentialities of the suggested methods by mapping the well-known source 2200+420 using astrometric and geodetic observations on a global VLBI array as an example.

THE UNIQUENESS OF THE SOLUTION

In the most general formulation where constraints are imposed only on the spectrum magnitude, the problem of reconstructing the function has an infinite set of solutions. Indeed, any function that has a given spectrum magnitude and an arbitrary spectral phase satisfies these constraints, and, if at least one solution is known, the other can be obtained by convolving this solution with a function that has an arbitrary phase and a spectrum magnitude equal to unity at all frequencies.

However, a significant narrowing of the set of solutions is possible for certain constraints imposed on the function being reconstructed in the spatial domain (Stark 1987). One of these is the constraint imposed on the spatial extent of an object; i.e., the sought-for function must have a finite carrier. Another severe constraint in the spatial domain is the requirement that the solution be real and nonnegative. Below, in solving the phase retrieval problem, we assume that the sought-for function satisfies these constraints; i.e., it is real and nonnegative and has a finite extent.

The finite extent of an object (the finiteness of the function) ensures that the Fourier spectrum is analytic in accordance with the Wiener–Paley theorem (Khurgin and Yakovlev 1971). As a result, this spectrum can be reconstructed from the known part of it, which is used to reconstruct images from the visibility function measured on a limited set of points in the UV-plane. If we determine the class of equivalent functions to within a linear shift and reversal of the argument (rotation through 180°), then all of the functions that belong to this class have the same spectrum magnitude. The solution of the phase retrieval problem is assumed to be unique if it was determined to within the class of equivalent functions.

In the case of one-dimensional functions, even these severe constraints on finiteness and nonnegativity do not guarantee a unique reconstruction from the spectrum magnitude. As the dimensionality of the function increases ($n \geq 2$), a unique (to within the class of equivalent functions) solution becomes possible, except for the degenerate cases defined on the set of measure zero (Bruck and Sodin 1979; Hayes 1982). This follows from the qualitative difference between the properties of the z-transformations of one-dimensional and multidimensional sequences. For a unique solution to exist, the z-transformation must be irreducible, which is not achievable in principle in the one-dimensional case and almost always holds in the multidimensional case.

Since we deal with two-dimensional images in VLBI, we assume that the solution of the phase retrieval problem exists and is unique. However, the existence of a unique solution does not yet guarantee that the retrieval algorithms converge. The papers by Gerchberg and Saxton (1972) and Fienup (1978) are of greatest importance in developing the theory and algorithms of solving the phase retrieval problem. Fienup's algorithm and its modifications aimed at speeding up the convergence to the required solution (Fienup 1982) are most efficient in terms of their applications. Based on numerous simulations, we choose a hybrid input–output algorithm modified to ensure convergence (by specifying the initial approximation) and to prevent stagnation due to computational effects from the entire set of various modifications of Fienup's algorithm (Bajkova 1994, 1996).

A MODEL FOR THE STRUCTURE OF COMPACT EXTRAGALACTIC RADIO SOURCES

Before turning to a description of the suggested phaseless mapping method, let us consider simplified models for the structure of compact extragalactic radio sources and their spectrum magnitudes. The simplest approximation of a core + jet source structure is a model that consists of two point components. This model will be useful below when considering a two-element interferometer. Let the brightest component be located at the phase center of the map and be the core of the source (the optically thick base of the jet) and the second component (the optically thinner feature of the jet) have a lower brightness and be located at an angular distance of r mas with the position angle θ reckoned from north to south through east (clockwise). We will consider the relative brightnesses by assuming the core brightness to be equal to unity. Let the brightness of the second component be $A < 1$.

The complex visibility function of such a source when its individual components are represented as δ-functions is

$$V_1(u,v) = 1 + A\exp(2\pi i(u\xi_0 + v\eta_0)),$$

where $\xi_0 = r\sin\theta$ and $\eta_0 = r\cos\theta$ are the rectangular coordinates of the source.

The square of the visibility magnitude is

$$|V_1(u,v)|^2 = 1 + A^2 + 2A\cos\phi, \qquad (1)$$

where $\phi = 2\pi(u\xi_0 + v\eta_0)$.

Clearly, since $\cos\phi$ is even, the source that is symmetrical to the original source relative to the map center will have the same visibility magnitude. Therefore, image reconstruction from the visibility magnitude alone is possible to within rotation through 180°.

For a symmetrical source with brightness B of the symmetrical components and coordinates (ξ_0, η_0), $(-\xi_0, -\eta_0)$, the visibility magnitude is

$$|V_2(u,v)| = |1 + 2B\cos\phi|. \qquad (2)$$

Clearly, function (2) has singularities at zeros, and it cannot have an analytic continuation to the entire complex plane. In this case, the condition for the spectrum magnitude being analytic (the existence of all derivatives) is satisfied for $B < 1/2$, because the following representation is valid:

$$|V_2(u,v)| = 1 + 2B\cos\phi. \qquad (3)$$

Below, we are concerned only with the cases where the spectrum magnitude of the source is an analytic function; this is achieved only when the flux from the central component dominates over that from the remaining components of the source. This condition is almost always satisfied for real sources. A deviation from this condition is possible only in the case of baseline-by-baseline data editing.

The square of the visibility magnitude is

$$|V_2(u,v)|^2 = 1 + 4B\cos\phi + 4B^2\cos^2\phi. \qquad (4)$$

The maximum and minimum values of (2) and (4) are reached at $\cos\phi = 1$ and $\cos\phi = -1$, respectively. For $A = 2B$, the minima and maxima of (2) and (4) coincide. The difference between the squares of the visibility magnitudes for the two-component and the corresponding three-component sources under the condition $A = 2B$ is

$$\Delta(V^2(u,v)) = A^2 - A^2\cos^2\phi = A^2\sin^2\phi.$$

Clearly, a symmetrical object can be distinguished from an asymmetric object only due to this difference; the higher the relative brightness of the jet component A, the more reliable the uniqueness of the solution.

Let us now complicate the source model to a three-component one with relative brightnesses A_1 and A_2 of the compact jet features and coordinates (ξ_1, η_1) and (ξ_2, η_2), respectively. The square of the visibility magnitude for this model can be represented as the sum

$$|V(u,v)|^2 = 1 + (A_1^2 + 2A_1\cos\phi_1) + (A_2^2 + 2A_2\cos\phi_2) + 2A_1A_2\cos(\phi_1 - \phi_2), \qquad (5)$$

where $\phi_1 = 2\pi(u\xi_1 + v\eta_1), \phi_2 = 2\pi(u\xi_2 + v\eta_2)$.

The first term on the right-hand side of (5) represents the core, the second term represents the first component of the jet, the third term represents the second component of the jet, and the fourth term represents the mutual orientation of the second and third components that gives rise to additional components in the autocorrelation function with coordinates equal to the difference between the coordinates of the first and the second components of the jet.

It is easy to show that in the general case of an N-component source,

$$|V(u,v)|^2 = 1 + \sum_{i=1}^{N-1} A_i^2 + 2\sum_{i=1}^{N-1} A_i\cos\phi_i + 2\sum_{i=1}^{N-2}\sum_{j=i+1}^{N-1} A_iA_j\cos(\phi_i - \phi_j), \qquad (6)$$

where $\phi_i = 2\pi(u\xi_i + v\eta_i)$. In the case of extended features, the source is represented as a set of point sources specified in each pixel. The visibility function

of the corresponding symmetrical (relative to the center) source with relative brightnesses $B_i = A_i/2$ of the components is

$$|V(u,v)| = 1 + \sum_{i=1}^{N-1} 2B_i \cos\phi_i. \quad (7)$$

Discarding the terms of the second order of smallness from (6) for $A_i \ll 1$ (which is valid for most of the compact radio sources with the core much brighter than the components of the jet), we can roughly represent the visibility magnitude when the flux from the central component dominates (for $\sum_{i=1}^{N-1} A_i < 1$) as

$$|V(u,v)| \approx 1 + \sum_{i=1}^{N-1} A_i \cos\phi_i. \quad (8)$$

As we see, expressions (7) and (8) are identical, to within the discarded terms of the higher order of smallness. These terms are important in providing unique reconstruction of the mutual orientation of the jet components and in suppressing the symmetric counterjet that is present on the intermediate map with a zero spectral phase (see the next section).

As follows from expression (8), to the first approximation, each feature of an N-component source introduces a harmonic to the visibility magnitude whose amplitude, frequency, and phase are determined by the brightness, the distance from the center, and the position angle of the component, respectively.

DESCRIPTION OF THE METHOD

The algorithms for image reconstruction from the spectrum magnitude of an object, the most efficient of which are Fienup's algorithm and its various modifications, require knowledge of the entire input two-dimensional sequence of sampled points. In VLBI, however, the visibility function is measured only on a limited set of points in the UV-plane, revealing large unfilled areas and a diffraction-limited constraint. Therefore, prior reconstruction of the visibility magnitude on the entire UV-plane from a limited data set is required to successfully use existing reconstruction algorithms like Fienup's algorithm.

Thus, the suggested phaseless aperture synthesis method consists of the following steps: (1) prior reconstruction of the visibility magnitude (the object's spectrum) on the entire UV-plane, and (2) reconstruction of the sought-for image using Fienup's algorithm or its modifications (Fienup 1978, 1982; Bajkova 1994, 1996) from the spectrum magnitude reconstructed at the first step of the method. The first step is performed through the reconstruction of an intermediate image that satisfies the measured visibility magnitude and a zero phase. Clearly, the intermediate image is symmetric relative to the phase center of the map. The Fourier transform of the image obtained yields the spectrum magnitude of the source extrapolated to the region of the UV-plane where there are no measurements.

Recall that Fienup's algorithm is an iterative process of the passage from the spatial domain of an object to the spatial frequency domain and back (using the direct and inverse Fourier transforms) in an effort to use the input constraints on the spectrum magnitude of the object in the frequency domain and the constraints on its nonnegativity and finite extent in the spatial domain. The finite carrier within which the source is expected to be localized should be specified in the form of a rectangle centered at the coordinate origin, because the structure of the source may turn out to be symmetric. Fienup *et al.* (1982) estimated the size of the carrier from the autocorrelation function equal to the inverse Fourier transform of the square of the spectrum magnitude for the object. Very important advantages of Fienup's algorithm are its high stability against noise (Sanz and Huang 1983) (stability means that a small change in input data causes the solution to change only slightly) and high speed (due to the application of fast Fourier transform algorithms) compared to other algorithms. The various modifications of Fienup's algorithm aimed at increasing the reliability of its convergence were also developed by Bajkova (1994, 1996). These papers are devoted to the synthesis of the initial approximation that increases the reliability of the algorithm convergence and to the prevention of the algorithm stagnation due to computational effects.

The intermediate image can be reconstructed from the visibility magnitude by the standard method of analytic continuation of the spectrum using the nonlinear CLEAN deconvolution procedures or the maximum entropy method (MEM) (Cornwell *et al.* 1999). Therefore, an important requirement for the visibility magnitude is its analyticity. As we noted in the previous section, this condition is satisfied for most of the compact extragalactic radio sources if the flux from the central compact component dominates over the flux from the remaining fainter components.

Note an important point concerning the use of the maximum entropy method. In contrast to the CLEAN method: the solution based on the standard MEM is strictly positive, while the sought-for intermediate image with a zero spectral phase is generally alternating, taking on both positive and negative values; in addition, it is characterized by a wider effective carrier. For clarity, let us show this using the simple two-component model as an example:

Let us represent the visibility magnitude (1) for a two-component source as the following expansion into a series:

$$|V_1(u,v)| = \sqrt{1+2A\cos\phi+A^2}$$
$$= \sqrt{(1+A\cos\phi)^2+A^2\sin^2\phi}$$
$$= (1+A\cos\phi)\sqrt{1+x^2} = (1+A\cos\phi)$$
$$\times\left(1+\frac{x^2}{2}-\frac{1}{2}\frac{1}{4}x^4+\frac{1}{2}\frac{1}{4}\frac{3}{6}x^6-\frac{1}{2}\frac{1}{4}\frac{3}{6}\frac{5}{8}x^8+\ldots\right),$$

where $x^2 = A^2\sin^2\phi/(1+A\cos\phi)^2 < 1$.

Disregarding the terms higher than the fourth order of smallness and expanding $1/(1+A\cos\phi)$ into a Taylor series, we obtain the following representation in the form of an infinite trigonometric series with rapidly decreasing terms:

$$|V_1(u,v)| \approx (1+A\cos\phi) \quad (9)$$
$$+\frac{A^2}{2}\sin^2\phi(1-A\cos\phi+A^2\cos^2\phi$$
$$-A^3\cos^3\phi+\ldots) = \left(1+\frac{A^2}{4}+\frac{A^4}{16}\right)$$
$$+\left(A-\frac{A^3}{8}-\frac{A^5}{16}\right)\cos\phi-\frac{A^2}{4}\cos 2\phi$$
$$+\left(\frac{A^3}{8}+\frac{A^5}{32}\right)\cos 3\phi-\frac{A^4}{16}\cos 4\phi$$
$$+\frac{A^5}{32}\cos 5\phi-\ldots.$$

Clearly, each coefficient of the cosine in expansion (9) with a multiple argument $n\phi$ in the spatial domain is twice the amplitude of the point component and the component symmetric to it (relative to the center) with coordinates $(n\xi_i, n\eta_i)$ and $(-n\xi_i, -n\eta_i)$, respectively (see also (3)). The coefficients of the cosines with odd and even arguments are positive and negative, respectively, suggesting that the intermediate image is alternating.

It is easy to show that, in general, the intermediate image that corresponds to the spectrum magnitude of a finite object and a zero spectral phase is also an alternating function with a theoretically unbounded carrier (since $n = \infty$). In this case, the effective carrier of the intermediate image is much wider than the carrier of the object, which must be properly taken into account when reconstructing the intermediate image.

Thus, the positive definiteness of the intermediate image is indicative of a zero phase and, hence, a symmetry of the object, while the alternating property is indicative of a nonzero phase and, accordingly, an asymmetry of the object relative to the coordinate origin. Therefore, in general, since we have no prior knowledge of whether the sought-for source is symmetric, it would be improper to use the standard MEM with positive output to reconstruct the intermediate image. A MEM modification suitable for obtaining both positive and alternating solutions is required. A generalized MEM (GMEM) suitable for reconstructing functions of any form was developed by Bajkova (1992). In addition, in contrast to the MEM, the GMEM yields an unbiased solution and is more stable against noise in the data (Bajkova 2000).

It should be emphasized that the combination of the alternating property and spatial unboundedness of the intermediate image, on the one hand, and the constraints on the nonnegativity and finite sizes of the object carrier, on the other hand, ensure that the reconstruction of the sought-for image is unique.

Below, we present simulation results that confirm our conclusions. Let us turn to Fig. 1, which shows the following: (a) the source model that consists of two Gaussian components (the central component represents the core, and the second fainter and extended component represents the jet); (b) the contaminated image that corresponds to incomplete UV filling whose Fourier transform is equal to the visibility magnitude at the measured points and to zero at the points without measurements (the visibility function was generated with a signal-to-noise ratio of $\approx$10); (c) the intermediate image with a zero spectral phase reconstructed from the measured visibility function using the standard MEM with positive output; (d) the intermediate image with a zero spectral phase reconstructed using the GMEM with alternating output; (e) and (f) the images reconstructed using Fienup's algorithm from the previous MEM and GMEM images, respectively. On all maps, the lower level of the contour line corresponds to 0.2% of the peak value.

As we see from the maps, the GMEM properly reconstructed the intermediate image with both positive and negative values, which subsequently allowed us to accurately reconstruct the structure of the source and, hence, its spectral phase (to within rotation through 180°) using Fienup's algorithm. In contrast, the standard MEM algorithm with positive output yielded no desirable result: at the output of Fienup's algorithm, the structure of the source was found to be nearly symmetric (the spectral phase was virtually unreconstructed), which is in conflict with the original model (a). Thus, at the first step of our mapping method, only algorithms with alternating output, either CLEAN or GMEM, should be used to reconstruct the intermediate image with a zero spectral phase.

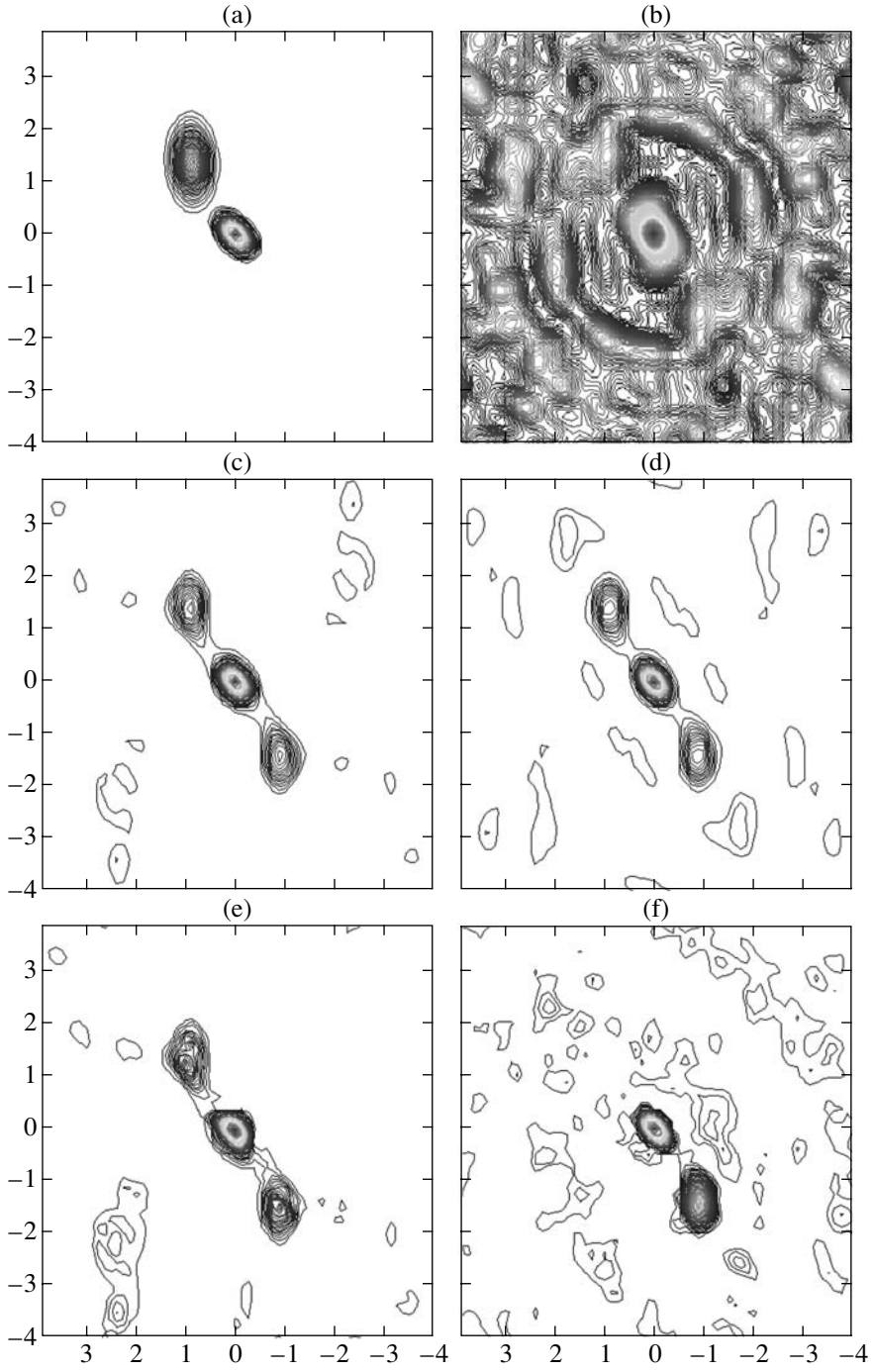

Fig. 1. Simulation of phaseless image reconstruction. Comparison of the reconstruction results when using the MEM and the GMEM (see the text).

An advantage of the suggested phaseless mapping method over the methods by Baldwin and Warner (1976, 1978) is the possibility of reconstructing sources that can be represented not only as a finite set of point components, but also sources with extended features, which makes the suggested method more efficient.

THE RECONSTRUCTION ACCURACY

For a given reconstruction method, the accuracy of the images being obtained depends on the following three major factors: (1) the structure of the source being mapped, (2) the UV filling (information on the various spatial frequencies of the source), and (3) the accuracy of the input data.

Clearly, the simpler the structure of a source at a given resolution (e.g., several (2 or 3) compact components with a low dynamic range), the less stringent the requirements for the *UV* filling and the signal-to-noise ratio of the measurements. The more complex the structure of a source (the presence of extended features against the background of compact features, a large number of components, and a high dynamic range), the more complete the filling of the spatial frequency domain (the presence of a low-frequency domain) and the higher the signal-to-noise ratio. General analytical expressions for estimating the image reconstruction accuracy are very difficult to derive by nonlinear methods, because the nonlinearity of the methods leads to nonlinear image distortions. Therefore, it would be appropriate to study the influence of various factors on the reconstruction accuracy by mathematical simulation for a large number of sources with various degrees of complexity of their structure, various *UV* fillings, and various specified data accuracies.

The accuracy of reconstructing the sought-for image by Fienup's method depends significantly on the accuracy of reconstructing the intermediate image or, in other words, on the spectrum magnitude of the sought-for image over the entire spatial frequency domain. Although Fienup's algorithms are highly stable against noise, significant distortions of the input data may lead to unpredictable nonlinear image distortions (the coordinates and amplitudes of the source's components), because the spectrum is no longer analytic. Distortions arise, because the spatial boundaries specified in Fienup's algorithm within which the solution is sought cease to correspond to the image being reconstructed. In these cases, the sizes of the carrier should be increased to reduce the distortions of the coordinates of the components. Our simulations of Fienup's hybrid input–output algorithms when the structure of sources is approximated by simple models show that the minimum signal-to-noise ratio of the input sampled points of the spectrum magnitude that does noticeably distort the coordinates of the compact components of the source, when the coordinates of the peak values of the components are taken as their coordinates, is about 5. In this case, the errors in the data were simulated as additive noise with a uniform distribution.

To achieve the required data quality at the output of the first step of the phaseless mapping method for typical core + jet structures of compact extragalactic radio sources and the *UV* filling obtained on VLBI arrays with a small number of elements (the cases that are the subject of discussion in this paper), the visibility magnitude must be measured with a signal-to-noise ratio of no less than 10. This accuracy is needed to reconstruct not only the positively defined, but also the negatively defined components of the intermediate image (see (9) for a two-component source), which are relatively small, but play a major role in suppressing the counterjets. As a result, we reconstruct the amplitudes of the two or three brightest components of the source with an accuracy of no less than 10% without any apparent distortions of their coordinates (for the mapping results of the source 2200+420, see below) and with satisfactory suppression of the symmetric counterjet. This is the minimum sufficient condition for solving the restricted problem of studying the structural evolution of compact extragalactic radio sources using interferometers with a small number of elements. Under the conditions of this problem, the situation where the coordinates of the components would be noticeably and unpredictably distorted because of the nonlinearity of the reconstruction algorithms is totally unacceptable. In reality, the visibility magnitude in VLBI can also be measured with a higher signal-to-noise ratio. Therefore, below, we consider examples of image reconstruction where the data are generated with a signal-to-noise ratio of no less than 10. When the real data are processed, the sampled points of the visibility function with unacceptable noise parameters can always be discarded during prior data editing.

PHASELESS MAPPING OF THE SOURCE 2200+420 USING MULTIBASELINE OBSERVATIONS

The goal of this section is to demonstrate the potentialities of phaseless mapping using the well-known radio source 2200+420 (BL Lacertae), which exhibits several compact bright features on milliarcsecond angular scales, as an example. Parameters of this source can be found in the NASA/IPAC Extragalactic Database (NED).[1] This source belongs to the class of BL Lacertae objects, being its brightest representative. It exhibits long-period variability of both flux and structure. It has been studied quite well. The structure of the source can be judged, for example, by the VLBA maps[2] obtained over the period 1996–2000 from 15-GHz ($\lambda = 2$ cm) observations.

We constructed five maps for the period 1996–1998 from the observations of the International Astrometric and Geodetic Programs (NEOS) on the global International VLBI Array at a frequency of 8.2 GHz ($\lambda = 3.5$ cm).

The mapping was performed by using two independent packages: QUASAR VLBImager developed

[1] http://wwwospg.pg.infn.it/PGblazar/nedBLLac.htm.
[2] http://nedwww.ipac.caltech.edu.

Parameters of the observations and the synthesized maps for the source 2200+420

Date	Frequency, MHz	VLBI stations	Number of UV points	Package Peak flux, Jy/beam	QVImager beam FWHM	Package Peak flux, Jy/beam	DIFMAP beam FWHM
March 26, 1996	8210.99	$GKWN_yN_{20}F$	103	1.62	0.63×0.63	1.30	0.56×0.53 34?3
Sep. 3, 1996	8182.99	$GKN_{20}WFN_y$	127	1.48	0.63×0.63	1.57	0.51×0.57 −1?6
Nov. 12, 1996	8182.99	$FGN_{20}WKN_y$	100	1.79	0.63×0.63	1.82	0.55×0.54 40?4
Aug. 26, 1997	8182.99	$KWN_{20}AN_y$	83	0.72	0.63×0.63	0.89	0.80×0.51 −33?0
Oct. 6, 1998	8182.99	$KN_{20}G_gFWN_y$	115	1.31	0.63×0.63	1.04	0.56×0.43 −15?3
March 26, 1996	8210.99	GK	21	1.10	0.63×0.63	–	–

Note. Abbreviated names of the stations: A—Algopark, F—Fortleza, G—Gilcreek, G_g—GGAO7108, K—Kokee, N_{20}—NRAO20, N_y—Ny Alesund, W—Wettzell.

by the author at the Institute of Applied Astronomy (Russian Academy of Sciences) and CalTech's DIFMAP.

The parameters of the observations and the synthesized maps are given in the table. It lists the dates and frequencies of the observations, the global VLBI stations involved in the experiment, the number of visibility measurements, and parameters of the maps (peak fluxes and the parameters of the Gaussian beam with which the solution was convolved).

The maps obtained by the phaseless method (QUASAR VLBImager) described above and by the self-calibration method in terms of differential mapping (DIFMAP) are shown in Fig. 2. In these maps and those shown below, the minimum level of the contour line corresponds to 1% of the peak value.

Let us turn to the figure. The images along the rows pertain to different dates of observations. The first column (a–e) gives the UV fillings; the second column (f–j) gives the intermediate images obtained from a given visibility magnitude and a zero spectral phase (some of them (f, i) were obtained by using the GMEM, while others (g, h, j) were obtained by the CLEAN method); and the third column (k–o) gives the sought-for images reconstructed from the previous images by using Fienup's algorithm. The images obtained show the structure of the source that is immediately adjacent to the core (within 2 to 3 mas) and allows its evolution with time to be traced. We see individual components of the jet at position angles in the range $(-170°, -180°)$ whose brightnesses and positions change from date to date. Our maps qualitatively agree with the 2-cm VLBA maps (see footnote [2]). The fourth column of Fig. 2 ((p)–(t)) gives the maps obtained by the adaptive calibration method using the DIFMAP package (the scale of these maps is half the scale of the previous ones).

Analysis of images ((p)–(t)) shows that it is not always justifiable to use equations for closure phases. Thus, for example, we see a symmetric counterjet on maps (p) and (q), which, as follows from the higher-quality astrophysical VLBA maps (Fig. 2), should not be there. The presence of a counterjet is indicative of incomplete spectral phase retrieval, which shows the spurious quasi-symmetry of the source. As a result, the strong component of the jet was not fully reconstructed; it broke down into two parts, distributing the brightness between them. Thus, here, we clearly show a case where using unreliable phase information may prove to be more dangerous than its retrieval from the visibility magnitude measured with a sufficient accuracy.

A comparison (given the beam size) of maps (m) and (n) with maps (r) and (s), respectively, shows good agreement (see also the peak fluxes in the table), implying that the visibility function was measured reliably in these cases. A comparison of map (o) with map (t) again argues for the phaseless mapping that resolved not one, but two components of the jet present on the maps for the two previous dates.

The latter result can be explained as follows. If the visibility magnitude has been measured with a sufficiently high accuracy, then the intermediate image of the source with a zero spectral phase will contain all of the structural features and their mirror features relative to the phase center of the map. The accuracy of reconstructing the coordinates of the source's

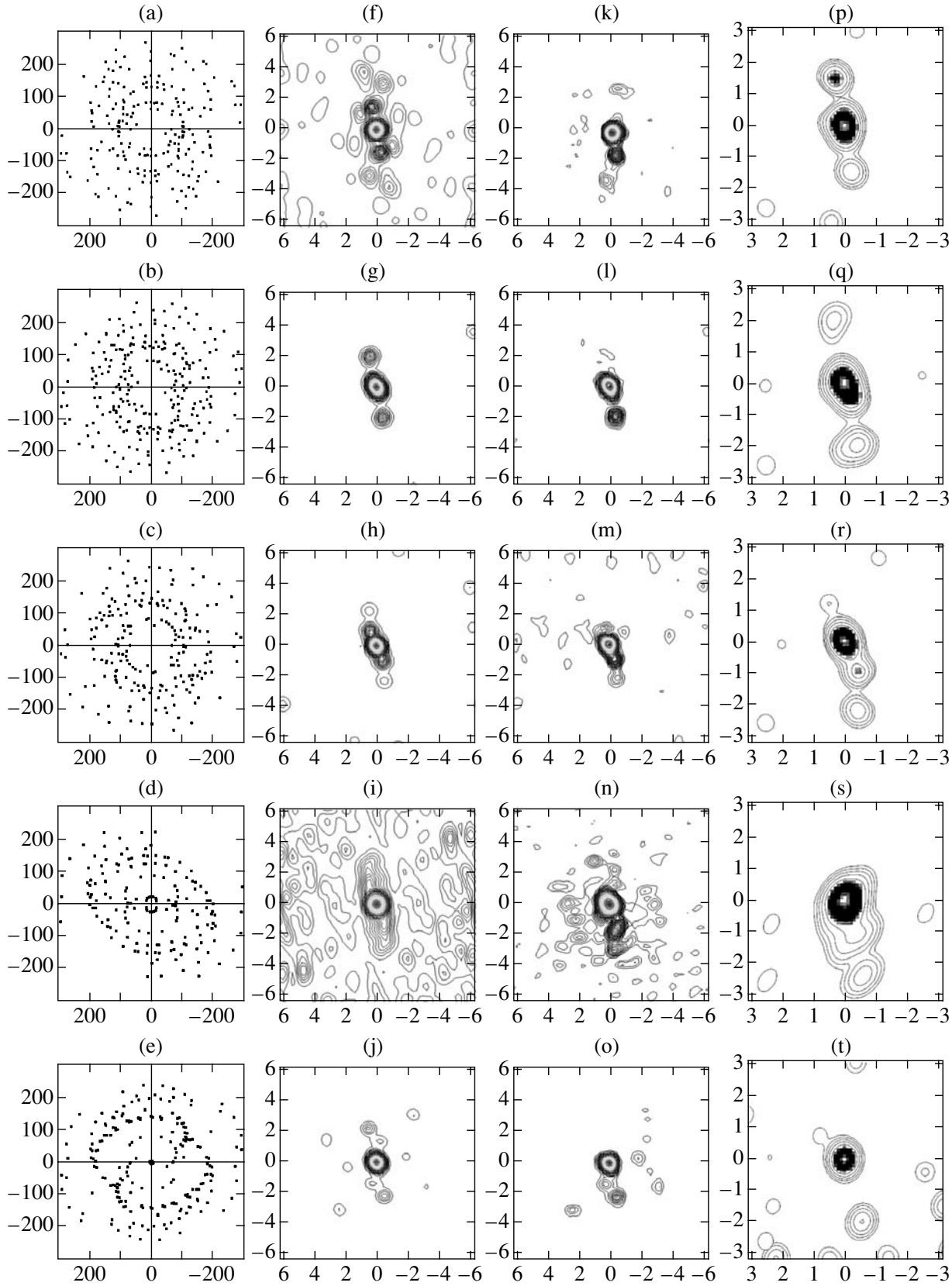

Fig. 2. Mapping of the source 2200+420 based on astrometric and geodetic data from a global VLBI array using the phaseless (QUASAR VLBImager) self-calibration (DIFMAP) methods (see the text).

components depends only on the accuracy of measuring the visibility magnitude. The subsequent image reconstruction using Fienup's algorithm leads to an approximately twofold enhancement of the structural components with correct coordinates, as we see from a comparison of the maps in the middle and the last columns of Fig. 2. In contrast, using distorted or insufficient phase information in adaptive calibration methods may lead to an unpredictable distortion of the source's structure, both the brightness and the coordinates of its individual components. In this case, the reconstruction accuracy depends not only on the accuracy of the visibility magnitude, but also on the degree of distortion of the phase information.

MAPPING OF COMPACT RADIO SOURCES ON A TWO-ELEMENT INTERFEROMETER

During the Earth's rotation, the interferometer baseline vector describes an ellipse whose coordinates on the UV plane are defined by the equation (Thompson *et al.* 1986)

$$\frac{u^2}{(L_x^2+L_y^2)}+\frac{(v-v_0)^2}{(L_x^2+L_y^2)\sin^2\delta_0}=1, \qquad (10)$$

where L_x and L_y are the components of the baseline vector $P_{ij}(u,v,w)$ along the equatorial coordinate axes, δ_0 is the declination of the phase center of the source, and $v_0=w\cos\delta_0$. Below, we assume that the coordinates u, v, w are measured in units of wavelengths.

In investigating a single-baseline interferometer for mapping, it would be appropriate to use the approximation of a model source by a set of point components. This approximation is justifiable, because, in this case, the spectrum magnitude is extrapolated to higher frequencies from the values specified only on one curve (10); image reconstruction in the form of a set of very compact features in the limit of point components corresponds to this case. Therefore, sources with this type of structure are most suitable for observations on a two-element interferometer. If, however, the source at a given resolution of the instrument reveals extended features, they will be represented in the reconstructed maps as compact components with coordinates at the points of maximum brightness.

Clearly, the parameters A, r, θ uniquely, to within rotation through 180°, determine the one-dimensional visibility function on curve (10). Let us illustrate how variations of the source's parameters affect the form of the visibility magnitude using a specific example.

In Fig. 3, the left column shows the images of model sources with the following parameters of the compact component of the jet:

(Fig. 3a)—$A=0.4,\ r=6.0$ mas, $\theta=38°$,

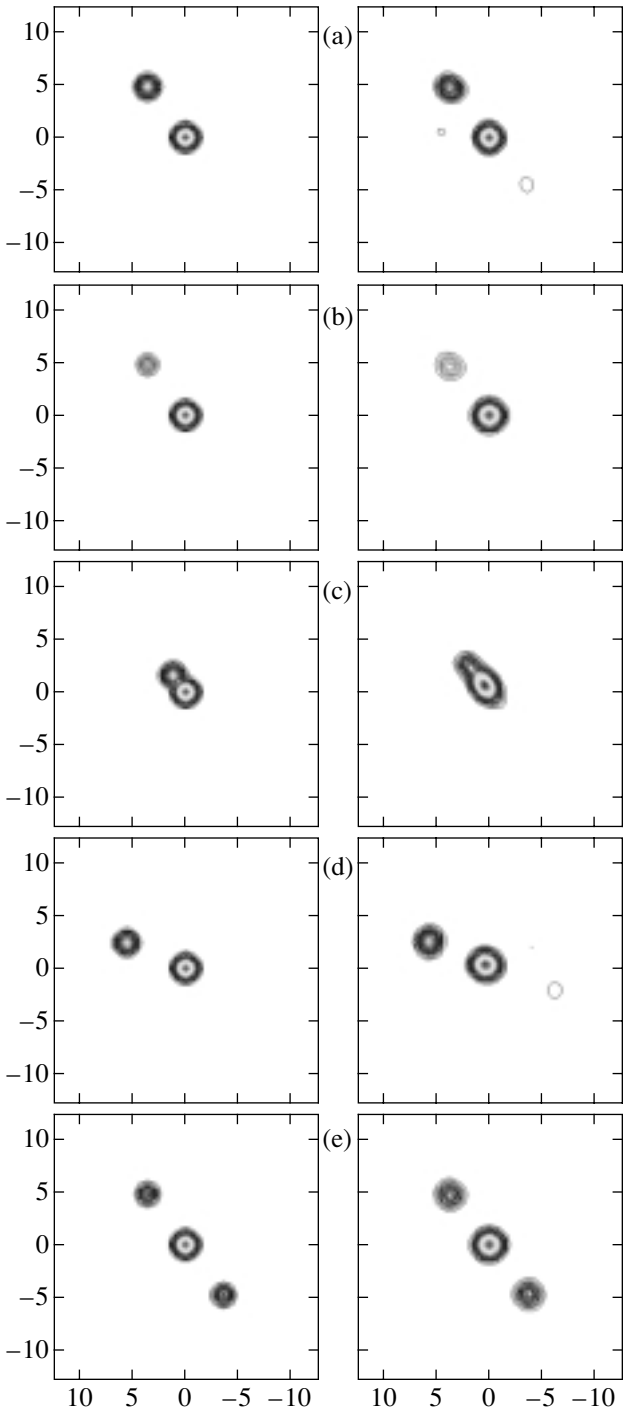

Fig. 3. Simulation of phaseless mapping for a two-component source with various parameters on a two-element interferometer (see the text).

(Fig. 3b)—$A=0.1,\ r=6.0$ mas, $\theta=38°$,

(Fig. 3c)—$A=0.4,\ r=2.0$ mas, $\theta=38°$,

(Fig. 3d)—$A=0.4,\ r=6.0$ mas, $\theta=68°$,

(Fig. 3e)—$B=0.2,\ r=6.0$ mas, $\theta_1=38°,\ \theta_2=218°$.

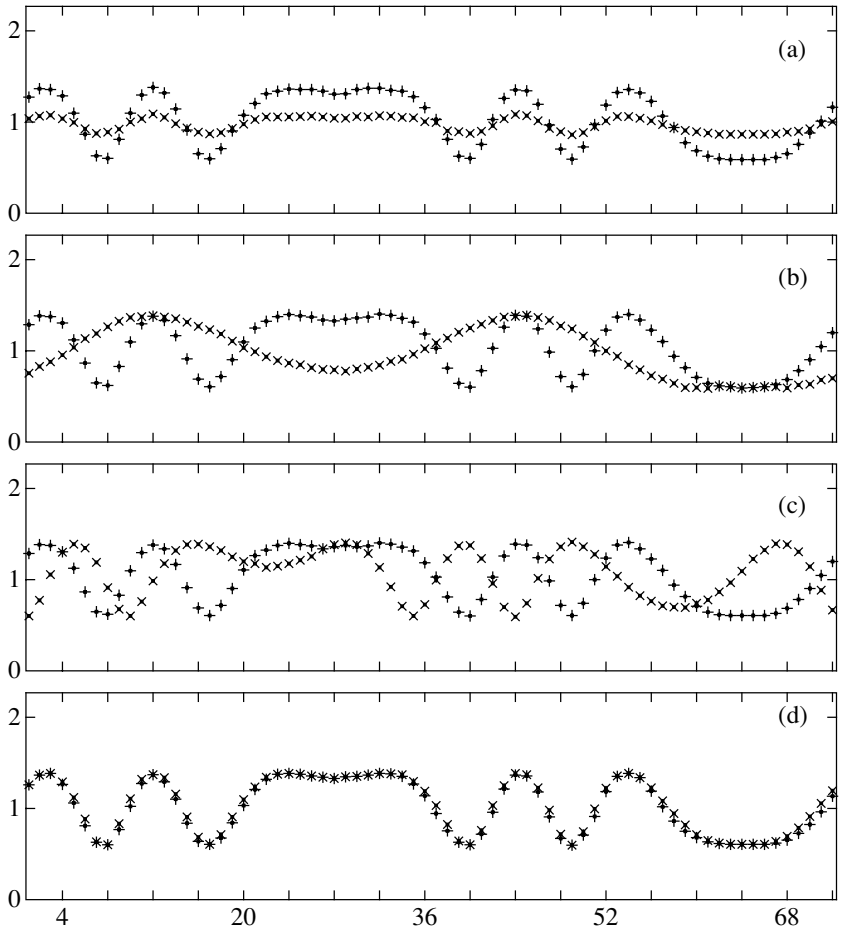

Fig. 4. Influence of the parameters of a two-component source on the form of the visibility magnitude on an interferometer baseline (see the text).

All of the changes in the form of the visibility magnitude determined on the Svetloe–Zelenchuk baseline for a source with a declination of $\delta = 73\overset{\circ}{.}5$ are shown in Fig. 4. The corresponding UV filling is shown in Fig. 5a.

In all panels of Fig. 4, the pluses indicate the visibility magnitude of the reference source (time is plotted along the horizontal axis) shown in Fig. 3a; the crosses indicate the visibility magnitude of the source with a changed value of a particular parameter. Thus, we can see from Figs. 3a–3d, and (d) how changes in brightness A of the component, in distance r from the map center, in position angle θ, and the separation of the component into two symmetric parts with equal brightnesses, respectively, affect the visibility function. More specifically, a decrease in the brightness of the component causes a decrease in the modulation of the visibility magnitude; a decrease in the distance of the component from the center causes a decrease in the modulation frequency; a change in the position angle causes a linear shift in the visibility function with time; and the separation of the jet component into two symmetric parts with equal brightnesses causes an increase in the visibility magnitude by approximately $A^2 \sin^2 \phi/2(1 + A\cos\phi)^2$.

Let us now present the results of our reconstruction of the two-component sources shown in Fig. 3 from visibility magnitude data generated with a signal-to-noise ratio of ≈ 10 on the Svetloe–Zelenchuk baseline. The right column of Fig. 3 shows the final images reconstructed by using the GMEM and Fienup's algorithm. Analysis of our results indicates that the brightnesses of the components were reconstructed with an accuracy up to 10%, and the coordinates of the components were reconstructed without apparent distortions.

Thus, for two-component sources, mapping using single-baseline data yields a reconstruction quality that may well be acceptable for solving a number of problems. One of these problems might be, for example, investigation of the motion of the brightest components of a source on long time scales; another problem can be allowance for the influence of the structure in astrometric reduction, because the components that are brightest and farthest from the

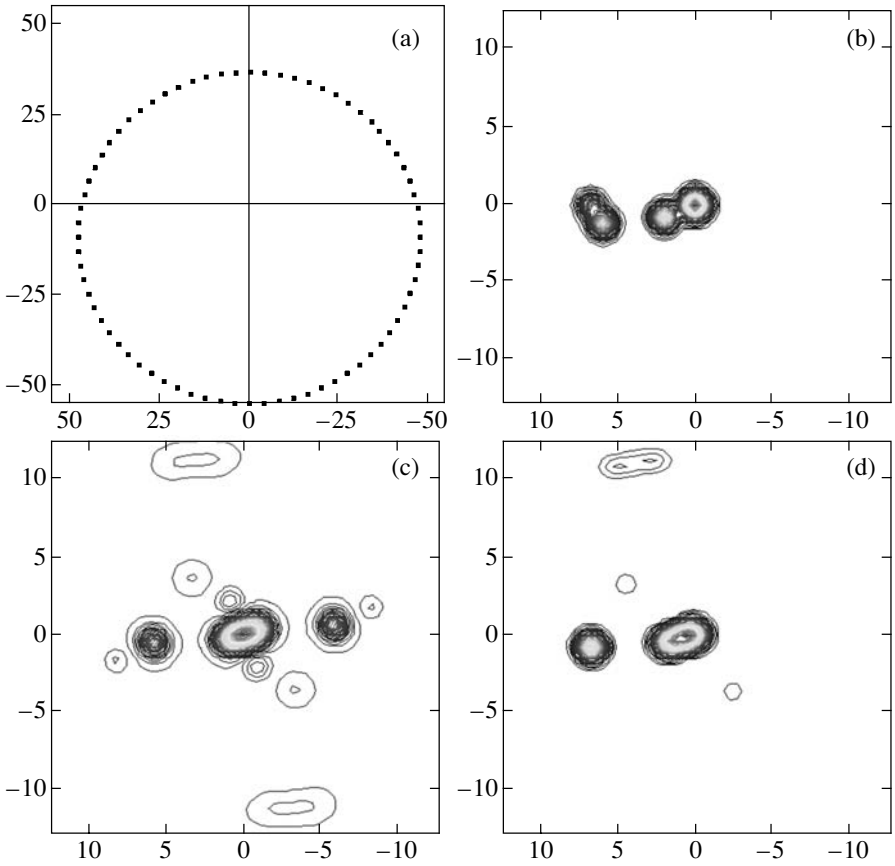

Fig. 5. Mapping simulation for the four-component source 0212+735 based on observations on the Svetloe–Zelenchuk interferometer (see the text).

core introduce the largest error in determining the coordinates of reference sources (Bajkova 2002a).

Clearly, the more complete and accurate the determination of the visibility magnitude on an interferometer baseline, the higher the accuracy of reconstructing the structure of a source by using the methods of the analytic continuation of the spectrum. In practice, the reconstruction problem is solved with a limited accuracy, because the data are discrete and contain measurement errors, causing the necessary analyticity condition to be violated. Fortunately, however, as we showed above, acceptable image estimates can be obtained by using reconstruction methods (GMEM, Fienup's algorithm) that are stable against noise. In this case, the brightest components are reconstructed reliably. Thus, data with a signal-to-noise ratio of $\approx$10 yield maps that generally have two or three very bright, well-reconstructed components.

Below, we present the results of yet another simulation (Fig. 5) that confirm our conclusions. Figure 5a shows the diurnal UV filling that corresponds to the Svetloe–Zelenchuk interferometer and the declination of the source 0212+735. Figure 5b shows the four-component model of 0212+735 that was roughly estimated from existing VLBA maps (see footnote 2). Figure 5c shows the intermediate GMEM map reconstructed from the visibility magnitude that was measured with a signal-to-noise ratio of $\approx$ 10. Figure 5d presents the final reconstruction result obtained by Fienup's method. A comparison of the original model (Fig. 5b) and the reconstructed map (Fig. 5d) indicates that we have been able to reconstruct three of the four components; the resolution of the component near the core was not quite as good as that on the original map. The fourth (faintest and farthest) component was not reconstructed because of the visibility errors in which the contribution from this component was lost (in fact, the third and fourth components merged together). Clearly, as the accuracy of measuring the visibility magnitude increases, the accuracy of reconstructing individual components can also increase. However, as follows from our results, we can obtain maps of acceptable quality for solving the limited range of problems outlined above even at a relatively low signal-to-noise ratio.

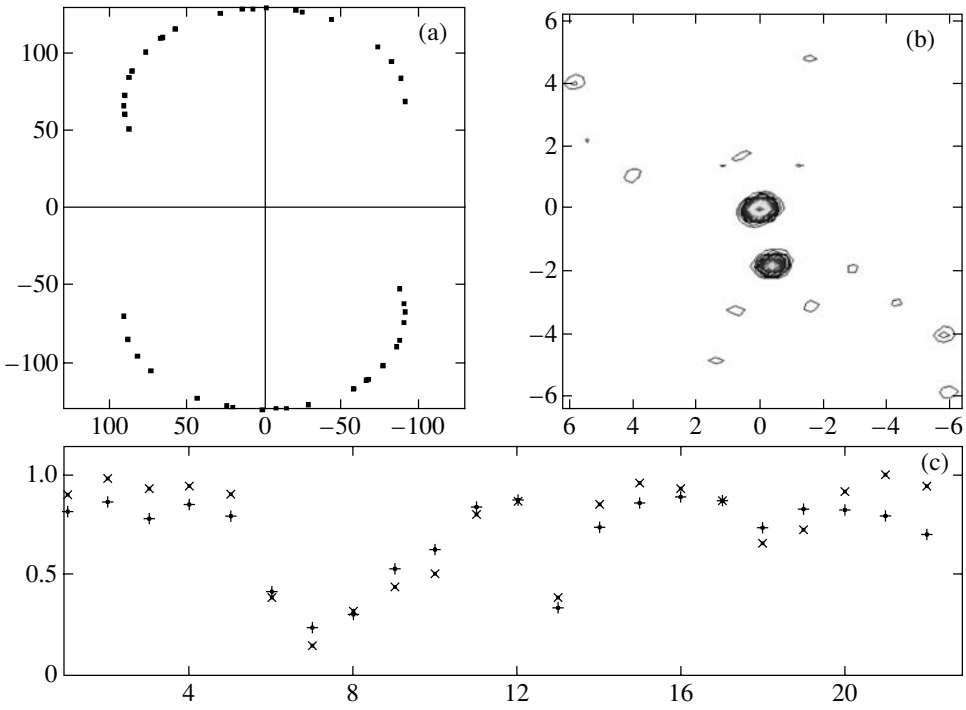

Fig. 6. Phaseless mapping of the source 2200+420 using the astrometric and geodetic VLBI observations of March 26, 1996, on the Gilcreek–Kokee baseline (see the text).

PHASELESS MAPPING OF THE SOURCE 2200+420 USING SINGLE-BASELINE OBSERVATIONS

Let us now present the results of our mapping of the source 2200+420 using data obtained only on one interferometer baseline (Fig. 6). To this end, we separated out the observations on the Gilcreek–Kokee baseline from the geodetic and astrometric observations on March 26, 1996. The corresponding *UV* filling is shown in Fig. 6a. Parameters of the observations and the output map are given in the last row of the table.

The image of the source reconstructed using the GMEM and Fienup's algorithm is shown in Fig. 6b. The extent to which the input and output data agree can be judged from Fig. 6c. In this figure, the pluses indicate the measured visibility magnitude (time is plotted along the horizontal axis), and the crosses indicate the visibility magnitude that corresponds to the reconstructed image. As we see from Fig. 6b, we were able to reconstruct only the most prominent two-component structure of the source, in close agreement with the reasoning given in the previous section.

The derived relative fluxes from the components are close to the fluxes from the components of image (k) in Fig. 2. Thus, we conclude that mapping using single-baseline data may prove to be quite acceptable in solving the restricted problem of studying the structural evolution of sources that consist of several bright compact features.

CONCLUSIONS

Despite the existence of efficient adaptive calibration methods that use closure phases directly or indirectly (Cornwell and Fomalont 1999) and the existence of powerful processing packages that perform them (AIPS, DIFMAP, ASL[3]), it seems to be of considerable interest to develop and use alternative phaseless mapping methods for the following reasons:

(1) The spectral phase is such an important characteristic of the image that using erroneous or insufficient phase information (at a small number of baselines) is more dangerous than restoring it from the spectrum magnitude measured with sufficient accuracy. Such situations are not uncommon for VLBI observations that are not directly intended for astrophysical mapping, but provide invaluable data for studying the structural evolution of sources on long time scales.

(2) The phase can be uniquely retrieved in principle from the spectrum magnitude for multidimensional ($\geq$2) images with a finite carrier.

[3] http://platon.asc.rssi.ru/dpd/asl/asl.html.

(3) Since the spectra of finite functions are analytic, the entire function can be reconstructed from the known part of it, which is important for VLBI.

(4) There are reliable numerical methods and reconstruction algorithms that are stable against noise in the data.

(5) The relative simplicity of the structure of compact extragalactic radio sources on milliarcsecond angular scales ensures that our phaseless mapping method converges reliably and rapidly.

(6) Available Russian-made instruments with a small number of elements (in the limit, two-element ones) can be used to solve a limited range of problems (e.g., to study the evolution of the brightest components of extragalactic radio sources).

However, it is important to emphasize that we did not set the goal of contrasting the suggested phaseless method with the traditional VLBI mapping methods that use partial phase information (equations for closure phases). The methods that use any properly measured phase information are always better than the phaseless methods. In this paper, we suggest using the phaseless methods as alternatives to the existing methods that use phase information only in the following two cases: (1) when the equations for closure phases are insufficient or unavailable (a two-element interferometer) and (2) the available phase information is unreliable, and the visibility magnitudes were measured with a sufficient accuracy. In particular, the suggested method can be used for mapping based on data from an intensity interferometer.

Thus, we have considered an efficient phaseless mapping method that was tested both on models and on real VLBI observations. We have presented the results of our study of a two-element interferometer, which are of current interest even now in connection with the putting into operation of a Russian-made instrument based on Quasar RT-32 radio telescopes (Bajkova 2002b).

REFERENCES

1. A. T. Bajkova, Astron. Astrophys. Trans. **1**, 313 (1992).
2. A. T. Bajkova, Soobshch. Inst. Prikl. Astron. Ross. Akad. Nauk, No. 62 (1994).
3. A. T. Bajkova, Izv. Vyssh. Uchebn. Zaved. Radiofiz. **39**, 472 (1996).
4. A. T. Bajkova, T. B. Pyatunina, and A. M. Finkel'shteĭn, *Trudy Inst. Prikl. Astron. Ross. Akad. Nauk, Astrometry and Geodynamics* (Inst. Prikl. Astron. Ross. Akad. Nauk, St. Petersburg, 1997), Vol. 1, p. 22 [in Russian].
5. A. T. Bajkova, Izv. Vyssh. Uchebn. Zaved., Radiofiz. **43**, 895 (2000).
6. A. T. Bajkova, Izv. Vyssh. Uchebn. Zaved., Radiofiz. **45**, 187 (2002a).
7. A. T. Bajkova, *Russian Conference in Memory of A. A. Pistol'kors: Radio Telescopes RT-2002* (Pushchinskaya Radioastron. Obs. Astron. Kosm. Tsentr Fiz. Inst. Akad. Nauk, Pushchino, 2002b), p. 20.
8. J. E. Baldwin and P. J. Warner, Mon. Not. R. Astron. Soc. **175**, 345 (1976).
9. J. E. Baldwin and P. J. Warner, Mon. Not. R. Astron. Soc. **182**, 411 (1978).
10. Yu. M. Bruck and L. G. Sodin, Optics Comm. **30**, 304 (1979).
11. T. J. Cornwell, R. Braun, and D. S. Briggs, *Synthesis Imaging in Radio Astronomy II,* Ed. by G. B. Taylor, C. L. Carilli, and R. A. Perley, ASP Conf. Ser. **180**, 151 (1999).
12. T. J. Cornwell and E. B. Fomalont, *Synthesis Imaging in Radio Astronomy II,* Ed. by G. B. Taylor, C. L. Carilli, and R. A. Perley, ASP Conf. Ser. **180**, 187 (1999).
13. A. M. Finkelstein and A. T. Bajkova, Preprint No. 15, IPA AN SSSR (Institute of Applied Astronomy, Academy of Sciences of the USSR, Leningrad, 1990).
14. J. R. Fienup, Opt. Lett. **3**, 27 (1978).
15. J. R. Fienup, Appl. Opt. **21**, 2758 (1982).
16. J. R. Fienup, T. R. Crimmins, and W. Holsztynski, J. Opt. Soc. Am. **72**, 610 (1982).
17. R. Gerchberg and W. O. Saxton, Optik **35**, 237 (1972).
18. M. H. Hayes, IEEE Trans. Acoust., Speech, Signal Process. **30**, 140 (1982).
19. Ya. I. Khurgin and V. P. Yakovlev, *Finite Functions in Physics and Engineering* (Nauka, Moscow, 1971) [in Russian].
20. A. V. Oppenheim and J. S. Lim, Proc. IEEE **69**, 529 (1981).
21. T. B. Pyatunina, A. M. Finkelstein, I. F. Surkis, *et al., Trudy Inst. Prikl. Astron. Ross. Akad. Nauk, Astrometry and Geodynamics* (Inst. Prikl. Astron. Ross. Akad. Nauk, St. Petersburg, 1998), Vol. 3, p. 259.
22. J. L. C. Sanz and T. S. Huang, J. Opt. Soc. Am. **73**, 1442 (1983).
23. *Image Recovery. Theory and Application,* Ed. by H. Stark (Academic, Orlando, 1987; Mir, Moscow, 1992).
24. A. R. Thompson, J. M. Moran, and G. W. Swenson, Jr., *Interferometry and Synthesis in Radio Astronomy* (Wiley, New York, 1986; Mir, Moscow, 1989).

Translated by V. Astakhov

Astronomy Letters, Vol. 30, No. 4, 2004, pp. 232–239. Translated from Pis'ma v Astronomicheskiĭ Zhurnal, Vol. 30, No. 4, 2004, pp. 268–276.

The Structure of Galactic Gas at High Latitudes: The Southern Polar Cap

I. V. Gosachinskii*, G. N. Il'in, and V. A. Prozorov

Special Astrophysical Observatory, St. Petersburg Branch, Russian Academy of Sciences, Pulkovo, St. Petersburg, 196140 Russia

Received July 30, 2003

Abstract—We analyze the angular structure of the 21-cm interstellar neutral hydrogen emission at six and seven declinations in the northern (published previously) and southern polar caps of the Galaxy (Galactic latitudes from $-40°$ to $-90°$), respectively, with an extent of $90°$ in right ascension. The RATAN-600 radio telescope has a beam width averaged over these regions of $2'.0 \times 30'$. One-dimensional power spectra for the angular distribution of interstellar neutral hydrogen emission were computed in each 6.3-km s^{-1}-wide spectral channel by using the standard Fast Fourier Transform (FFT) code and were smoothed over 1^h in right ascension. The Galactic latitude dependence of the mean parameters for the sky distribution of H I line emission at high latitudes was found to correspond to the distribution of gas in the form of a flat layer only in the northern region, while in the southern cap, the gas distribution is much less regular. In addition, the mean H I radial velocities are negative everywhere (-3.7 ± 3.0 km s^{-1} in the north and -6.0 ± 2.4 km s^{-1} in the south). The power spectra of the angular fluctuations in the range of angular periods from $10'$ to $6°$ appear as power laws. However, the spectral indices change greatly over the sky: from -3 to -1.2; on average, as the Galactic latitude increases and the H I column density decreases, the fluctuation spectrum of the interstellar gas emission becomes flatter. In the northern polar region, this behavior is much more pronounced, which probably stems from the fact that the gas column density in the south is generally a factor of 2 or 3 higher than that in the north. Therefore, the spectra are, on average, also steeper in the south, but the dependence on Galactic latitude is weaker. Using simulations, we show that the observed power-law spectrum of the H I emission distribution can be obtained in terms of not only a turbulent, but also a cloud model of interstellar gas if we use our previous spectra of the diameters and masses of H I clouds. © *2004 MAIK "Nauka/Interperiodica".*

Key words: *interstellar medium, neutral hydrogen, cloud structure.*

INTRODUCTION

The characteristics of the H I cloud structure determined from observations play a major role in elucidating the main physical processes that govern its existence: heating and cooling, cloud–cloud collisions, molecular cloud formation, gravitational instability and star formation, etc.

There are many methods for studying the structure of the interstellar medium. The natural view of a cloud as an object that is separated from an extended background and neighboring objects by the intensity distribution of its emission is taken in many observational works. However, several authors (Crovisier and Dickey 1983; Green 1993; Dickey *et al.* 2001) used a statistical method: they measured the spatial spectrum of the H I intensity distribution with interferometers or single dishes. The major advantage of the spectral approach is its high sensitivity to the angular characteristics of the gas emission, but only if these characteristics are stationary in regions of significant angular sizes. It should also be noted that, first, the measured spectra are angular rather than spatial, second, all authors measure the so-called power spectra, i.e., the spectra of the squares of the amplitudes with the loss of phase information, and, third, small areas in the Galactic plane where the distribution of interstellar gas emission is far from stationary and depends strongly on the radial velocity are chosen for measurements.

The angular spectra obtained by the above authors are close to power laws. However, as Green (1993) pointed out, the spectral indices measured with interferometers (two-dimensional spectra) differ by unity from the one-dimensional spectra computed by using the Fourier transform of the drift curves obtained with single dishes. The two-dimensional spectra are steeper, and their amplitudes are smaller.

The papers by Lazarian (1995), Lazarian and Pogosyan (2000), and Goldman (2000) are also worthy of note (in predicative). These authors made attempts to mathematically interpret the observed

*E-mail: gos@fsao.spb.su

angular spectra in an effort to directly calculate the three-dimensional statistics of interstellar gas fluctuations and its relationship to the turbulence characteristics of the interstellar medium, which is believed to determine these observed spectra.

Taking into account all these circumstances, in 1996 we embarked on a program of measuring the angular spectra of the 21-cm H I emission at high Galactic latitudes with the RATAN-600 radio telescope. Previously (Gosachinskii *et al.* 1999), we published the results of our study of the northern Galactic polar cap. Here, we present the results of our observations of a region around the southern Galactic pole and make a comparison of these data. Note that the gas located near the Sun (300–600 pc) at nearly zero radial velocities (± 20 km s^{-1}) is mainly observed at high Galactic latitudes. In contrast to the angular distribution of its emission near the Galactic plane, its observed angular characteristics are expected to be much more statistically homogeneous in this case. Therefore, it is hoped that the application of spectral methods for studying the structural properties of the distribution of interstellar gas emission averaged over the sky on a large scale is adequate.

INSTRUMENTATION AND TECHNIQUES

The RATAN-600 antenna has a $2'.0 \times 30'$ field-averaged beam FWHM and an effective area of 900–1000 m^2 at a wavelength of 21 cm at declinations from $-40°$ to $+10°$. The automated radiospectrometric system of the radio telescope has an uncooled HEMT amplifier at its input at decimeter wavelengths (Il'in *et al.* 1997). In our observations, we used a 39-channel filter spectrum analyzer (Venger *et al.* 1982) with a channel bandwidth of 30 kHz (6.3 km s^{-1}) and a separation between the channels of 30 kHz, so the full bandwidth of the survey was 1.2 MHz. The time constant of the output devices was 6 s, and the sampling period was 3 s. An IBM PC was used for system control and data acquisition and primary reduction through KAMAK (Alferova *et al.* 1986; Venger *et al.* 1997). Observations of a series of bright references sources with measured fluxes (Venger *et al.* 1981) were used to check the parameters of the antenna and the instrumentation.

The southern polar region was observed during the period 1999–2003. Drift curves were obtained at declinations of $-40°$, $-34°$, $-27°$, $-20°$, $-10°$, $0°$, and $+10°$ in the range of right ascensions from 22^h to 4^h (Galactic latitudes from $-40°$ to $-90°$). At each declination, we carried out two sets of observations, each containing 10 to 14 records, with a spectrum analyzer frequency shift by half the separation between the spectral channels, so each drift curve ultimately contained 78 spectral channels that followed at 3.15-km s^{-1} steps. The mean square of the noise fluctuations in the averaged records was 0.1 K. We measured all radial velocities relative to the Local Standard of Rest. In addition, we obtained one more drift curve for the northern polar cap at a declination of $-5°$; the results of its processing are presented below in figures.

At high latitudes, where the total intensity of the 21-cm H I emission is low, the radio line profiles are known to consist of the following three main components: the narrow emission line near zero radial velocities that originates in an H I layer near the Sun, the emission from rare H I clouds at high negative and positive radial velocities, and the stray radiation from the far sidelobes and diffuse background of the antenna system. An example of a profile that clearly shows the first and the third components is given in our previous paper (Gosachinskii *et al.* 1999). Eliminating the stray diffuse background is a serious problem, and special methods have been developed for its solution (see, e.g., Heiles *et al.* 1981; McGee and Newton 1986; Hartmann *et al.* 1996). However, as we showed previously, this radiation may be ignored in the formulated problem, because the pattern of the diffuse background of the antenna cannot yield small-scale features in the intensity distribution. In general, the large-scale H I distribution at high latitudes was studied in pioneering works (see, e.g., Fejes and Wesselius (1973) and references therein). Our data on the total gas column density that we obtained after eliminating the stray diffuse background smoothed by the RATAN-600 beam are used only to compare the total H I column density with the fine-structure parameters determined with the same instrument using one coordinate.

We computed the one-dimensional angular spectrum of the interstellar gas intensity distribution in each spectral channel by using the standard FFT code based on 64 points. Consequently, for a sampling period of 3^s, the first and the last (32nd) spectral harmonics correspond to periods in right ascension of 192^s and 6^s, respectively. At $\delta = 0°$, these periods correspond to angular periods of $48'$ and $1'.5$, respectively. At other declinations, these periods increase in inverse proportion to $\cos\delta$. It emerged that the sensitivity of the instrumentation achieved in our survey allowed a signal to be isolated at spatial harmonics with numbers no higher than 8 to 10. Therefore, we subsequently smoothed the drift curves by the function $\sin x/x$ with a sine period of 24^s so as to be able to compute the spectra for periods from 48^s to 1536^s using the same FFT code based on 64 points with appropriate resampling while avoiding the so-called aliasing effect.

The spectra of the squares of the amplitudes (i.e., the spatial power spectra) were smoothed over a

Table 1. Mean radial velocities of H I at low radial velocities in the southern polar cap

δ	α										
	03^h30^m	03 00	02 30	02 00	01 30	01 00	00 30	00 00	23 30	23 00	22 30
+10.0	−2.3	−5.3	−4.5	−8.5	−8.3	−6.8	−6.8	−6.8	−6.8	−4.5	−2.0
	+9.0	+10.5	+12.8	+13	+13	+13	+12.8	+12.8	+12.8	+12.0	+10.5
0.0	−3.0	−5.0	−7.0	−8.0	−8.0	−8.0	−6.0	−2.0	−1.5	−2.0	−0.5
	+8.0	+8.0	+7.5								
−10.0	−4.7	−4.7	−7.5	−10.3	−8.4	−8.4	−8.4	−5.6	−2.8	−0.9	−0.9
	+9.3	+8.4	+7.5	+9.3							
−20.0	−6.6	−10.3	−11.3	−9.4	−8.4	−10.3	−9.4	−4.7	−3.8	−3.8	−4.7
	+7.5	+1.5	0.0	0.0							
−27.0	−3.7	−8.4	−7.5	−8.4	−7.5	−5.6	−5.6	−3.7	−3.7	−5.6	−5.6
−34.0	−3.7	−4.7	−6.0	−6.5	−6.5	−6.9	−7.3	−5.6	−5.6	−5.6	−7.1
−40.0	−5.6	−6.2	−7.5	−8.4	−8.4	−8.4	−6.5	−6.5	−5.6	−5.6	−3.7
	−28										

1^h (15°) interval and along the radial velocity axis over five spectral channels (15.7 km s^{-1}). Subsequently, the system noise spectrum obtained as a spectrum averaged over the spectrometer channels where no line emission was observed was subtracted from the maximum spectrum. Since the system noise does not correlate with the fluctuations in the H I line intensity distribution recorded by the RATAN-600 antenna, their spectra are added quadratically (in power). This is how they should be separated, and therein lies the physical meaning of the angular power spectrum. Subsequently, we corrected the difference spectrum for the following three effects that smoothed the observed fluctuations: smoothing by the horizontal antenna beam, filtering by the output low-frequency devices of the spectrometer, and averaging of the fluctuations over the vertical antenna beam.

Thus, we obtained 11 statistically significant spectra computed at $0^h.5$ steps in each drift curve with an extent of 6^h in right ascension. The fluctuation amplitude of the interstellar gas emission at very low angular frequencies is known to be large. Since, on the one hand, angular periods no larger than a few degrees were of special interest, and, on the other hand, there is always the risk of spurious signals leaking through the sidelobes of the transfer function of the FFT spectrum analyzer in a spectral analysis, we removed the periods longer than 6° as well as the constant component from the drift curves in all channels.

RESULTS

The Total H I Column Density

The radial velocities of the H I peaks in the region around the southern Galactic pole under study are listed in Table 1. Since no data of this kind were published in our previous paper for the northern region, we give them here in Table 2 to conveniently compare the data on both regions. Our data confirm the long-known fact that the mean radial velocities of the circumsolar gas are mainly negative both in the south (-6.0 ± 2.4 km s^{-1}) and in the north (-3.7 ± 3 km s^{-1}). No clear systematic correlation of the H I radial velocity with coordinate (e.g., Galactic latitude, Fig. 1) is observed both in the north and in the south. A slow fall of the background gas in the layer toward its middle plain may serve as the only plausible explanation of this phenomenon. This assumption also accounts for the choice of the x axis in Fig. 1: if the spatial velocity is mainly perpendicular to the Galactic plane, then the radial velocity is proportional to $V_g \sin|b|$.

Some of the areas in the regions under study (mainly at low latitudes) are characterized by profile

Table 2. Mean radial velocities of H I at low radial velocities in the northern polar cap

δ	α										
	15^h30^m	15 00	14 30	14 00	13 30	13 00	12 30	12 00	11 30	11 00	10 30
+50?0	−5.0	−4.0	−3.0	−5.0	−7.0	−8.0	−7.0	−7.0	−9.0	−12.0	−14.0
+39.0	−1.5	−1.5	−2.0	0.0	0.0	−2.0	−2.5	–	–	–	–
+27.5	−3.0	−1.5	−1.5	−3.5	−5.0	–	–	–	–	−7.0	0.0
+16.0	−0.5	−0.5	0.0	+0.5	0.0	0.0	+0.5	0.0	−1.0	−5.0	−5.5
+5.0	−2.5	−2.5	−2.5	−2.5	−3.0	−3.5	−5.0	−5.0	−6.0	−7.0	−5.04
−5.0	0.0	0.0	0.0	0.0	−6.0	−6.0	−6.0	−6.0	−8.3	−7.5	−6.0
					+3.0	+2.3	+3.0	+3.0	+7.5	+2.3	+3.3

splitting. In this case, we gave the radial velocities of both peaks in Tables 1 and 2. The appearance of H I emission at positive velocities can be easily explained. In fact, a large-scale H I structure at nearly zero radial velocities that is commonly called ridges is known to exist at high latitudes. Fejes and Wesselius (1973) gave parameters for 13 such ridges; most of them (11) are almost perpendicular to the Galactic plane, and some of them reach latitudes of $\pm 40°$. Note also that, in contrast to the background gas, many of them have positive radial velocities, and five ridges fall within the region of our survey precisely where the peaks at positive velocities are observed. Since any large-scale structure is not the goal of our study, these peaks are not considered below. The FWHMs of the H I profile peaks corrected for the analyzer band smoothing effect are shown in Fig. 2 for the northern and southern polar caps. The mean FWHMs are 13.4 ± 3.2 km s^{-1} in the south and 9.8 ± 3.0 km s^{-1} in the north; there is no correlation with coordinates. Finally, the H I column density in the southern polar region is given in Table 3, and its plot against cosec$|b|$ for the north and the south is shown in Fig. 3. Since the abscissas in Figs. 2 and 3 are proportional to the extent of the line of sight for an observer within the flat layer, it is interesting to note that the layer appears flat only in the northern part. In the south, first of all, the gas column density is a factor of 2 or 3 higher than that in the north, and, second, its distribution is much less regular. Our conclusions are consistent with the data by Fejes and Wesselius (1973) and with the fact that the inclined H I disk discovered by these authors does not fall within the region of our survey, because it lies at lower latitudes.

Angular Spectra of the H I Line Emission

In general, the one-dimensional angular fluctuation power spectra of the 21-cm H I line intensity distribution in the southern Galactic polar cap also appear as power laws as those in the northern region (Gosachinskii *et al.* 1999). The spectral indices, which are the slopes of the regression line, are given together with their rms computational errors in Table 4. As in the north, the angular spectra are characterized by a large spread in indices: from −1.2 to −3. Although the relation between the angular scale of the spectra and the time scale depends on declination, it is clear that this merely displaces the angular spectra on a logarithmic scale along the x axis without changing their slopes (spectral indices).

The spectral indices for the northern and southern regions can be compared with one another and with other parameters by using Figs. 4 and 5. Since we do not know how the spectral index might depend on latitude, we took the latitude in degrees as the abscissa in Fig. 4. The northern and southern polar caps differ not only in total gas column density (Fig. 3), but also in gas structure. In the southern region, the spectral index correlates much better with Galactic latitude than it does in the northern region (Fig. 4, the correlation coefficient is −0.7), although, in general, the fluctuation spectra become flatter with increasing Galactic latitude in both regions.

Surprisingly, the clear correlation between spectral index and total gas column density that we found previously for the northern region (Fig. 5) is much less distinct in the southern polar cap. However, it should be borne in mind that the detected flattening of the fluctuation spectra could be of a different nature: it could be a physical effect that stems from the fact that features of small angular sizes at a high total density

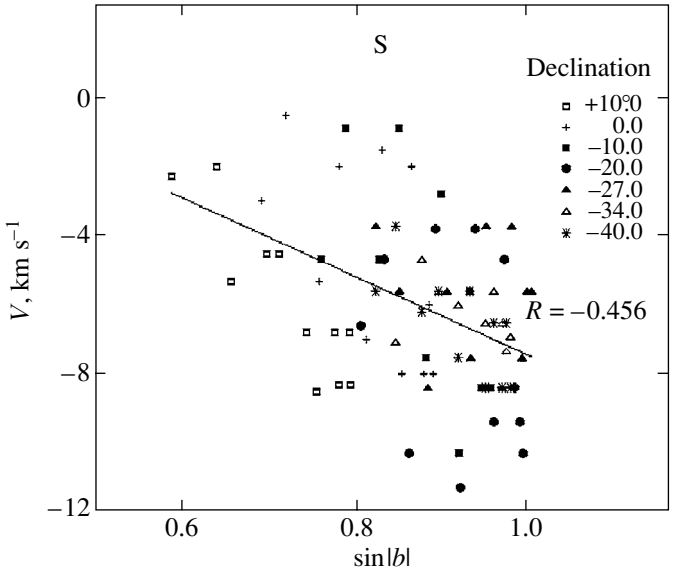

Fig. 1. H I radial velocity versus Galactic latitude in the southern polar cap. The straight line in this and the following figures represents a linear regression, and R is the correlation coefficient between the quantities in the plots.

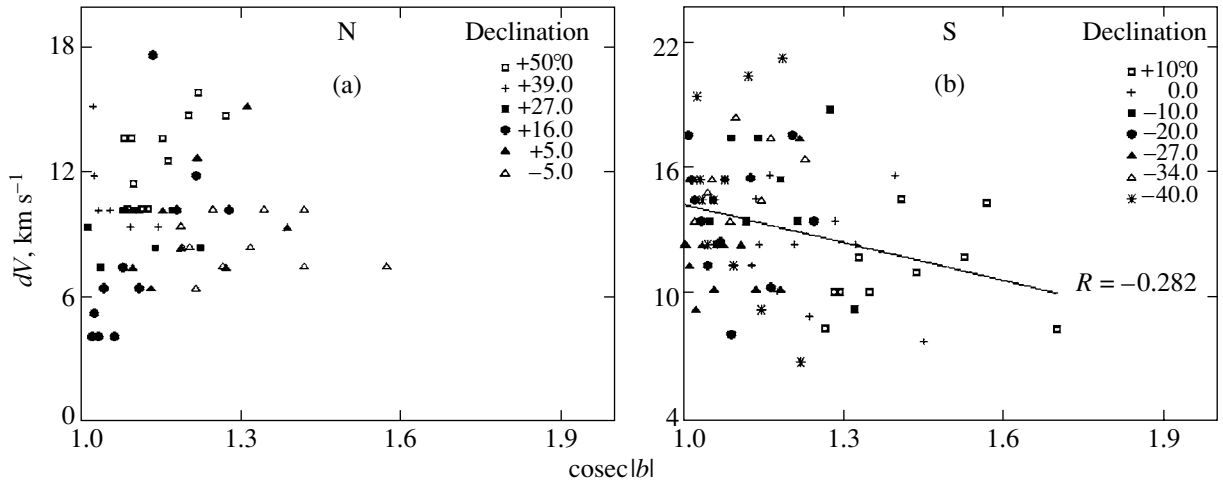

Fig. 2. H I profile FWHMs at low radial velocities versus cosec $|b|$ in the northern (a) and southern (b) polar caps.

do not survive collisions or evaporation in the hot intercloud medium, causing the observed angular spectra to become flatter; on the other hand, a selection effect could also be at work: when the number of small features is large, they are difficult to discern because of the insufficient sensitivity and angular resolution, which cannot be offset by correcting the spectra for smoothing effects.

DISCUSSION

Two distinctly different physical processes are usually invoked to explain the physical nature of the cloud structure of the interstellar medium. One of them, interstellar turbulence, is basically statistical, i.e., the characteristic interstellar gas velocity field leads to turbulent fluctuations in gas density, to what observers commonly call clouds. A description of this physics can be found in many papers, for example, in the fundamental paper by Ballesteros-Paredes *et al.* (1999), which contains a large number of references to other studies.

This approach, which may be attractive mathematically, is often unacceptable for observers for the following simple reason: the cloud structure that arises from turbulence must be hierarchical in principle; i.e., clouds of smaller angular sizes must be within clouds of larger sizes. Unfortunately, there are virtually no observational works that unambiguously re-

Table 3. Mean H I column densities (in units of 10^{20} cm^{-2}) in the southern polar cap

δ	α										
	03^h30^m	03 00	02 30	02 00	01 30	01 00	00 30	00 00	23 30	23 00	22 30
+10°0	2.60	3.50	5.00	4.40	3.80	3.40	3.80	3.90	3.00	2.90	3.6
	9.00	6.40	1.30	0.50	0.30	0.40	0.50	0.20	0.20	0.20	0.50
0.0	1.00	1.30	1.00	1.10	1.30	1.30	2.00	3.50	3.50	4.40	4.50
	5.60	2.70	1.30								
−10.0	0.75	1.50	1.60	1.90	1.80	2.20	2.40	2.30	1.90	2.50	3.20
	3.10	1.60	0.23	0.02							
−20.0	0.99	1.30	0.87	0.53	0.81	1.10	0.87	1.20	1.40	1.50	1.60
	1.30	0.70	0.80	0.45							
−27.0	0.56	0.59	0.58	0.52	0.39	0.58	0.94	0.71	0.77	0.79	0.68
−34.0	0.59	1.15	1.33	1.23	1.24	1.49	0.83	0.66	0.44	0.65	0.43
−40.0	0.17	0.59	0.78	1.20	1.50	2.50	1.70	1.40	1.60	1.90	1.30

Table 4. Indices of the angular H I emission spectrum at low negative radial velocities in the southern polar cap

δ	α										
	03^h30^m	03 00	02 30	02 00	01 30	01 00	00 30	00 00	23 30	23 00	22 30
+10°0	−3.3	−2.8	−3.0	−2.9	−2.7	−2.9	−2.9	−2.5	−2.5	−2.9	−3.0
	0.1	0.2	0.2	0.2	0.3	0.2	0.2	0.2	0.2	0.2	0.2
0.0	−2.8	−2.6	−2.3	−2.4	−2.3	−2.6	−2.5	−2.6	−2.6	−2.5	−2.7
	0.1	0.1	0.3	0.2	0.3	0.2	0.3	0.2	0.2	0.2	0.2
−10.0	−2.8	−3.0	−2.1	−2.4	−2.2	−2.3	−2.0	−2.0	−2.1	−2.6	−2.8
	0.1	0.1	0.2	0.2	0.2	0.2	0.2	0.2	0.2	0.1	0.1
−20.0	−3.0	−2.5	−1.7	−2.7	−2.2	−2.1	−1.9	−1.8	−2.3	−2.4	−2.6
	0.2	0.2	0.3	0.4	0.3	0.2	0.3	0.3	0.2	0.3	0.3
−27.0	−1.9	−1.9	−2.2	−2.3	−2.5	−1.8	−2.7	−2.0	−2.1	−2.2	−2.2
	0.3	0.2	0.3	0.3	0.3	0.3	0.5	0.3	0.2	0.3	0.3
−34.0	−2.7	−2.4	−2.5	−2.3	−1.2	−1.9	−1.5	−2.4	−3.0	−2.7	−2.3
	0.3	0.4	0.2	0.3	0.4	0.3	0.2	0.3	0.2	0.5	0.4
−40.0	−2.7	−2.4	−2.5	−2.3	−1.2	−1.9	−1.5	−2.4	−3.0	−2.7	−2.2
	0.3	0.4	0.2	0.3	0.4	0.3	0.2	0.3	0.2	0.5	0.4

veal such a structure. Clouds of interstellar gas most commonly appear as separate independent objects. In addition, in our case, the problem is complicated by the fact that the observed region cannot be considered to be a thin layer, so the results of theoretical model calculations such as those by Lazarian (1995) or Goldman (2000) are inapplicable.

The long-existing two-stage scenario in which clouds originate from a continuous medium through instabilities of some kind—most commonly the thermal instability that arises after initial contraction of the medium in shock waves—in spiral arms or supernova remnants, is taken as an alternative. Subsequently, the clouds exist in equilibrium with the ex-

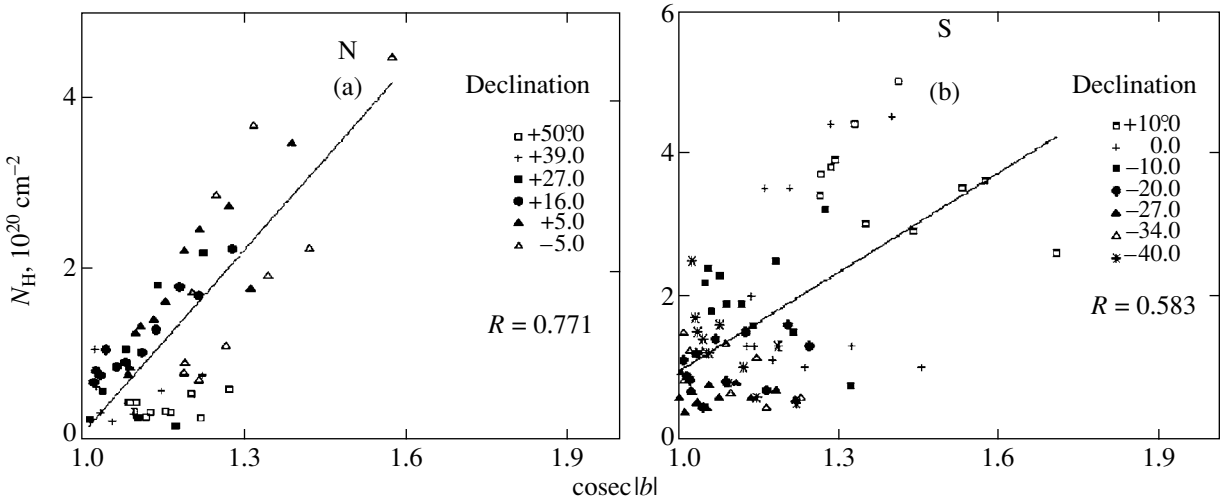

Fig. 3. H I column densities in the northern (a) and southern (b) polar caps.

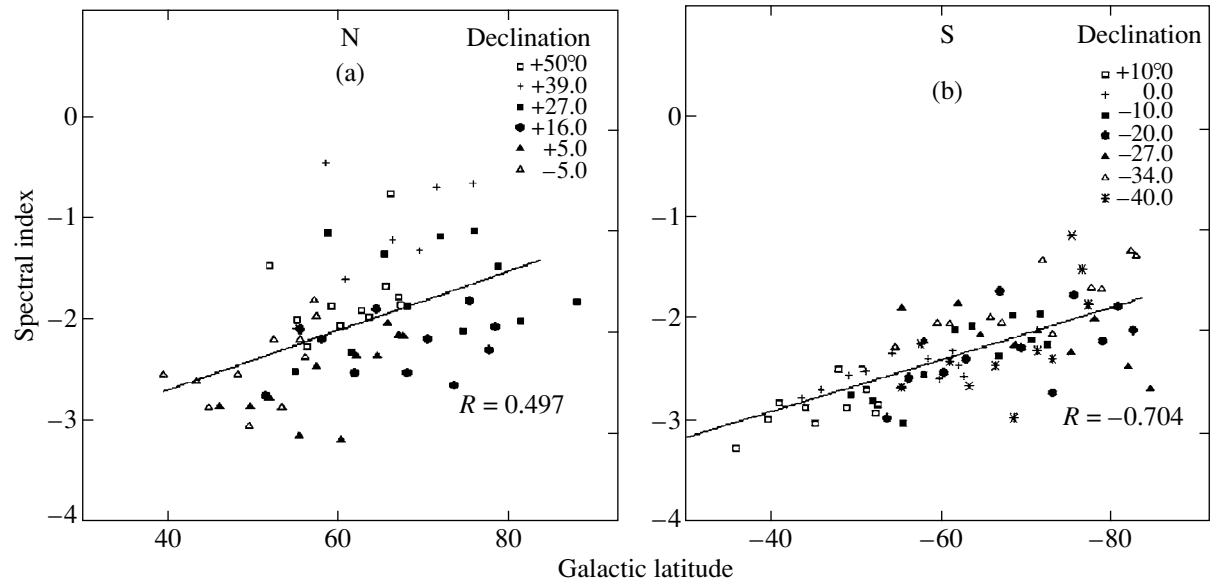

Fig. 4. Indices of the one-dimensional angular H I fluctuation spectra in the northern (a) and southern (b) Galactic polar caps versus Galactic latitude.

ternal intercloud gas pressure, inelastically colliding between themselves. As a result of these collisions, they increase in mass and density until gas molecularization begins and Jeans instability starts working. This scenario has been considered by many authors, so we refer the reader to the monograph by Kaplan and Pikelner (1979) for further information.

Strangely enough, the authors of theoretical works automatically adopt turbulent physics to explain a particular shape of the observed power-law emission spectra for the interstellar gas. To check the possible spectral characteristics of a medium composed of separate objects (clouds) randomly distributed in space with given parameters, we developed an appropriate computer code that simulated the drift curves of the observed medium whose angular spectrum could be obtained by using the same processing software that we applied to the real observations. It immediately became clear that, because of the large extent of the gas layer along the line of sight, the computed angular spectra proved to be close to power-law spectra even if the diameters, densities, and temperatures of the observed objects were fixed. If, however, we use the statistical relations for these parameters derived from observations (see, e.g., Gosachinskii and Morozova 1996, 1999), then we can obtain a wide set of indices for the observed angular fluctuation spec-

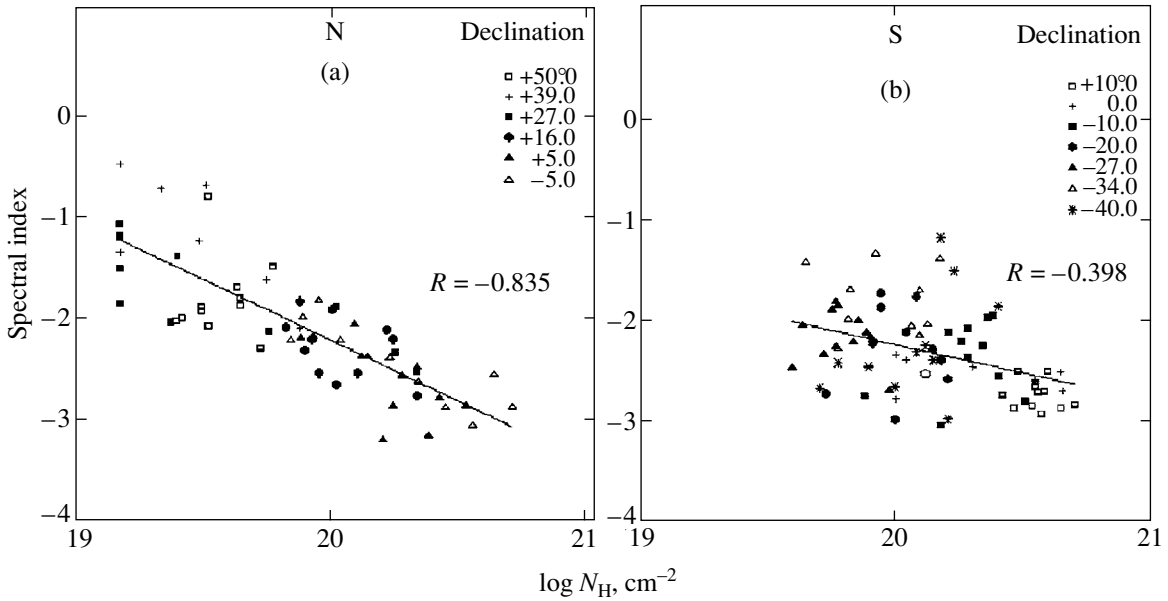

Fig. 5. Indices of the angular spectra versus total H I column density.

trum by choosing appropriate parameters of these relations. Since the number of free parameters in the system of equations was found to be large, choosing the best model takes much time. The results of these computations will be presented in the next paper of this series.

ACKNOWLEDGMENTS

We wish to thank Z.A. Alferova and T.M. Monastyreva from the Special Astrophysical Observatory (Russian Academy of Sciences) for their help with our observations and data reduction. This work was supported by the Russian Foundation for Basic Research (project no. 01-02-17154).

REFERENCES

1. Z. A. Alferova, I. V. Gosachinskii, S. R. Zhelenkov, and A. S. Morozov, Izv. SAO RAN **23**, 89 (1986).
2. J. Ballesteros-Paredes, E. Vasquez-Semadeni, and J. Scalo, Astrophys. J. **515**, 286 (1999).
3. J. Crovisier and J. M. Dickey, Astron. Astrophys. **122**, 282 (1983).
4. J. M. Dickey, N. M. McClure-Griffiths, S. Stanimirivic, *et al.*, Astrophys. J. **561**, 264 (2001).
5. I. Fejes and P. R. Wesselius, Astron. Astrophys. **24**, 1 (1973).
6. I. Goldman, Astrophys. J. **541**, 701 (2000).
7. I. V. Gosachinskii and V. V. Morozova, Astron. Astrophys. Trans. **11**, 215 (1996).
8. I. V. Gosachinskii and V. V. Morozova, Astron. Zh. **76**, 883 (1999) [Astron. Rep. **43**, 777 (1999)].
9. I. V. Gosachinskii, G. N. Il'in, A. S. Morozov, and V. A. Prozorov, Pis'ma Astron. Zh. **25**, 820 (1999) [Astron. Lett. **25**, 712 (1999)].
10. D. A. Green, Mon. Not. R. Astron. Soc. **262**, 327 (1993).
11. D. Hartmann, P. M. W. Kalberla, W. B. Burton, and U. Mebold, Astron. Astrophys., Suppl. Ser. **119**, 115 (1996).
12. C. Heiles, S. Kulkarni, and A. A. Stark, Astrophys. J. Lett. **247**, L73 (1981).
13. G. N. Il'in, V. A. Prozorov, and A. M. Pilipenko, in *Proceedings of the XXVII Radioastronomy Conference: Problems of Modern Radioastronomy* (IPA RAN, St. Petersburg, 1997), p. 128.
14. S. A. Kaplan and S. B. Pikelner, *Physics of the Interstellar Medium* (Nauka, Moscow, 1979) [in Russian].
15. A. Lazarian, Astron. Astrophys. **293**, 507 (1995).
16. A. Lazarian and D. Pogosyan, Astrophys. J. **537**, 720 (2000).
17. R. X. McGee and L. M. Newton, Publ. Astron. Soc. Australia **6**, 358 (1986).
18. A. P. Venger, I. V. Gosachinskii, V. G. Grachev, and N. F. Ryzhkov, Izv. SAO RAN **14**, 118 (1981).
19. A. P. Venger, V. G. Grachev, T. M. Egorova, *et al.,* Soobshch. SAO RAN, No. 35, 5 (1982).
20. A. P. Venger, I. V. Gosachinskii, N. A. Esepkina, *et al.,* in *Proceedings of the XXVII Radioastronomy Conference: Problems of Modern Radioastronomy* (IPA RAN, St. Petersburg, 1997), p. 130.

Translated by V. Astakhov

Astronomy Letters, Vol. 30, No. 4, 2004, pp. 240–246. Translated from Pis'ma v Astronomicheskiĭ Zhurnal, Vol. 30, No. 4, 2004, pp. 277–284.

Nonstationary Radio Luminosity of the Remnant of Supernova 1181 (3C 58)

V. P. Ivanov[1*], I. A. Rakhimov[2], S. G. Smolentsev[2], K. S. Stankevich[1], and A. M. Finkelstein[2]**

[1] *Radiophysical Research Institute, ul. Bol'shaya Pecherskaya 25, GSP-51, Nizhni Novgorod, 603950 Russia*

[2] *Institute of Applied Astronomy, Russian Academy of Sciences, nab. Kutuzova 10, St. Petersburg, 191187 Russia*

Received July 30, 2003

Abstract—We measured the flux densities of the radio source 3C 58, which was identified with the remnant of SN 1181, in April–May 2003 relative to the spectrum of the standard source 3C 295 at four frequencies in the range 1550 to 8450 MHz using the RTF-32 radio telescope at the Svetloe Observatory of the Institute of Applied Astronomy (Russian Academy of Sciences). We found significant nonstationary frequency-dependent flux-density variations in 3C 58 and variations in its instantaneous spectrum. We established that these variations occurred between 1986 and 1998. Based on data for the instantaneous spectra, we show that the break in the spectrum of 3C 58 results from prolonged energy losses by relativistic electrons through synchrotron radiation that took place in a nebula with an age of 5400 yr, equal to the age of the pulsar PSR J0205+6449. SN 1181 is shown to have exploded without the birth of a pulsar, which is characteristic of type-I supernovae. The shock acceleration of relativistic electrons after the explosion may be responsible for the observed nonstantionarity of the flux densities. The long-term evolution of the radio spectrum for the nebula 3C 58 and the nonstationary flux-density variations due to the explosion of SN 1181 are reconciled in terms of a model of an evolved binary system. © *2004 MAIK "Nauka/Interperiodica".*

Key words: *supernovae, supernova remnants, pulsars, age, nonstationary radio emission, instantaneous spectra.*

INTRODUCTION

The radio source 3C 58 has been identified with the remnant of Supernova (SN) 1181 (Clark and Stephenson 1977; Pskovskii 1978). By the structure of its radio brightness distribution, it is classified as a Crab-like supernova remnant. Therefore, it was assumed that the remnant must host a pulsar injecting magnetic fields and relativistic particles into the nebula. The long-term searches for the pulsar were crowned with success only in the past year: the pulsar, with a period of $P = 65.68$ ms, was first discovered in X rays (Murray *et al.* 2002), and then the radio pulsar PSR J0205+6449 was discovered (Camilo *et al.* 2002). It seemed that with the discovery of the pulsar, the energetics of the nebula could be understood. However, serious problems arose precisely at this time. One of these problems is the age of the radio source 3C 58. The dynamical age of the pulsar (5400 yr) determined from its spindown rate (Camilo *et al.* 2002) was found to be incompatible with the age of the remnant of SN 1181. The age problem also arose earlier, particularly, after the mean expansion velocity of the 3C 58 nebula was determined by comparing the VLA images obtained in 1973 and 1998: a dynamical age of 5000 ± 2250 yr corresponds to this velocity (Bietenholz *et al.* 2001). Thus, the ages of the radio nebula and the pulsar proved be almost the same and are a factor of 4 to 5 older than the age of the remnant of SN 1181.

Previously, the flux density of the radio source 3C 58, the only known Galactic supernova remnant, was found to be increasing. This increase characterizes the remnant as a young object with an age much less than 5000 yr. The increase in flux density was observed in 1985–1987 compared to the earlier epoch (1965–1967) and was almost the same at frequencies of 8000 MHz (Aller and Reynolds 1985), 1667 MHz (Aslanyan *et al.* 1987), and 408 MHz (Green 1987). Therefore, the authors interpreted it as a secular increase in the flux density of an evolving young supernova remnant with an age of 820 yr. One might expect an evolutionary rise in luminosity in succeeding years. However, ten years after, in 1996, the flux density at 5000 MHz remained at the 1986 level (Ivanov *et al.* 1997). The following question arose even at

* E-mail: ivnv@nirfi.sci-nnov.ru
** E-mail: stnk@nirfi.sci-nnov.ru

that time: Is the increase in flux density a systematic, evolutionary effect, or is it the effect of random nonstationary variations? Further observations of the instantaneous spectra at subsequent epochs were required to solve this question. For this purpose, we measured the flux densities at several frequencies in April–May 2003 using the RTF-32 radio telescope at the Svetloe Observatory of the Institute of Applied Astronomy (the Russian Academy of Sciences). Our results made it possible to establish the overall pattern of flux-density variations in 3C 58 after 1965, which turned out to be significant and nonstantionary and could be due to the explosion of SN 1181.

It would seem to be very important to search for evolutionary effects in the radio emission from the nebula, particularly those with a long duration, on the order of several thousand years, if the 3C 58 nebula was formed when the pulsar was born. Based on the flux densities at 84.2 GHz (Salter *et al.* 1989) and in the infrared (IRAS), Green and Scheuer (1992) found a break in the spectrum of 3C 58 at 50 GHz. The low frequency of the break, the large difference between the radio and infrared spectral indices ($\Delta\alpha \sim 0.7$), and the short lifetime of the source reckoned from the 1181 explosion did not fit into the known evolutionary models of such sources. Our study of the instantaneous radio spectra for 3C 58 has shown that they change significantly and that a jump in spectral indices by $\Delta\alpha = 0.5$ is possible at a break frequency of 75 GHz. For the nebula age of 5400 yr, which is equal to the pulsar age, the break in the spectrum results from the energy losses of relativistic electrons through synchrotron radiation resulting from continuous injection (Kardashev 1962). We reconciled the long-term evolution of the radio spectrum for the 3C 58 nebula with the nonstationary flux-density variations due to the explosion of SN 1181 in terms of the model of an evolved binary (Bietenholz *et al.* 2001). Our results are presented below, and the parameters of the nebula and the pulsar PSR J0205+6449 are given in Table 1.

RESULTS

In studies of the nonstationarity of emissions from radio sources, errors are reduced by comparing the ratios of the flux densities of the object being studied and a stable calibrator source determined over quite short time intervals at various epochs. The radio emission from the standard source, the radio galaxy 3C 295, is stable: according to the systematic measurements started after 1976, the possible flux-density variations (for 2.8 cm $\leq \lambda \leq$ 21 cm) are less than 1%; its spectrum has been measured with high accuracy (Ott *et al.* 1994). Therefore, we chose 3C 295 as the comparison source to determine the ratios of the flux densities for 3C 58 and 3C 295 at the current and earlier epochs.

We measured the radio flux densities of 3C 58 and 3C 295 using the fully steerable parabolic RTF-32 radio telescope with a diameter of 32 m in May 2002 at 4840 MHz and in April–May 2003 at 1550, 2370, 4840, and 8450 MHz in circular polarization. The basic parameters of the radio telescope are given in our previous papers (Finkelstein 2001; Finkelstein *et al.* 2002; Rakhimov *et al.* 2001). The sources were observed in cycles; each cycle included six to eight pointings at the source. In each cycle we made scans through both sources at 4840 and 8450 MHz. We chose the time of our observations in such a way that the elevation difference between 3C 58 and 3C 295 did not exceed 5°. Three to four comparison cycles were performed at each frequency; as a result, the standard deviation of the peak antenna temperature ratios did not exceed 1.3% at all frequencies. We used the standard technique adopted in flux-density measurements to allow for the partial resolution of 3C 58 by the antenna beam and the possible systematic errors (see, e.g., Ott *et al.* 1994). Table 2 gives the ratios of the flux densities for 3C 58 and 3C 295 at epoch 2003.4 and the corresponding errors. The surveys of discrete sources at 1425 MHz (1965.5) (Fomalont 1968), 2695 MHz (1966.5) (Kellermann *et al.* 1968), and 5000 MHz (1967.0) (Pauliny-Toth and Kellermann 1968) served as the basis for comparison at the earlier epoch. We constructed the relative spectrum $\log\left(\frac{S(3C\,58)}{S(3C\,295)}\right)$ as a function of $\log\nu$ in the frequency ranges 1425–2695 MHz and 2695–5000 MHz and determined $\log\left(\frac{S(3C\,58)}{S(3C\,295)}\right)$ at the frequencies of our measurements at the corresponding epoch by linear interpolation. The results are presented in Table 2.

There is no reason to believe that the radio flux density of 3C 58 during the period 1965–1967 was unperturbed. However, it was the only period in the past when detailed measurements of the flux densities of discrete sources were made in the frequency range under study, from which the relative spectrum could be constructed. In addition, these measurements were used previously as reference data to determine the flux-density variations at 1667 MHz in 1985 (Aslanyan *et al.* 1987) and at 5000 MHz in 1996 (Ivanov *et al.* 1997). The spectral index of the relative spectrum at 2003.4 was $\alpha(3C\,58) - \alpha(3C\,295) = 0.9655 \pm 0.0136$. Its value at the earlier epoch (mid-1960s) was 0.8026 ± 0.0166. The change resulted from a decrease in the slope of the spectrum for 3C 58,

Table 1

Quantities	Values	Authors
Coordinates	R.A. B $02^h01^m53\overset{s}{.}4$; D $+64°35'30''$	Reynolds and Aller (1988)
Galactic coordinates	$l = 130\overset{\circ}{.}73$; $b = 3\overset{\circ}{.}08$	
Distance, kpc	3.2	Roberts *et al.* (1993)
Height above Galactic plane, pc	173	
Size, arcmin	$9' \times 5'$ $10\overset{'}{.}3 \times 6\overset{'}{.}3$	Reynolds and Aller (1988) Bietenholz *et al.* (2001)
Expansion velocity, % per year	0.020 ± 0.008	Bietenholz *et al.* (2001)
Expansion velocity along axes, km s^{-1}	910 ± 360; 550 ± 220	"
Dynamical age, yr	5000 ± 2250	"
Pulsar coordinates, PSR	R.A. B $02^h01^m50\overset{s}{.}16$; D $+64°35'27\overset{''}{.}6$	Murray *et al.* (2002)
Period, ms	65.6863	Camilo *et al.* (2002)
Distance, kpc	3.2	"
$\dot{P}$, s s^{-1}	1.9393×10^{-13}	"
Dynamical age of pulsar, yr	5400	"

Table 2

ν, MHz	$\frac{S(3C\,58)}{S(3C\,295)}(2003.4)$	$\frac{S(3C\,58)}{S(3C\,295)}(1966.5)$	$\frac{S(3C\,58, 2003.4)}{S(3C\,58, 1966.5)}$
1550	1.44 ± 0.03	1.633 ± 0.03	0.882 ± 0.025
2370	2.215 ± 0.04	2.324 ± 0.03	0.953 ± 0.024
4840	4.272 ± 0.13	4.067 ± 0.16	1.05 ± 0.052
8450	7.505 ± 0.3	6.393 ± 0.45	1.174 ± 0.08

which is $\Delta\alpha = 0.163$ at the current epoch. A plot of the relative flux-density variations in 3C 58 at epoch 2003.4 (see Fig. 1) was constructed from the data of Table 2. This plot clearly shows a frequency dependence: an increase in flux at 3.55 and 6.2 cm and a decrease at 12.6 and 19.3 cm. The measured quantities have a high correlation coefficient, $R = 0.997 \pm 0.005$, and their frequency dependence is described by the power law

$$\frac{S(3C\,58, 2003)}{S(3C\,58, 1966)} \propto \nu^{\beta}, \qquad (1)$$

where $\beta = 0.164 \pm 0.02$.

Figure 1 also shows the plot of the relative flux-density variations for 3C 58 at epoch 1985–1986 constructed from published data at 408 MHz (Green 1987), 1667 MHz (Aslanyan *et al.* 1987), and 8000 MHz (Aller and Reynolds 1985). The initial epoch of these measurements is 1965–1968 and corresponds to the initial epoch of our measurements. The correlation coefficient of the measured ratios is $R = 0.811 \pm 0.002$, and they exhibit virtually no frequency dependence ($\beta = -0.0037 \pm 0.0027$); i.e., the flux density of 3C 58 at epoch 1985–1986 increased by 5–6% at all of the frequencies in the range under consideration. Of great interest is the portion of the spectrum for 3C 58 at frequencies near 5000 MHz: in the plot shown in Fig. 1, the data point for 2003 also falls on the 1985–1986 spectrum; Table 3 also gives additional data that show that the flux densities of 3C 58 did not vary after 1986. Undoubtedly, the radio intensity variations of 3C 58 are nonstationary in time and significant in magnitude: not only does the intensity vary, but an energy redistribution over the spectrum of the source also takes place.

Figure 2 shows the instantaneous spectrum of

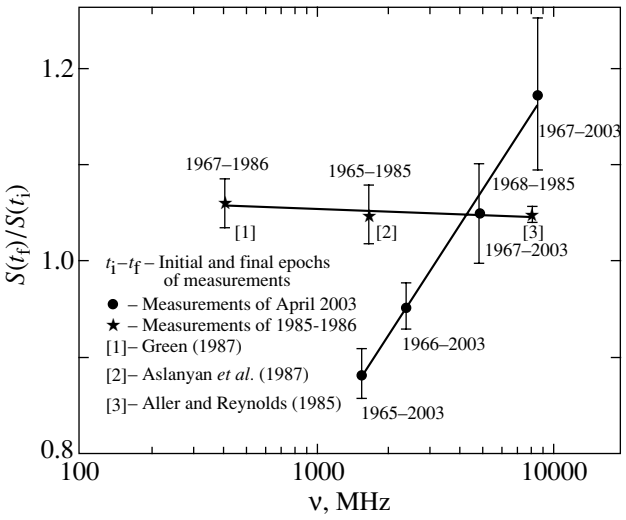

Fig. 1. Relative variations in the flux density of 3C 58.

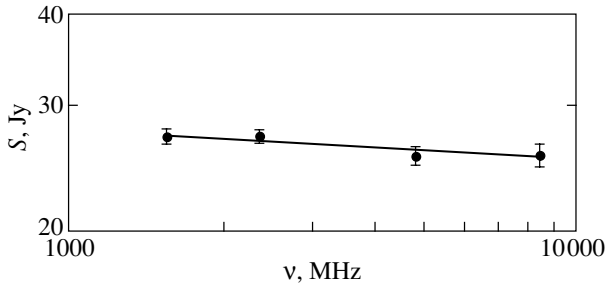

Fig. 2. Instantaneous spectrum of 3C 58 at epoch 2003.4. The spectral index is $\alpha = 0.041 \pm 0.013$.

3C 58 at epoch 2003.4; its spectral index is $\alpha = 0.0413 \pm 0.0133$. Bietenholz *et al.* (2001) measured the spectral index between the frequencies of 327 MHz and 4.9 GHz at epoch 1998 and also found a smaller value of $\alpha = 0.06 \pm 0.03$, which agrees with the above value, within the error limits. Therefore, we may assert that the slope of the spectrum for 3C 58 decreased between 1986 and 1998. We separated three instantaneous spectra from the available data set for epochs 1965–1967, 1985–1986, and 2003.4. The 1965–1967 spectrum is characterized by smaller perturbations both in intensity and in spectral energy distribution; its spectral index is much larger than that for the 2003 spectrum and is equal to $\alpha = 0.20 \pm 0.02$. Note that the data included in the instantaneous spectra yield a total mean spectral index of $\alpha = 0.12 \pm 0.03$. Its value is similar to the published values obtained by averaging the long-term measurements that pertain to different instantaneous spectra: $\alpha = 0.09$ (Wilson and Weiler 1976), $\alpha = 0.09 \pm 0.02$ (Green 1986), $\alpha = 0.1$ (Green and Scheuer 1992), $\alpha = 0.11 \pm 0.01$ (Salter *et al.* 1989), and $\alpha = 0.13 \pm 0.05$ (Green *et al.* 1975). None of the fast variations in the spectrum of 3C 58 mentioned above are evolutionary; their contribution to the luminosity is ~10%.

DISCUSSION

It would seem to be of great importance to search for secular variations in the radio emission from 3C 58. These variations must have occurred, particularly if the nebula has been evolving for a prolonged period on the order of the several thousand years that have elapsed since the birth of the pulsar PSR J0205+6449.

The evolutionary variation in luminosity is determined by the energy losses as the nebula expands and by the energy of the relativistic particles and magnetic fields injected by the pulsar. The adiabatic losses are largest:

$$\frac{1}{L_r}\frac{dL_r}{dt} = -2(2\alpha+1)\frac{\dot{\theta}}{\theta},\ \%/\text{yr}. \qquad (2)$$

The decrease in luminosity (2) is 0.06 %/yr at a yearly expansion rate of $\dot{\theta}/\theta = 0.02\%$ and a spectral index of $\alpha = 0.2$, and must be even smaller if we take into account the injected energy. Thus, the evolutionary decrease in luminosity would be no more than 0.7% after 1965. It is too small to be distinguishable against the background of nonstationary flux-density variations.

Green and Scheuer (1992) found a break in the spectrum of 3C 58 at ~50 GHz between the radio spectrum with a spectral index of $\alpha = 0.1$ and the spectrum with $\alpha(\text{IR}) = 0.8$ that was constructed from the envelope of the upper limits on IRAS infrared fluxes and the flux at 84.2 GHz (Salter *et al.* 1989). The low frequency of the break, the large difference between the radio and infrared spectral indices ($\Delta\alpha \sim 0.7$), and the short lifetime of the source reckoned from the 1181 explosion did not fit into the known evolutionary models of such sources. The currently available data allow us to reconsider some of the aspects in the paper by Green and Scheuer (1992), in particular, the age of the nebula and the adopted spectral indices. Since the instantaneous radio spectrum of the supernova remnant 3C 58 has the form of a slowly evolving component with nonstationary intensity variations superimposed on it, the spectral index of the evolving part of the spectrum could be larger than the measured value. As was noted above, the 1965–1967 spectrum had $\alpha = 0.2$. Given the errors in the spectral indices of the evolving radio spectrum and the IR spectrum, the break may be expected to be close to $\Delta\alpha = 0.5$.

The break in the spectrum of the source with a change in slope of $\Delta\alpha = 0.5$ is evidence of the energy

Table 3

Frequency, MHz	Flux-density variation, %	Interval between measurements	Authors
5000	$+(6.0 \pm 1.8)$	1966–1996	Ivanov *et al.* 1997
4840	$+(6.5 \pm 5.0)$	1967–2002	This paper
4840	$+(5.0 \pm 5.0)$	1967–2003	This paper

losses by relativistic electrons through synchrotron radiation as a result of the continuous, stationary injection of relativistic electrons with a power-law energy spectrum (Kardashev 1962). The break frequency of the evolving spectrum is

$$\nu_{\rm B} = \frac{2.63 \times 10^8}{H^3 t^2}\ {\rm Hz}, \qquad (3)$$

where H is the magnetic-field strength (in G), and t is the time (in yr) elapsed since the onset of injection. For a radio spectral slope of $\alpha = 0.2$, the break frequency shifted toward higher frequencies and is equal to $\nu_{\rm B} = 75$ GHz. Assuming the age of the nebula to be equal to the age of the pulsar ($t = 5400$ yr), from (3) we can estimate the average magnetic-field strength in the nebula, $H = 4.8 \times 10^{-4}$ G. This value is slightly higher than the estimates based on the principle of minimum energy or energy equipartion. For comparison, the break frequency for the Crab nebula is $\nu_{\rm B} = 10^{13}$ Hz, and the average magnetic field is $H = 3 \times 10^{-4}$ G for an age of $t = 948$ yr. Thus, we have reason to believe that the rather low break frequency in the spectrum of 3C 58 is the result of prolonged energy losses by relativistic electrons through synchrotron radiation and is an additional argument for the hypothesis that the nebula existed several thousand years before the explosion of SN 1181, which actually took place inside the nebula.

For comparison, Table 4 gives data on the spectra of 3C 58 and the Crab nebula (3C144) in the frequency range 10^7 to 10^{13} Hz and their luminosities. The fractions of rotational energy lost by the neutron star and transformed into radiation are almost equal for 3C 58 and the Crab nebula, $\approx 7 \times 10^{-3}$, despite the fivefold age difference between the pulsars themselves. This probably implies that both pulsars are at the same energy phase. In the model by Pacini and Salvati (1973), the pulsar transfers energy to the nebula, and the time dependence of the energy is given in the form

$$L(t) = \frac{L_0}{\left(1 + \dfrac{t}{\tau}\right)^s}, \qquad (4)$$

where t is the lifetime of the pulsar, τ is the characteristic spindown time scale, $s = \dfrac{n+1}{n-1} < 3$, and n is the spindown index. For the Crab pulsar, $t = 948$ yr, $s = 2.325$ (Groth 1975), and $\tau = 744$ yr (Bandiera *et al.* 1984), implying that $t/\tau = 1.27$. If we take the same (in order of magnitude) ratio t/τ for the pulsar 3C 58, then we obtain a characteristic spindown time scale of $\tau \approx 4400$ yr. This would imply that the characteristic time scale $\tau \approx P^{2.6}$ also increases with increasing period. The evolutionary processes in 3C 58 must then be similar to those in the Crab nebula, but have a longer time scale ($\sim$5000–6000 yr).

Bietenholz *et al.* (2001) considered several scenarios for the origin and evolution of the nebula 3C 58. Among these, in the opinion of the authors, the following scenario is unlikely: 3C 58 is a complex remnant of a binary where both stars have passed through the stage of supernova explosion; the earlier star produced a slowly expanding remnant, while the later explosion of lower energy was observed in 1181 as the historic supernova explosion event. This scenario received a strong support after the pulsar PSR J0205+6449 was discovered in the supernova remnant 3C 58 and its age was estimated at 5400 yr. SN 1181 exploded inside the earlier supernova remnant that formed the pulsar. Previously, this explosion was identified with a type-II supernova, because the fading of the supernova by four magnitudes in half a year is typical of type-II supernovae (Pskovskii 1985). The nonthermal radio source discovered in 1952 and the Crab-like filamentary nebula discovered in the late 1970s seemingly confirmed that the explosion belonged to type-II supernovae. However, this argument has lost its force in light of the latest developments. Since the low brightness at the maximum of the light curve and its decrease are typical of type-I supernovae (Reynolds and Aller 1988), the type of SN 1181 cannot be unambiguously determined from its light curve. The energy ratios of the nebula and the pulsar in 3C 58 are similar to those of the Crab nebula, which rules out the presence of a second pulsar. Therefore, SN 1181 exploded without giving birth to a pulsar, which is typical of type-I supernovae. The radio-emitting electrons in supernova remnants of this type are known to be produced at the shock front when it collides with external material. How this process occurred when the star exploded inside the remnant of the preceding supernova is a separate question. However, the radio

Table 4

Parameters	3C 58	3C144
S(1 GHz), Jy	30 [1]	990.7 [3]
Spectral index $\alpha(10^7{-}5\times10^{10}$ Hz)	0.1 [1]	0.323 [3]
Break frequency, Hz	5×10^{10}	10^{13}
Spectral index after break in spectrum	0.8 [1]	0.8 [4]
Radio luminosity $L_r(10^7{-}10^{13}$ Hz), erg s^{-1}	1.9×10^{35}	35.7×10^{35}
Distance, kpc	3.2 [2]	2.0
Age, yr	5400 [5]	948
Rotational energy losses by pulsar $(L_{\rm P},$ erg s$^{-1})$	2.7×10^{37}	45.5×10^{37}
$L_r/L_{\rm P}$	7.0×10^{-3}	7.8×10^{-3}
H, G	4.8×10^{-4}	3×10^{-4}

Note: [1]—Green and Scheuer (1992); [2]—Roberts *et al.* (1993); [3]—Ivanov *et al.* (1994); [4]—Marsden *et al.* (1984); [5]—Camilo *et al.* (2002).

emission mechanism of this type must be operating and could be responsible for the observed flux-density nonstationarity and the redistribution of radiation energy in the spectrum of 3C 58. Furthermore, the relativistic electrons produced when the star exploded were added to the nebula; the radio emission of these electrons is observed during the visibility periods of enhanced brightness. Nonstationary variations in the luminosity and the radio spectrum were previously observed in the Crab nebula. These variations were caused by the variations in pulsar activity (Ivanov *et al.* 1994); they may also be typical of Crab-like supernova remnants.

The effects of the explosion of SN 1181 must have been reflected in the nebular structure. VLA imaging at 1446 and 4886 MHz with a resolution of $2''$ and $2''.45$, respectively, has revealed a very complex, intricate filamentary structure in the 3C 58 nebula (Reynolds and Aller 1988). The filaments in bright parts have brightness contrasts ranging from 1.5 to 2 and lengths of $10''{-}30''$; their emissivity is a factor of 40 to 50 higher than the remnant-averaged emissivity. For example, in the image cross section centered at R.A. $02^{\rm h}01^{\rm m}28^{\rm s}.3$ and D $+64^\circ35'30''$, the brightness contrast of a $30''$-wide filament reaches 2.5. Obtaining data on the redistribution of emissions in the filaments and variations in their brightness would be of crucial importance in establishing the mechanism of the nonstationary luminosity of 3C 58.

CONCLUSIONS

(1) We measured the intensity ratios of 3C 58 (the remnant of SN 1181) and the radio galaxy 3C295 used as a standard source at four frequencies in the range 1550 to 8450 MHz in April–May 2003 using the RTF-32 radio telescope at the Svetloe Observatory of the Institute of Applied Astronomy (the Russian Academy of Sciences). These intensity ratios were compared with those at epoch 1965–1967. We found variations in the slope of the instantaneous spectrum for 3C 58 and significant frequency-dependent flux-density variations: a decrease at decimeter wavelengths (by up to 12% at 1550 MHz) and an increase at centimeter wavelengths. We reconstructed the overall pattern of variability in the frequency range under study from available observational data: during the period 1965–1986, the luminosity of 3C 58 increased by 5–6% without any variations in the radio spectral index; the spectral index decreased between 1986 and 1998 and is currently equal to $\alpha = 0.041 \pm 0.013$. All of the detected variations are nonstationary and result from the shock acceleration of relativistic electrons after the explosion of SN 1181.

(2) We have shown that the break in the spectrum of 3C 58 discovered by Green and Sheuer (1992) is attributable to the energy losses by relativistic electrons through synchrotron radiation for the nebula age of $t = 5400$ yr, which is equal to the age of the pulsar PSR J0205+6449. This fact is further evidence that the 3C 58 nebula was formed several thousand years before the explosion of SN 1181, which actually took place inside the nebula.

(3) We showed that the fraction of rotational energy lost by the neutron star and transformed into radio emission in the frequency range $10^7{-}10^{13}$ Hz

is virtually the same for 3C 58 and the Crab nebula, ~0.7%. Hence, two corollaries follow:

(a) Despite the fivefold age difference between the pulsars in 3C 58 and the Crab nebula, they are in the same energy phase;

(b) There is no second pulsar in the 3C 58 nebula, and SN 1181 exploded without giving birth to a pulsar.

(4) We have reconciled the long-term evolution of the radio spectrum for the 3C 58 nebula and the nonstationary flux-density variations due to the explosion of SN 1181 in terms of the model of an evolved binary (Bietenholz *et al.* 2001).

ACKNOWLEDGMENTS

This work was supported in part by the Russian Foundation for Basic Research (project no. 01-02-16635) and the Council for the Support of Leading Scientific Schools (project no. NSh-1483.2003.2)

REFERENCES

1. H. D. Aller and S. P. Reynolds, *Crab Nebula and Related Supernova Remnants,* Ed. by M. C. Kafatos and R. Henry (Cambridge Univ. Press, Cambridge, 1985), p. 75.
2. A. M. Aslanyan, A. G. Gulyan, V. P. Ivanov, *et al.*, in *Proceedings of the XIX All-Union Radio Astronomy Conference, Tallin, USSR, 1987*, p. 154.
3. R. Bandiera, F. Pacini, and M. Salvati, Astrophys. J. **285**, 134 (1984).
4. M. F. Bietenholz, N. E. Kassim, and K. W. Weiler, Astrophys. J. **560**, 772 (2001).
5. F. Camilo, I. H. Stairs, D. R. Lorimer, *et al.*, Astrophys. J. **571**, L41 (2002).
6. D. H. Clark and F. R. Stephenson, *The Historical Supernovae* (Pergamon, Oxford, 1977).
7. A. M. Finkelstein, Nauka Ross. **5**, 20 (2001).
8. A. Finkelstein, A. Ipatov, and S. Smolentsev, *4th APSGP Workshop,* Ed. by H. Cheng and Q. Zhi-han (Shanghai Sci. Techn., Shanghai, 2002), p. 47.
9. E. B. Fomalont, Astrophys. J., Suppl. Ser. **15**, 203 (1968).
10. D. A. Green, Mon. Not. R. Astron. Soc. **218**, 533 (1986).
11. D. A. Green, Mon. Not. R. Astron. Soc. **225**, 11 (1987).
12. A. J. Green, J. R. Baker, and T. L. Landecker, Astron. Astrophys. **44**, 187 (1975).
13. D. A. Green and P. A. G. Scheuer, Mon. Not. R. Astron. Soc. **258**, 833 (1992).
14. E. J. Groth, Astrophys. J., Suppl. Ser. **29**, 453 (1975).
15. V. P. Ivanov, K. S. Stankevich, and S. P. Stolyarov, Astron. Zh. **71**, 737 (1994).
16. V. P. Ivanov, A. M. Aslanyan, K. S. Stankevich, *et al.*, in *Proceedings of the XXVII Radio Astronomy Conference, St. Petersburg, 1997*, Vol. 1, p. 136.
17. N. S. Kardashev, Astron. Zh. **39**, 393 (1962) [Sov. Astron. **6**, 317 (1962)].
18. K. I. Kellermann, I. I. K. Pauliny-Toth, and W. C. Tyler, Astron. J. **73**, 298 (1968).
19. P. L. Marsden, F. C. Gillett, R. E. Jennings, *et al.*, Astrophys. J. **278**, L29 (1984).
20. S. S. Murray, P. O. Slane, F. D. Seward, *et al.*, Astrophys. J. **568**, 226 (2002).
21. M. Ott, A. Witzel, A. Quirrenbach, *et al.*, Astron. Astrophys. **284**, 331 (1994).
22. I. I. K. Pauliny-Toth and K. I. Kellermann, Astron. J. **73**, 953 (1968).
23. F. Pacini and M. Salvati, Astrophys. J. **186**, 249 (1973).
24. Yu. P. Pskovskii, Astron. Zh. **55**, 737 (1978) [Sov. Astron. **22**, 201 (1978)].
25. Yu. P. Pskovskii, *Novae and Supernovae* (Nauka, Moscow, 1985) [in Russian].
26. I. A. Rakhimov, Sh. B. Akhmedov, A. A. Zborovskiĭ, *et al.*, in *Proceedings of the All-Russian Astronomical Conference, St. Petersburg, 2001*, p. 152.
27. S. P. Reynolds and H. D. Aller, Astrophys. J. **327**, 845 (1988).
28. D. A. Roberts, W. M. Goss, P. M. W. Kalberla, *et al.*, Astron. Astrophys. **274**, 427 (1993).
29. C. J. Salter, S. P. Reynolds, D. E. Hogg, *et al.*, Astrophys. J. **338**, 171 (1989).
30. A. S. Wilson and K. W. Weiler, Astron. Astrophys. **49**, 357 (1976).

Translated by A. Dambis

Astronomy Letters, Vol. 30, No. 4, 2004, pp. 247–250. Translated from Pis'ma v Astronomicheskiĭ Zhurnal, Vol. 30, No. 4, 2004, pp. 285–288.

Detection of Giant Pulses from the Pulsar PSR B0031−07

A. D. Kuzmin*, A. A. Ershov, and B. Ya. Losovsky*****

Pushchino Radio Astronomy Observatory, Astrospace Center, Lebedev Institute of Physics, Russian Academy of Sciences, Pushchino, Moscow oblast, 142290 Russia

Received September 11, 2003

Abstract—Giant pulses have been detected from the pulsar PSR B0031−07. A pulse with an intensity higher than that of the average pulse by a factor of 50 or more is encountered approximately once per 300 observed periods. The peak flux density of the strongest pulse was 530 Jy, which is a factor of 120 higher than the peak flux density of the average pulse. The giant pulses are a factor of 20 narrower than the integrated profile and are clustered about its center. © *2004 MAIK "Nauka/Interperiodica"*.

Key words: *pulsars and black holes, neutron stars, giant pulses, PSR B0031−07.*

INTRODUCTION

Giant pulses (GPs), which are short-duration outbursts of pulsar radio emission, are rare events that have been observed only in five pulsars: the Crab pulsar PSR B0531+21 (Staelin and Sutton 1970), the millisecond pulsars PSR B1937+21 (Wolszczan *et al.* 1984) and PSR B1821−24 (Romani and Johnston 2001), the pulsar PSR B1112+50 (Ershov and Kuzmin 2003), and the extragalactic pulsar in the Large Magellanic Cloud PSR B0540−69 (Johnston and Romani 2003).

For normal pulsars, the intensity of their individual pulses exceeds that of the average pulse by no more than several times. The GPs from the Crab pulsar PSR B0531+21 (Kostyuk *et al.* 2003), the extragalactic pulsar PSR B0540−69 in the Large Magellanic Cloud (Johnston and Romani 2003), and the millisecond pulsar PSR B1937+21 (Wolszczan *et al.* 1984; Cognard *et al.* 1996) exceed in intensity the average level by factors of 70 000, 5000, and 300, respectively; for the pulsars PSR B1112+50 and PSR B1821−24, this excess reaches a factor of 80 (Ershov and Kuzmin 2003; Romani and Johnston 2001).

Kuzmin and Losovsky (2002), Kostyuk *et al.* (2003), and Hankins *et al.* (2003) have found extremely high brightness temperatures, $T_B \sim 10^{35}$–10^{37} K, for the GPs from the millisecond pulsar PSR B1937+21 and the Crab pulsar PSR B0531+21.

The characteristic features of the GPs also include their short duration, stable position, and the pattern of their intensity distribution. The GP duration is much shorter than that of the integrated profiles for these pulsars. The GPs are localized within a small part of the integrated profile. The intensity has a two-component distribution: lognormal for most of the pulses and a power law $N \propto S^{\alpha}$ for pulses with an intensity higher than a certain level, i.e., for GPs (Lundgren *et al.* 1995). The boundary at which the pattern of the distribution changes corresponds to an approximately 30-fold intensity of the average pulse.

Attempts to detect GPs from other pulsars (Phinney and Taylor 1979; Johnston and Romani 2002; McLaughlin and Cordes 2003) have so far failed.

We have detected GPs from the pulsar PSR B0031−07.

OBSERVATIONS AND DATA REDUCTION

The observations were carried out from April 19 through August 10, 2003, with the BSA radio telescope at the Pushchino Radio Astronomy Observatory (Astrospace Center of the Lebedev Institute of Physics, Russian Academy of Sciences). Only linear polarization was received. We used a 128-channel receiver with the channel bandwidth $\Delta f = 20$ kHz. The frequency of the first (highest-frequency) channel was 111.870 MHz. The sampling interval was 0.819 ms, and the time constant $\tau = 1$ ms. The observations were performed in the mode of recording individual pulses. The duration of one observing session was about 3 min. We observed 205 pulsar periods in a session.

Over the above time interval, we conducted a total of 56 observing sessions containing 11 480 pulsar periods. We detected 43 pulses with peak flux densities

*E-mail: akuzmin@prao.psn.ru
**E-mail: ershov@prao.psn.ru
***E-mail: blos@prao.psn.ru

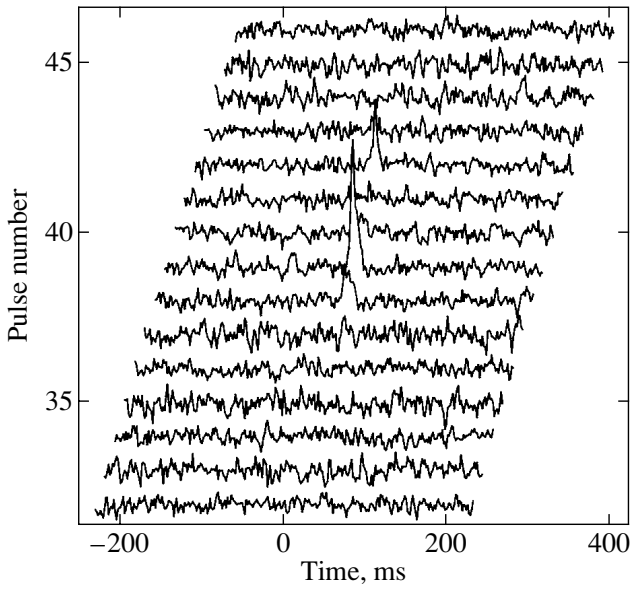

Fig. 1. Example of a GP from the pulsar PSR B0031−07.

exceeding the peak flux density of the average pulse (for all of the 56 days of observations) by more than a factor of 50 (one pulse per 270 observed periods). A sample record of a giant pulse is shown in Fig. 1.

Figure 2 shows the strongest observed GP in comparison with the integrated pulsar profile for all of the days of observations. The peak flux density of this GP is a factor of 120 higher than that of the average pulse. For convenient examination, the integrated profile was magnified by a factor of 100, and the flux densities of the GP and the integrated profile are indicated on the left- and right-hand scales of the vertical axes. The measured GP duration is $w_{\rm GP50} = 5 \pm 1$ ms. The duration of the integrated pulsar profile is $w_{50} = 110$ ms $= 115$ mP $= 42°$ (at half maximum[1]). Thus, the GP is approximately a factor of 20 narrower than the integrated profile, which is also typical of GPs.

This figure also shows the phases of the 43 observed GPs whose peak flux density exceeds that of the average pulse by more than a factor of 50. The temporal positions of the GPs are stable; they are clustered about the middle of the first component of the integrated profile. The phase difference between the GP centroid and the integrated profile is $\Phi_{\rm GP} - \Phi_{\rm Av} = -6° \pm 4° = (-0.12 \pm 0.09) \times w_{50}$.

[1] The pulse duration was determined at half maximum for each component of the two-component pulsar profile.

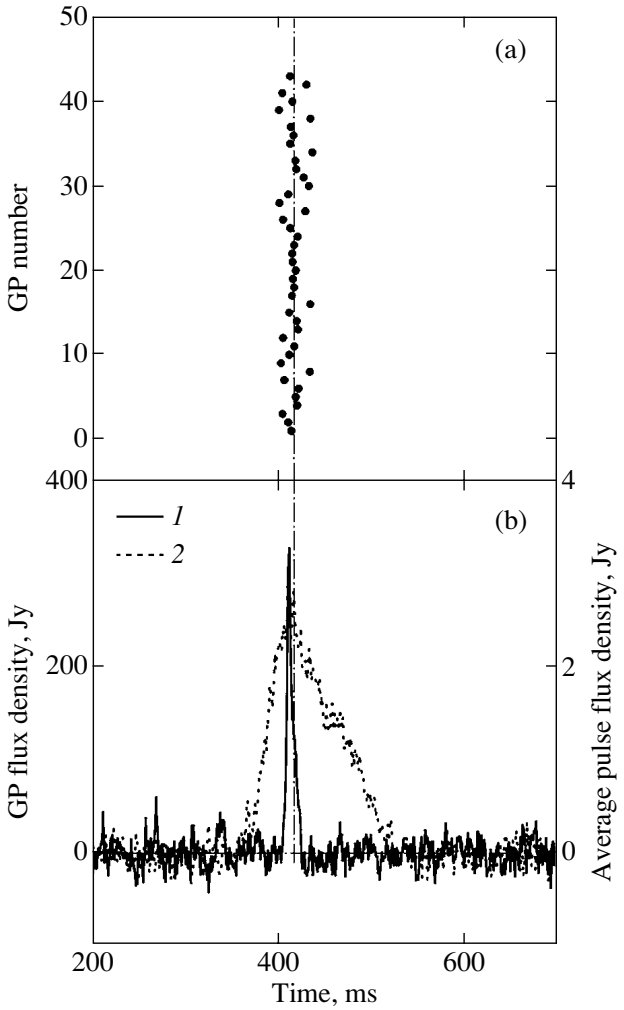

Fig. 2. (a) Phases of the 43 observed GPs with peak flux densities exceeding the peak flux density of the average pulse by more than a factor of 50. (b) The strongest GP (*1*) together with the integrated profile (*2*), which was magnified by a factor of 100.

We determined the GP flux density by a comparison with the average pulse of this pulsar with a known (period-averaged) flux density S. At a close frequency of 102 MHz, the flux density of the average pulse is $S = 400$ mJy (Izvekova *et al.* 1981); for the spectral index $\alpha = 1.75$, this value corresponds to $S = 350$ mJy at the frequency of our measurements, 111 MHz. The peak flux density of the average pulse is

$$S_{\rm Av}^{\rm max} = S/k_{\rm shape} = 4.4 \text{ Jy},$$

where S is the period-averaged flux density of the average pulse, and $k_{\rm shape} = 0.08$ is the scaling ratio of the period-averaged flux density of the pulsar to the peak flux density of the pulse with allowance made for the shape of the integrated profile. The GP peak flux

density is

$$S_{\rm GP}^{\rm max} = S_{\rm Av}^{\rm max} \times (I_{\rm GP}/I_{\rm Av}),$$

where $I_{\rm GP}/I_{\rm Av}$ is the observed intensity ratio of the giant pulse and the integrated profile. For the strongest GP, $I_{\rm GP}/I_{\rm Av} = 120$, which corresponds to the peak flux density $S_{\rm GP}^{\rm max} = 530$ Jy.

The GP brightness temperature is

$$T_{\rm B} = S\lambda^2/2k\Omega,$$

where λ is the wavelength of the received radio emission, k is the Boltzmann constant, and Ω is the solid angle of the radio-emitting region. Assuming the size of the radio-emitting region to be $\ell \le c \times w_{\rm GP50}$, where c is the speed of light, and the pulsar distance to be $d = 0.68$ kpc (Taylor *et al.* 1995), for $w_{\rm GP50} =$ 5 ms and $S = 530$ Jy we obtain $T_{\rm B} \ge 10^{26}$ K.

The GPs that we detected are not the result of scintillations. The characteristic scintillation timescale in the interstellar medium (the radius of the time correlations) for a pulsar with a dispersion measure $DM = 10.89$ pc $\times$ cm^{-3} at the frequency of our observations, 111 MHz, is $\approx$1 min and $\approx$1000 d, respectively, for refractive and diffractive scintillations (Shishov *et al.* 1995). This time scale significantly exceeds the lifetimes of the observed GPs (no more than a few seconds).

DISCUSSION

The GPs that we detected from the pulsar PSR B0031−07 exhibit characteristic features of the classical giant pulses from the pulsars PSR B0531+21 and PSR B1937+21. The GP peak intensity exceeds that of the average pulse by more than a factor of 100. The GPs are much narrower than the integrated profile, and their positions within the integrated profile are stable.

The absence in our observations of GPs exceeding in intensity the average pulse by more than a factor of 120, which were observed for the pulsars PSR B0531+21 and PSR B1937+21, may be attributable to the relatively small (because of the long period of the pulsar PSR B0031−07) number of observed periods (11 480 compared to more than 10^6 periods for PSR B0531+21 and PSR B1937+21). For these pulsars, pulses exceeding in intensity the average level by a factor of 100 are observed once per approximately 10^5 pulses.

Note that the pulsar PSR B0031−07, like PSR B1112+50 that we detected previously (Ershov and Kuzmin 2003), does not belong to the group of pulsars with the strongest magnetic fields on the light cylinder ($B_{\rm LC} \simeq 10^6$ G), which are considered to be most promising for the search of GPs. For the pulsars PSR B0031−07 and PSR B1112+50, the magnetic fields on the light cylinder $B_{\rm LC}$ are $\simeq$5 G. This may be a different class of GPs.

The observed GP localization within a small part of the integrated profile suggests that the GP radiation beam is much narrower than the beam of the integrated profile. Hence, the probability of "seeing" a pulsar GP is much lower than the probability of seeing normal, broader pulses. Therefore, the number of observed pulsars with GPs must be much smaller than the number of observed normal pulsars.

CONCLUSIONS

We have detected GPs from the pulsar PSR B0031−07. At 111 MHz, the peak flux density of the strongest pulse is about 500 Jy, which is more than a factor of 100 higher than the peak flux density of the average pulse. Pulses for which the peak intensity exceeds the peak intensity of the average pulse by more than a factor of 50 are encountered approximately once per 300 periods. The GPs are a factor of about 20 narrower than the integrated profile and are clustered in the middle part of the integrated profile. The brightness temperature of the observed GPs is $T_{\rm B} \ge 10^{26}$ K.

ACKNOWLEDGMENTS

We wish to thank V.V. Ivanova, K.A. Lapaev, V.D. Pugachev, and A.S. Aleksandrov for their software and technical support of the observations. This work was supported in part by the Russian Foundation for Basic Research (project no. 01-02-16326) and the Program of the Presidium of the Russian Academy of Sciences for the Study of the Nature of Nonstationary Phenomena in Astrophysical Objects in Various Ranges of the Electromagnetic Spectrum.

REFERENCES

1. J. Cognard, J. A. Shrauner, J. H. Taylor, and S. E. Thorsett, Astrophys. J. Lett. **457**, L81 (1996).
2. A. A. Ershov and A. D. Kuzmin, Pis'ma Astron. Zh. **29**, 111 (2003) [Astron. Lett. **29**, 91 (2003)].
3. T. H. Hankins, J. S. Kern, J. C. Weatherall, and J. A. Eilek, Nature **422**, 141 (2003).
4. V. A. Izvekova, A. D. Kuzmin, V. M. Malofeev, and Yu. P. Shitov, Astrophys. Space. Sci. **78**, 45 (1981).
5. S. Johnston and R. W. Romani, Mon. Not. R. Astron. Soc. **332**, 109 (2002).
6. S. Johnston and R. W. Romani, Astrophys. J. Lett. **590**, L95 (2003).
7. S. V. Kostyuk, I. V. Kondrat'ev, A. D. Kuzmin, *et al.,* Pis'ma Astron. Zh. **29**, 440 (2003) [Astron. Lett. **29**, 387 (2003)].

8. A. D. Kuzmin and B. Ya. Losovsky, Pis'ma Astron. Zh. **28**, 25 (2002) [Astron. Lett. **28**, 21 (2002)].
9. S. C. Lundgren, J. M. Cordes, M. Ulmer, *et al.*, Astrophys. J. **453**, 433 (1995).
10. M. A. McLaughlin and J. M. Cordes, Astrophys. J. **596**, 982 (2003).
11. S. Phinney and J. H. Taylor, Nature **277**, 117 (1979).
12. R. W. Romani and S. Johnston, Astrophys. J. Lett. **557**, L93 (2001).
13. D. H. Staelin and J. M. Sutton, Nature **226**, 69 (1970).
14. V. I. Shishov, V. M. Malofeev, A. V. Pynzar', and T. V. Smirnova, Astron. Zh. **72**, 485 (1995) [Astron. Rep. **39**, 428 (1995)].
15. J. H. Taylor, R. N. Manchester, A. G. Lyne, *et al.*, *Catalog of 706 Pulsars* (1995) (unpublished work).
16. A. Wolszczan, J. M. Cordes, and D. R. Stinebring, *Millisecond Pulsars,* Ed. by S. P. Reynolds and D. R. Stinebring (NRAO, Green Bank, 1984), p. 63.

Translated by G. Rudnitskiĭ

Astronomy Letters, Vol. 30, No. 4, 2004, pp. 251–257. Translated from Pis'ma v Astronomicheskiĭ Zhurnal, Vol. 30, No. 4, 2004, pp. 289–296.

Kinematic Control of the Inertiality of ICRS Catalogs

V. V. Bobylev*

Pulkovo Astronomical Observatory, Russian Academy of Sciences,
Pulkovskoe shosse 65, St. Petersburg, 196140 Russia

Received July 16, 2003

Abstract—We perform a kinematic analysis of the Hipparcos and TRC proper motions of stars by using a linear Ogorodnikov–Milne model. All of the distant ($r > 0.2$ kpc) stars of the Hipparcos catalog have been found to rotate around the Galactic y axis with an angular velocity of $M_{13}^- = -0.36 \pm 0.09$ mas yr^{-1}. One of the causes of this rotation may be an uncertainty in the lunisolar precession constant adopted when constructing the ICRS. In this case, the correction to the IAU (1976) lunisolar precession constant in longitude is shown to be $\Delta p_1 = -3.26 \pm 0.10$ mas yr^{-1}. Based on the TRC catalog, we have determined the mean Oort constants: $A = 14.9 \pm 1.0$ and $B = -10.8 \pm 0.3$ km s^{-1} kpc^{-1}. The component of the model that describes the rotation of all TRC stars around the Galactic y axis is nonzero for all magnitudes, $M_{13}^- = -0.86 \pm 0.11$ mas yr^{-1}. © *2004 MAIK "Nauka/Interperiodica".*

Key words: *Galaxy (Milky Way), astronomical constants, ICRS.*

INTRODUCTION

Based on the Ogorodnikov–Milne model and using the proper motions of stars, Clube (1972, 1973), du Mont (1977, 1978), and Miyamoto and Sôma (1993) modeled the Galactic rotation. This modeling showed that, apart from the Galactic rotation parameters, it is possible to control the inertiality of the catalogs being analyzed and to refine the adopted precession constant. Here, instead of the currently popular method for solving the Ogorodnikov–Milne model equations using parallaxes, we use a method for determining the kinematic parameters of the Galactic rotation that is completely free from parallax errors to analyze Hipparcos data (ESA 1997). In this method, the parallactic factor is assumed to be equal to unity. First, this assumption makes it possible to analyze stars even with negative parallaxes (the Hipparcos catalog). Second, since the proper motions of TRC stars (Hfig *et al.* 1998) can be analyzed in full only by this method, this approach yields comparable data for both ICRS catalogs (International Celestial Reference System). The kinematic method for controlling the inertiality of the catalogs of stellar proper motions is based on the analysis of the two components of the rigid-rotation tensor that describe the rotation about the Galactic y and x axes in the Galactic coordinate system.

*E-mail: vbobylev@gao.spb.ru

BASIC EQUATIONS

In this paper, we use a rectangular Galactic coordinate system with the axes directed away from the observer toward the Galactic center ($l = 0°$, $b = 0°$, the x axis), along the Galactic rotation ($l = 90°$, $b = 0°$, the y axis), and toward the North Galactic Pole ($b = 90°$, the z-axis). In the Ogorodnikov–Milne model, we use the notation introduced by Clube (1972, 1973) and employed by du Mont (1977, 1978). When using only the stellar proper motions, one of the diagonal terms of the deformation matrix is known (Ogorodnikov 1965) to remain indeterminate. It is possible to determine the differences between the diagonal elements of the deformation matrix, for example, in the form $(M_{11}^+ - M_{22}^+)$ and $(M_{33}^+ - M_{22}^+)$. In this approach, the basic equations can be written as

$$\mu_l \cos b = (1/r)(X_\odot \sin l - Y_\odot \cos l) \quad (1)$$
$$- M_{32}^- \cos l \sin b - M_{13}^- \sin l \sin b + M_{21}^- \cos b$$
$$+ M_{12}^+ \cos 2l \cos b - M_{13}^+ \sin l \sin b$$
$$+ M_{23}^+ \cos l \sin b - 0.5(M_{11}^+ - M_{22}^+) \sin 2l \cos b,$$
$$\mu_b = (1/r)(X_\odot \cos l \sin b + Y_\odot \sin l \sin b \quad (2)$$
$$- Z_\odot \cos b) + M_{32}^- \sin l - M_{13}^- \cos l$$
$$- 0.5 M_{12}^+ \sin 2l \sin 2b + M_{13}^+ \cos l \cos 2b$$
$$+ M_{23}^+ \sin l \cos 2b - 0.5(M_{11}^+ - M_{22}^+) \cos^2 l \sin 2b$$
$$+ 0.5(M_{33}^+ - M_{22}^+) \sin 2b,$$

where $X_\odot$, $Y_\odot$, and $Z_\odot$ are the velocity components of the peculiar solar motion, and M_{12}^-, M_{13}^-, and M_{23}^-

1063-7737/04/3004-0251$26.00

Table 1. Kinematic parameters inferred from the proper motions of Hipparcos stars

Parameter	1	2	3	4	5	6	7	8
$\bar{r}$, kpc	0.074	0.142	0.243	0.361	0.570	1.2	∼2	>0.2
$N_\star$	13453	29378	20032	16040	11441	10015	3833	58675
$X_\odot$	25.32 ± 0.70	14.27 ± 0.25	8.10 ± 0.17	6.05 ± 0.14	4.53 ± 0.13	3.56 ± 0.11	2.23 ± 0.19	5.89 ± 0.08
$Y_\odot$	47.97 ± 0.69	23.24 ± 0.13	13.37 ± 0.18	10.24 ± 0.15	8.06 ± 0.14	6.75 ± 0.13	5.81 ± 0.18	10.22 ± 0.08
$Z_\odot$	18.59 ± 0.68	10.04 ± 0.24	5.66 ± 0.16	4.27 ± 0.13	3.23 ± 0.12	2.49 ± 0.10	2.03 ± 0.16	4.10 ± 0.07
$V_\odot$	20.1 ± 0.2	19.6 ± 0.2	19.1 ± 0.2	21.6 ± 0.2	26.4 ± 0.4	45.7 ± 0.7	$\sim 62.0 \pm 1.7$	22.0 ± 0.1
$L_\odot$	62.2 ± 0.7	58.6 ± 0.5	58.8 ± 0.6	59.4 ± 0.7	60.6 ± 0.8	62.2 ± 0.9	69.0 ± 1.7	60.0 ± 0.4
$B_\odot$	18.9 ± 0.7	20.2 ± 0.5	19.9 ± 0.6	19.8 ± 0.6	19.3 ± 0.7	18.0 ± 0.9	18.1 ± 1.4	19.2 ± 0.3
M_{12}^+	2.40 ± 0.86	2.20 ± 0.30	2.96 ± 0.21	2.85 ± 0.17	2.77 ± 0.16	2.91 ± 0.14	2.48 ± 0.21	2.90 ± 0.09
M_{32}^-	-0.18 ± 0.70	0.06 ± 0.25	-0.15 ± 0.18	-0.10 ± 0.15	0.07 ± 0.14	-0.11 ± 0.13	-0.53 ± 0.21	-0.16 ± 0.08
M_{13}^-	-2.44 ± 0.69	-1.06 ± 0.25	-0.62 ± 0.18	-0.15 ± 0.15	-0.24 ± 0.15	-0.18 ± 0.13	-0.68 ± 0.21	-0.36 ± 0.09
M_{21}^-	-2.40 ± 0.68	-2.47 ± 0.24	-3.01 ± 0.16	-3.03 ± 0.13	-3.00 ± 0.12	-2.85 ± 0.10	-2.76 ± 0.16	-2.93 ± 0.07
$M_{11}^+ - M_{22}^+$	0.08 ± 1.76	-2.13 ± 0.62	-2.00 ± 0.42	-1.40 ± 0.34	-1.16 ± 0.32	-1.50 ± 0.27	-0.62 ± 0.41	-1.35 ± 0.19
M_{13}^+	-4.01 ± 0.92	-0.56 ± 0.33	-0.10 ± 0.23	-0.12 ± 0.20	-0.14 ± 0.19	-0.07 ± 0.17	-0.75 ± 0.25	-0.11 ± 0.11
M_{23}^+	-1.38 ± 0.92	-0.58 ± 0.33	0.41 ± 0.23	-0.03 ± 0.19	-0.20 ± 0.18	0.14 ± 0.16	0.49 ± 0.25	0.13 ± 0.10
$M_{33}^+ - M_{22}^+$	-1.65 ± 1.73	-1.33 ± 0.63	-0.61 ± 0.44	0.17 ± 0.37	-0.07 ± 0.36	-0.24 ± 0.33	-0.39 ± 0.52	-0.14 ± 0.21
l_{xy}	-1 ± 11	13 ± 4	9 ± 2	7 ± 2	6 ± 2	7 ± 1	4 ± 2	7 ± 1

Note: $\bar{r}$ is the mean distance, $N_\star$ is the number of stars, the coordinates of the solar apex $L_\odot$ and $B_\odot$ and the vertex l_{xy} are in degrees, $V_\odot$ is the solar velocity in km s^{-1}; all of the remaining quantities are in mas yr^{-1}.

are the vector components of the rigid rotation of an infinitesimal solar neighborhood around the corresponding axes. In accordance with the adopted rectangular coordinate system, the following rotations are positive: from axis 1 to axis 2, from axis 2 to axis 3, and from axis 3 to axis 1. The quantity M_{21}^- is an analogue of the Oort constant B. Each of the quantities M_{12}^+, M_{13}^+, and M_{23}^+ describes the deformation in the corresponding plane. The quantity M_{12}^+ is an analogue of the Oort constant A. The diagonal components of the deformation tensor M_{11}^+, M_{22}^+, and M_{33}^+ describe the overall contraction or expansion of the entire stellar system. Equations (1)–(2) contain eleven unknowns that can be determined by the least-squares method. The quantity $1/r$ is the parallactic factor, which is assumed to be equal to unity. In this case, the stars are referred to a unit sphere. In this approach, all of the parameters being determined are proportional to the heliocentric distance of the stellar centroid under consideration and are expressed in the same units as the stellar proper motion components, i.e., in mas yr^{-1}. Before the appearance of the Hipparcos catalog, researchers were forced to use this method of analysis because of the lack of highly accurate stellar parallaxes. When the distances to stars are known, the parallactic factor is $1/r = \pi/4.74$, where π is the parallax, and the factor 4.74 is equal to the ratio of the number of kilometers in an astronomical unit to the number of seconds in a tropical year. To express the solar velocity components (mas yr^{-1}) in km s^{-1}, they must be multiplied by $4.74/\pi$; to express any of the derived (in mas yr^{-1}) components of the deformation and rotation tensors in km s^{-1} kpc^{-1}, they must be multiplied only by the proportionality factor 4.74.

THE SYSTEM OF THE HIPPARCOS CATALOG

We divided the Hipparcos stars into seven groups, depending on the heliocentric distance (kpc): 0.05–0.1, 0.1–0.2, 0.2–0.3, 0.3–0.45, 0.45–0.66, >0.66, and the group of stars with negative parallaxes. We imposed a constraint on the stellar space velocity that allows us to discard only those stars whose space velocities exceed the hyperbolic velocity, for example, stars with enormous peculiar velocities acquired through explosions and encounters, $V = 220 + 62 = 282$ km s^{-1}. Here, 220 km s^{-1} is the circular velocity of Galactic rotation at the solar Galactocentric distance (recommended by IAU 1986) and

62 km s^{-1} is the mean stellar space velocity dispersion in the solar neighborhood (estimated by Oort). The Hipparcos stars whose space velocities exceed the hyperbolic velocity were found, for example, by Moffat *et al.* (1998). In this case, when using only the stellar proper motions, we estimated the stellar space velocities on the basis of the Kleiber theorem (Agekyan *et al.* 1962):

$$|V_t|4.74r < \frac{3.14}{4}|V|.$$

Here, $V_t = \sqrt{(\mu_l \cos b)^2 + \mu_b^2}$ is the tangential velocity of the star in mas yr^{-1}, and V is the total space velocity of the star in km s^{-1}.

Table 1 presents the results of the simultaneous solution of Eqs. (1) and (2). Columns 1–7 give the parameters obtained from the proper motions of the stars located in seven "thin" spherical shells. All of the stars with negative parallaxes were assumed to be located at a heliocentric distance of 2 kpc. The last column gives the kinematic parameters determined from the proper motions of 58 675 distant stars located farther than 0.2 kpc from the Sun (the mean heliocentric distance of this group of stars is 0.371 kpc). We emphasize that these are special solutions; they were obtained by setting the parallactic factor equal to $1/r = 1$. We needed the parallaxes to divide the stars into distance-limited groups. This method made it possible, first, to use the most distant Hipparcos stars with negative parallaxes, second, to completely eliminate all of the effects of random parallax errors when solving Eqs. (1) and (2), and, third, to ensure that the results obtained by this method are in close agreement with those obtained from the proper motions of TRC stars. Since we used this approach to control the inertiality of the Hipparcos catalog, the solution from the last column of Table 1 that is of greatest interest in this respect may be called inertial. Let us consider the derived kinematic parameters of the inertial solution (in mas yr^{-1}):

$$\begin{aligned} M_{12}^+ &= +2.90 \pm 0.09, \quad M_{21}^- = -2.93 \pm 0.07, \quad (3)\\ M_{13}^+ &= -0.11 \pm 0.11, \quad M_{13}^- = -0.36 \pm 0.09,\\ M_{23}^+ &= +0.13 \pm 0.10, \quad M_{32}^- = -0.16 \pm 0.08,\\ M_{11}^+ - M_{22}^+ &= -1.35 \pm 0.19,\\ M_{33}^+ - M_{22}^+ &= -0.14 \pm 0.21. \end{aligned}$$

As we can see, the following quantities are statistically significant: M_{12}^+, M_{21}^-, and $(M_{11}^+ - M_{22}^+)$. Based on these quantities, we find that $A = 13.7 \pm 0.4$ km s^{-1} kpc^{-1}, $B = -13.9 \pm 0.3$ km s^{-1} kpc^{-1}, $C = -3.2 \pm 0.5$ km s^{-1} kpc^{-1} and the vertex deviation $l_{xy} = 7^\circ \pm 1^\circ$. To this end, we used the standard relations $A = M_{12}^+ 4.74$, $B = M_{21}^- 4.74$, $C = 4.74(M_{11}^+ - M_{22}^+)/2$ and $\tan 2l_{xy} = -C/A$. The Oort constants A and B obtained by this method are in good agreement with the values recommended by the IAU (1986) and with the values from the paper by Bobylev (2004): $A = 13.7 \pm 0.6$ km s^{-1} kpc^{-1}, $B = -12.9 \pm 0.4$ km s^{-1} kpc^{-1} in which they were calculated by analyzing their recent determinations by various authors. The vertex deviation also agrees with its published determinations based on various observational data, for example, with those by Dehnen and Binney (1998).

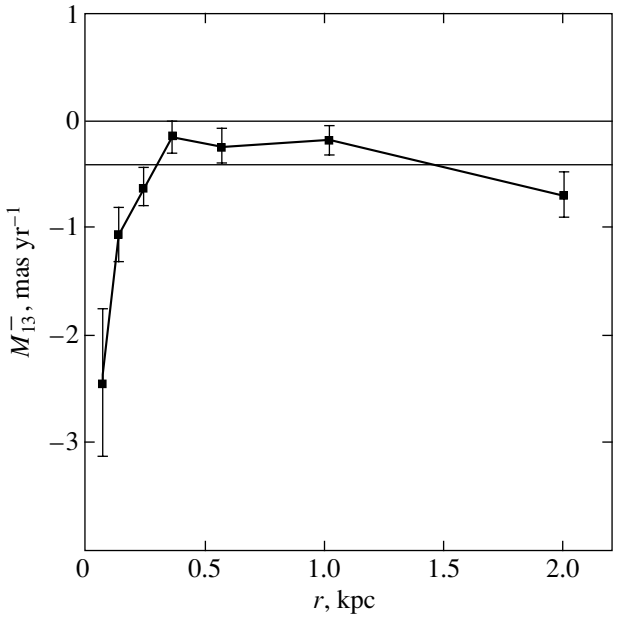

Fig. 1. Component M_{13}^- of the rigid-rotation tensor for Hipparcos stars against stellar heliocentric distance r.

Note, nevertheless, that M_{13}^- is also statistically significant. Figure 1 shows a plot of M_{13}^- against heliocentric distance constructed from the data of Table 1. As we can see from Table 1 and Fig. 1, M_{13}^- is nonzero for the most distant Hipparcos stars. It should also be emphasized that, as can be seen from Fig. 1, the constraint $r > 0.2$ kpc used to obtain the inertial solution and to determine M_{13}^- has such an effect that we obtain a lower limit on M_{13}^-.

THE SYSTEM OF THE TRC CATALOG

The results of our solution of Eqs. (1) and (2) based on TRC stars of mixed spectral composition are plotted against magnitude in Fig. 2. The random errors of all of the sought unknowns are small in all of the magnitude intervals, each of which contains ~100 000 stars, and are equal to 0.1–0.2 mas yr^{-1} for faint stars. As we can see from Fig. 2, the parameters that describe the deformation in the yz plane and the

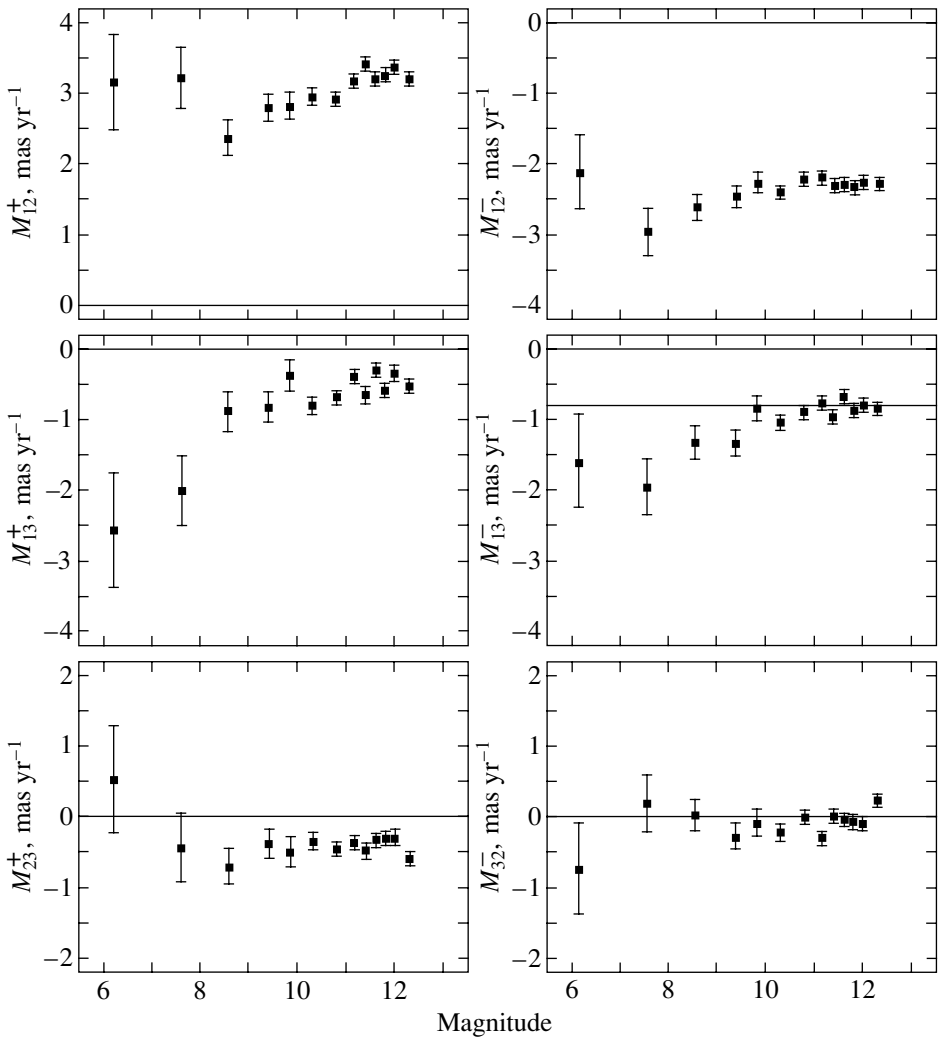

Fig. 2. Kinematic parameters inferred from the proper motions of TRC stars versus magnitude (Tycho B mag.).

rotation around the x axis, i.e., M_{23}^{+} and M_{32}^{-}, are virtually equal to zero. The parameters that describe the deformations in the xy and yz planes and the rotation around the z and y axes differ significantly from zero. The values of M_{13}^{-} are nonzero for the faintest TRC stars. We calculated the mean,

$$M_{13}^{-} = -0.86 \pm 0.11 \text{ mas yr}^{-1}, \qquad (4)$$

by using the results obtained in nine intervals of magnitudes fainter than $9\overset{\text{m}}{.}5$. This result must be compared with the results of our analysis of the proper motions for Hipparcos stars.

The deviation of the vertex l_{xy} is virtually equal to zero in each magnitude interval, which does not confirm the conclusions drawn from our analysis of the Hipparcos stellar proper motions. This result probably stems from the fact that to compile the reference catalog that the TRC was intended to be (Kuzmin *et al.* 1999), the stars were selected kinematically; no high proper-motion stars were used.

We calculated the mean values of $M_{21}^{+} = 3.15 \pm 0.20$ mas yr^{-1} and $M_{12}^{-} = -2.27 \pm 0.06$ mas yr^{-1} by the mean of the nine values obtained in the intervals of magnitudes fainter than $9\overset{\text{m}}{.}5$ (the mean being $m = 11\overset{\text{m}}{.}2$). This yields the following Oort constants: $A = 14.93 \pm 0.97$ km s^{-1} kpc^{-1} and $B = -10.77 \pm 0.31$ km s^{-1} kpc^{-1}, which are in good agreement with those calculated by Olling and Dehnen (1999) from the Tycho/ACT proper motions of red giants: $A = 14.2 \pm 1$ km s^{-1} kpc^{-1} and $B = -12.7 \pm 1$ km s^{-1} kpc^{-1}.

The model component that describes the rotation about the Galactic y axis inferred here from a kinematic analysis of the proper motions of TRC stars is $M_y = -0.86 \pm 0.11$ mas yr^{-1} and confirms the rotation that we found from the Hipparcos catalog (solution (3)). In this case, we have an upper limit, since the data for the faintest stars include the effect

Table 2. Precession corrections Δp_1 and ΔE, mas yr^{-1}

Reference	Data	Δp_1	ΔE
Miyamoto and Sôma (1993)	ACRS	$-2.7_{(0.3)}$	–
Walter and Ma (1994)	VLBI	$-3.6_{(1.1)}$	–
Charlot *et al.* (1995)	VLBI+LLR	$-3.0_{(0.2)}$	–
Rybka (1995)	PPM	$-3.1_{(0.2)}$	$-1.3_{(0.2)}$
Bobylev (1997)	PUL2–PPM	$-2.8_{(0.8)}$	–
Ma *et al.* (1998)	VLBI	$-2.84_{(0.04)}$	–
Vityazev (1999)	CGC–HIP	$-3.4_{(1.0)}$	$-3.3_{(1.0)}$

of the real rotation of nearby stars that to the Local stellar system (Fig. 1).

CORRECTION TO THE IAU (1976) PRECESSION CONSTANT

The proper motions of the Hipparcos stars are free from the effect of precession of the Earth's axis. However, the Hipparcos catalog is an extension to the optical range of the ICRF system (Ma *et al.* 1998), which is based on ground-based VLBI observations of radio sources.

To determine the precession parameters from the analysis of M_y, we use two equations that, given the numerical values for epoch J2000.0 (Perryman *et al.* 1997), can be written as

$$M_x = \Omega_x - 0.0965\Delta p_1 + 0.4838\Delta E, \quad (5)$$

$$M_y = \Omega_y + 0.8623\Delta p_1 - 0.7470\Delta E. \quad (6)$$

Here, Ω_x and Ω_y are the vector components of the real rigid rotation of the stellar system, and this rotation actually exists at heliocentric distances up to $r \sim 0.2$ kpc. Assuming that at large distances, $M_x - \Omega_x = 0$ and $M_y - \Omega_y = -0.36 \pm 0.09$ mas yr^{-1} includes only the precession quantities, we obtain from the solution of Eqs. (5) and (6)

$$\Delta p_1 = -0.50 \pm 0.13 \text{ mas yr}^{-1}, \quad (7)$$

$$\Delta E = -0.10 \pm 0.02 \text{ mas yr}^{-1}. \quad (8)$$

Setting $\Delta E = 0$, we obtain the following estimate from Eq. (6):

$$\Delta p_1 = -0.42 \pm 0.10 \text{ mas yr}^{-1}. \quad (9)$$

Table 2 gives the results of the determinations of two precession parameters by various authors: the correction to the IAU (1976) constant of lunisolar precession in longitude, Δp_1, and ΔE, which is the sum of the corrections to the rate of planetary precession and the motion of the zero point of right ascensions. Miyamoto and Sôma (1994) determined the precession correction based on a kinematic analysis of the proper motions of ACRS stars using the Ogorodnikov–Milne kinematic model. Walter and Ma (1994) determined the precession correction based on VLBI observations of extragalactic radio sources from an annual catalog. Charlot *et al.* (1995) determined the precession correction by analyzing a 24-yr-long series of lunar laser radar observations and a 16-yr-long series of radio-interferometric observations. Rybka (1995) determined the precession parameters based on a kinematic analysis of the proper motions of PPM stars using the Ogorodnikov–Milne kinematic model. Bobylev (1997) determined the precession correction by analyzing the differences between the Pulkovo absolute proper motions and PPM. To obtain the ICRF system that is based on ground-based VLBI observations of radio sources, Ma *et al.* (1998) adopted the following correction to the IAU (1976) lunisolar precession constant: $\Delta p_1 = -2.84 \pm 0.04$ mas yr^{-1}. Vityazev (1999) determined the precession parameters by comparing the proper motions of CGC and Hipparcos stars.

Our kinematic analysis of the proper motions of Hipparcos stars yielded $\Delta p_1 = -0.42 \pm 0.10$ mas yr^{-1} (solution (9)). It may be assumed that Ma *et al.* (1998) slightly underestimated Δp_1. Since the ICRS was constructed using precisely this value, we obtain a statistically significant "addition" to this correction, Δp_1, when analyzing the Hipparcos and TRC catalogs. Therefore, the correction to the IAU (1976) lunisolar precession constant is

$$\Delta p_1 = -3.26 \pm 0.10 \text{ mas yr}^{-1}. \quad (10)$$

This value agrees well with the data given in Table 2.

THE MOTION OF DISTANT OB STARS

Results (7)–(9) have yet another important implication: they show that $M_y = -0.36 \pm 0.09$ mas yr^{-1}

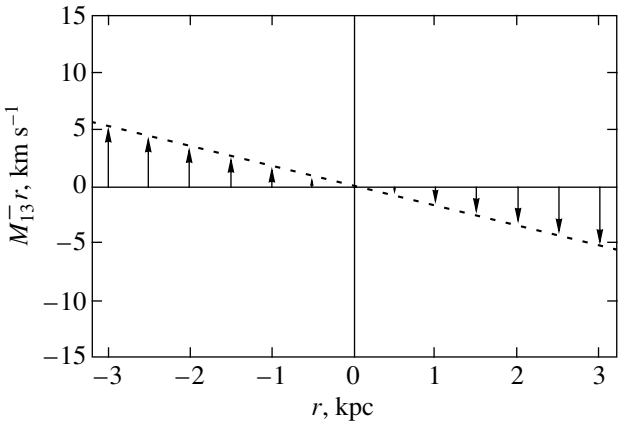

Fig. 3. Linear velocity vectors $M_{13}^- r \equiv W$ versus heliocentric distance r. The Galactic plane coincides with the xz plane, the x axis coincides with the r direction, and the z axis is directed upward.

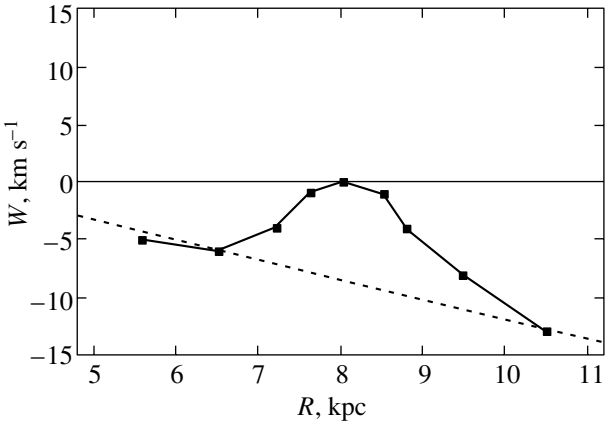

Fig. 4. Stellar residual velocity components W versus heliocentric distance R. The solar motion with respect to the LSR with velocities $(U, V, W)_\odot = (9, 5, 7)$ km s^{-1} was taken into account. The dotted line indicates our dependence, which must be eliminated.

may have a nature unrelated to the real stellar motions. The H I layer in the Galaxy is known to have an extended warp (Kulikovskiĭ 1985; Carroll and Ostly 1996). Smart *et al.* (1997) and Drimmel *et al.* (2000) considered the hypothesis that the extended Galactic H I layer affects the kinematics of OB stars. Drimmel *et al.* (2000) used simulations to estimate the angular velocity of the precession of OB stars in the zx-plane, -25 km s^{-1} kpc^{-1}. The effect of our $M_{13}^- = -0.36$ mas yr^{-1} (solution (3)) on the kinematic parameters of stars is easy to calculate. Since $M_{13}^- \times 4.74 = -1.7$ km s^{-1} kpc^{-1}, it is equal to -1.7 and -3.4 km s^{-1} at $r = 1$ and 2 kpc, respectively. The presence of such a fictitious wave could completely explain the precession velocity of -25 km s^{-1} kpc^{-1} found by Drimmel *et al.* (2000) for distant OB stars. In Fig. 3, the linear rotation velocity vectors $M_{13}^- r$ are plotted against heliocentric distance r. This rotation is attributable to the $M_{13}^- = -0.36$ mas yr^{-1} that we inferred from the Hipparcos catalog. The directions of the vectors are indicated in accordance with the fact that the rotation takes place in the zx plane and that, according to the chosen coordinate system, the rotation from the z axis to the x-axis is positive. In Fig. 4, the W components of space velocity (the linear velocity along the z-coordinate) are plotted against heliocentric distance R. The points are plotted by using the data obtained by Drimmel *et al.* (2000) for a sample of 4250 Hipparcos OB stars in the magnitude interval 0–$13^{\rm m}$. A comparison of Fig. 3 (the Sun is assumed to be at a Galactocentric distance of about $R_0 = 8.0$ kpc) and Fig. 4 leads us to conclude that the value of $M_{13}^- = -0.36$ mas yr^{-1} that we inferred from Hipparcos data almost completely explains the slope of the plot in Fig. 4. Eliminating the dependence that we found should significantly reduce the precession of -25 km s^{-1} kpc^{-1} for distant OB stars derived by Drimmel *et al.* (2000). In this case, the fact that distant OB stars belong to the hydrogen layer implies that there is only a linear displacement of all distant OB stars along the z coordinate.

CONCLUSIONS

Based on a linear Ogorodnikov–Milne model, we have performed a kinematic analysis of the Hipparcos and TRC stellar proper motions. We found the rotation of all distant ($r > 0.2$ kpc) Hipparcos stars with a mean angular velocity of $M_{13}^- = -0.36 \pm 0.09$ mas yr^{-1} about the Galactic y axis. One of the causes of this rotation may be an inaccuracy of the lunisolar precession constant adopted when creating the ICRF (Ma *et al.* 1998). We showed that, in this case, the correction to the IAU (1976) constant of lunisolar precession in longitude is $\Delta p_1 = -3.26 \pm 0.10$ mas yr^{-1}.

We have shown that eliminating the rotation $M_{13}^- = -0.36 \pm 0.09$ mas yr^{-1} from the proper motions of distant OB stars should lead to a significant reduction in the -25 km s^{-1} kpc^{-1} precession of distant OB stars inferred by Drimmel *et al.* (2000). In this case, the fact that distant OB stars belong to the hydrogen layer reduces only to a linear displacement of all distant OB stars along the z coordinate.

We have determined the mean Oort constants $A = 14.9 \pm 1.0$ km s^{-1} kpc^{-1} and $B = -10.8 \pm 0.3$ km s^{-1} kpc^{-1} from TRC data. The model component that describes the rotation of all TRC stars about the Galactic y axis was found to be nonzero for all magnitudes, $M_{13}^- = -0.86 \pm 0.11$ mas yr^{-1}.

ACKNOWLEDGMENTS

This work was supported by the Russian Foundation for Basic Research (project no. 02-02-16570).

REFERENCES

1. T. A. Agekyan, B. A. Vorontsov-Vel'yaminov, V. G. Gorbatskiĭ, *et al., A Course on Astrophysics and Stellar Astronomy,* Ed. by A. A. Mikhaĭlov (Fizmatlit, Moscow, 1962), Vol. 2 [in Russian].
2. V. V. Bobylev, *JORNEES 1997,* Ed. by J. Vondrák and N. Capitaine (Obs. de Paris, Paris, 1997), p. 91.
3. V. V. Bobylev, Pis'ma Astron. Zh. **30**, 185 (2004).
4. B. W. Carroll and D. A. Ostly, *An Introduction to Modern Astrophysics* (Addison-Wesley, New York, 1996).
5. P. Charlot, O. J. Sovers, J. G. Williams, *et al.*, Astron. J. **109**, 418 (1995).
6. S. V. M. Clube, Mon. Not. R. Astron. Soc. **159**, 289 (1972).
7. S. V. M. Clube, Mon. Not. R. Astron. Soc. **161**, 445 (1973).
8. W. Dehnen and J. J. Binney, Mon. Not. R. Astron. Soc. **298**, 387 (1998).
9. R. Drimmel, R. L. Smart, and M. G. Lattanzi, Astron. Astrophys. **354**, 67 (2000).
10. E. Hfig, A. Kuzmin, U. Bastian, *et al.*, Astron. Astrophys. **333**, L65 (1998).
11. A. Kuzmin, E. Hfig, U. Bastian, *et al.*, Astron. Astrophys., Suppl. Ser. **136**, 491 (1999).
12. P. G. Kulikovskiĭ, *Stellar Astronomy* (Nauka, Moscow, 1985) [in Russian].
13. C. Ma, E. F. Arias, T. M. Eubanks, *et al.*, Astron. J. **116**, 516 (1998).
14. M. Miyamoto and M. Sôma, Astron. J. **105**, 691 (1993).
15. B. du Mont, Astron. Astrophys. **61**, 127 (1977).
16. B. du Mont, Astron. Astrophys. **66**, 441 (1978).
17. A. F. G. Moffat, S. V. Marchenko, W. Seggewiss, *et al.*, Astron. Astrophys. **331**, 949 (1998).
18. K. F. Ogorodnikov, *Dynamics of Stellar Systems* (Fizmatgiz, Moscow, 1965).
19. R. P. Olling and W. Dehnen, Bull. Am. Astron. Soc. **31**, 1379 (1999).
20. M. A.C. Perriman, L. Lindegren, J. Kovalevsky, *et al.*, Eur. Space Agency **1–17** (1997).
21. S. P. Rybka, Kinemat. Fiz. Neb. Tel **11**, 77 (1995).
22. R. L. Smart, R. Drimmel, M. G. Lattanzi, *et al.*, *JORNEES 1997,* Ed. by J. Vondrák and N. Capitaine (Obs. de Paris, Paris, 1997), p. 179.
23. *The HIPPARCOS and Tycho Catalogues,* ESA SP-1200 (1997).
24. V. V. Vityazev, Doctoral Dissertation in Mathematical Physics (St. Petersburg, 1999).
25. H. G. Walter and C. Ma, Astron. Astrophys. **284**, 1000 (1994).

Translated by A. Dambis

Astronomy Letters, Vol. 30, No. 4, 2004, pp. 258–267. Translated from Pis'ma v Astronomicheskiĭ Zhurnal, Vol. 30, No. 4, 2004, pp. 297–306.

Spectral and Photometric Evolution of the Symbiotic Nova HM Sagittae in 1986–2002

V. P. Arkhipova*, V. F. Esipov, N. P. Ikonnikova, and R. I. Noskova

Sternberg Astronomical Institute, Universitetskiĭ pr. 13, Moscow, 119992 Russia

Received August 11, 2003

Abstract—We present the results of our photometric and spectroscopic observations of the symbiotic nova HM Sge in 1994–2002. After its outburst in 1975, the star was shown to fade in the U, B, V bands at a rate of about $0^m.05$ per year. The behavior of the $B-V$ and $U-B$ color indices reflects the variations of emission lines and, in part, the fading of the erupted component. We have studied the evolution of the emission spectrum in the range from Hδ to λ7751 Å over the period 1986–2002. The absolute fluxes in the hydrogen lines decreased by half, the ionization of the gaseous envelope continued to increase, and the Raman O VI lines appeared and strengthened. The significant (threefold) decrease in the ratio of the auroral and nebular O III lines is interpreted as a drop in the electron temperature of the envelope as its density decreased by a factor of about 1.5. We have measured the absolute intensity of the near-infrared continuum up to 10 000 Å and show that the infrared continuum follows the pulsations of the Mira star in the system HM Sge. We conclude that the dust envelope around the cool component became noticeably transparent in the 1990s.

Key words: *stars—variable and peculiar, symbiotic novae, photometry, spectra, HM Sge.*

INTRODUCTION

The symbiotic nova HM Sge, whose outburst occurred in 1975 (Dokuchaeva 1976), is still the object of intensive study in different spectral ranges. The system consists of a blue subdwarf and a Mira star surrounded by its own dense dust envelope. The Mira star is optically invisible because of high extinction, and its pulsations show up clearly only in the infrared. The period of the brightness variations in the red component is about 540 days. Following the outburst of the hot component, the system contains ionized gas whose excitation is increasing with time, as suggested by the emergence of emission lines of increasingly high ionization stages in the stellar spectrum. Soft X-ray radiation from the system and continuum radio emission from the gaseous nebula have also observed.

In contrast to classical novae, symbiotic novae exhibit a much lower optical luminosity at the maximum of their outburst and a very slow brightness decline after it. The parameter t_3 (the time of brightness decline from the maximum by 3^m) for the slowest classical novae does not exceed 1000 days. The symbiotic novae fade much more slowly, because, in particular, their envelope expansion velocities differ by an order of magnitude. Their post-outburst spectral evolution is greatly extended in time compared to the spectral evolution of typical novae.

We have been systematically observing HM Sagittae, one of the ten known representatives of the class of symbiotic novae, since its discovery. The first photoelectric observations after its discovery and pre-outburst photographic data were published previously (Belyakina *et al.* 1988). A spectrum taken immediately after its discovery was analyzed by Arkhipova *et al.* (1979). Subsequent spectroscopic and photometric observations were published by Arkhipova and Noskova (1991) and Arkhipova *et al.* (1994). Noskova (1996) determined the star's radial velocities from its emission lines.

In this paper, we present the results of our photometric and spectroscopic observations of the star for the period 1994–2002. Our goal was to study the evolution of the hot star and the envelope over almost 20 years, based on the absolute and relative intensities of the spectral lines and the continuum in the wavelength range 4100–10 000 Å. We show that the hot component faded by a factor of two near 5000 Å over this period. We also study the variations in envelope parameters: the density and the electron temperature. The contribution of the cool component to the combined near-IR spectrum was found to be considerable in the 1990s, suggesting that its dust envelope had become more transparent.

*E-mail: vera@sai.msu.ru

1063-7737/04/3004-0258$26.00 © 2004 MAIK "Nauka/Interperiodica"

UBV OBSERVATIONS OF HM Sge

Our *UBV* observations of HM Sge before 1993 were published previously (Arkhipova *et al.* 1994). We continued our observations with the same 60-cm reflector at the Crimean Station of the Sternberg Astronomical Institute (SAI) using the same instrumentation and the same photometric system, which is of great importance for a star with strong emission lines in its spectrum. Since 1995, the observations have been carried out with two apertures, 27″ and 13″ in diameter, while our earlier observations were mainly performed with a 27″ aperture that included the star's faint companion 8″ north of HM Sge. As previously, the comparison star was BD+16°3965, an F5 star (denoted by "g" in Arkhipova *et al.* 1994).

The CCD observations performed in 1999 and 2002 improved the *UBV* magnitudes of the companion: $V = 13\overset{m}{.}6$, $B = 14\overset{m}{.}2$, and $U = 14\overset{m}{.}5$.

Since HM Sge has faded with time, the contribution of the companion to the total light in 2002 reached $\sim 0\overset{m}{.}3$ in V, $\sim 0\overset{m}{.}3$ in B, and $\sim 0\overset{m}{.}1$ in U. Therefore, we corrected all our observations with the 27″ aperture for the contribution of the companion. Table 1[1] gives our *UBV* observations of HM Sge from 1994 to 2002, corrected for the contribution of the neighboring star.

We also computed the yearly mean *UBV* magnitudes for HM Sge obtained before 1994 and corrected for the influence of the companion. As a result, we compiled a homogeneous catalog of *UBV* data for HM Sge over the entire period of its observations from 1976 to 2002 (Table 2).

The yearly mean V, B, and U magnitudes for this period are shown in Fig. 1. After 1981, the rate of brightness decline in the star in the V and B bands was about $0\overset{m}{.}05$ per year. The $B-V$ color index (Fig. 2) increased by 0.2 from 1981 until 1997 and then began to monotonically decrease. The $U-B$ color index (Fig. 2) decreased to -1.0 by 1989, with the largest changes being observed in 1982–1983. After 1989, it began to gradually increase. As was show previously (Arkhipova and Noskova 1991), the star's color properties in the U, B, V bands characterize the hot component together with the gaseous nebula. The influence of the nebula's Balmer emission continuum is significant in the U band, while the contribution of its emission lines is large in the V and B bands (according to our estimates, it exceeds 70% in B).

[1]Tables 1 and 6 are published in electronic form only and are accessible via ftp cdsarc.u-strasbg.fr/pub/cats/J (130.79.128.5) or http://cdsweb.u-strasbg.fr/pub/cats/J.

Table 2. Yearly mean *UBV* data for HM Sge in 1976–2002

JD 2400000+	V	B	U	$B-V$	$U-B$	$U-V$
43052	11.91	12.32	11.92	0.41	−0.40	+0.01
43355	11.18	11.48	11.01	0.30	−0.47	−0.17
43675	11.19	11.63	11.14	0.44	−0.49	−0.05
44098	11.08	11.42	11.12	0.34	−0.30	+0.04
44479	11.19	11.60	11.25	0.41	−0.35	+0.06
44878	11.12	11.43	11.16	0.31	−0.27	+0.04
45173	11.10	11.43	11.15	0.33	−0.28	+0.05
45613	11.28	11.70	10.92	0.42	−0.78	−0.36
45911	11.25	11.66	10.89	0.41	−0.77	−0.36
46279	11.36	11.82	10.90	0.46	−0.92	−0.46
46638	11.41	11.82	10.90	0.41	−0.92	−0.51
47004	11.41	11.89	10.95	0.48	−0.94	−0.46
47375	11.54	11.98	11.02	0.44	−0.96	−0.52
47744	11.55	12.00	11.00	0.45	−1.00	−0.55
48121	11.61	12.10	11.16	0.49	−0.94	−0.45
48465	11.65	12.14	11.25	0.49	−0.89	−0.40
48861	11.66	12.18	11.29	0.52	−0.89	−0.37
49175	11.68	12.18	11.32	0.50	−0.86	−0.36
49540	11.73	12.24	11.48	0.49	−0.84	−0.35
49933	11.77	12.26	11.44	0.49	−0.82	−0.33
50250	11.90	12.41	11.54	0.49	−0.87	−0.38
50620	11.86	12.39	11.56	0.53	−0.83	−0.40
51043	11.90	12.38	11.57	0.48	−0.81	−0.33
51410	11.97	12.39	11.59	0.42	−0.80	−0.38
51772	12.05	12.43	11.66	0.38	−0.77	−0.39
52101	12.15	12.50	11.71	0.35	−0.79	−0.44
52464	12.08	12.52	11.74	0.44	−0.78	−0.34

In the two-color ($U-B$, $B-V$) diagram (Fig. 3), the star moved upward to the right and back, similar to the behavior of another symbiotic nova, V1016 Cyg (Parimucha *et al.* 2000). Such a motion can be attributed to variations in the emission Balmer jump of the nebular continuum due to variations in the electron temperature of the gaseous envelope, as well as to the appearance and changes of emission lines, particularly the strongest [NeV] 3343, 3425 Å doublet in the U band.

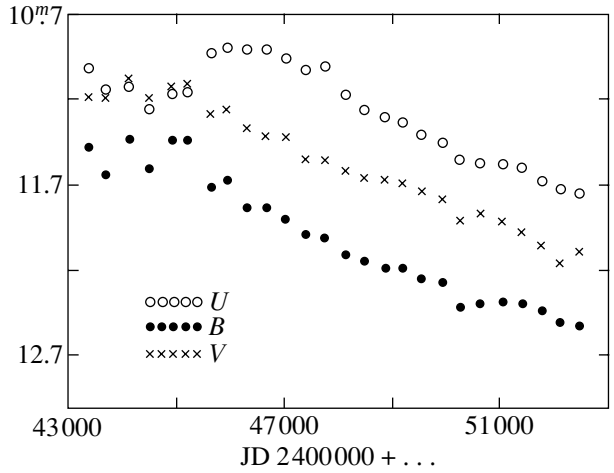

Fig. 1. Yearly mean UBV magnitudes of HM Sge for 1976–2002.

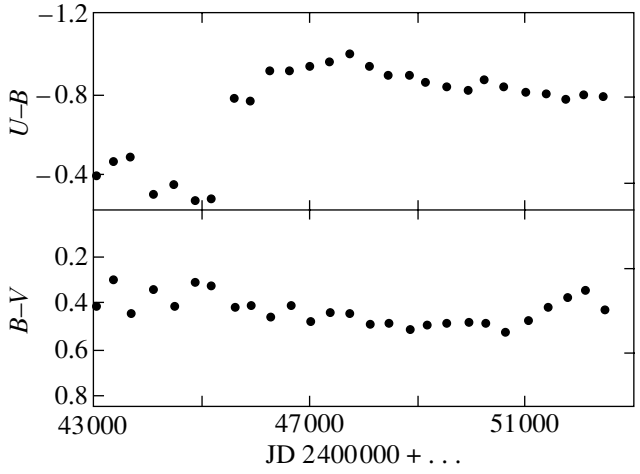

Fig. 2. The evolution of the $B-V$ and $U-B$ color indices in 1976–2002.

After the outburst, the star described something of an arc in the color–magnitude $(U-B, U)$ diagram (Fig. 4), which can also be interpreted as the result of variations in the electron temperature and emission measure of the gaseous envelope.

SPECTROSCOPIC OBSERVATIONS OF HM Sge

Observational data. We carried out the spectroscopic observations of HM Sge in the period 1994–2002 with the 125-cm reflector at the Crimean Station of the SAI using a fast spectrograph equipped with an ST-6 I CCD camera in the range $\lambda\lambda$4000–10 000 Å with a resolution of about 5 Å per pixel.

We used stars with known spectral energy distributions as standards for the absolute calibration of the continuum and emission-line fluxes. Information about our spectra and the comparison stars is contained in Tables 3 and 4.

The continuum of HM Sge. The continuum of HM Sge observed in 1987–1988 in the range $\lambda\lambda$4500–6500 Å was virtually flat, and the monochromatic flux was, on average, $F_{\rm cont} = (2.8 \pm 0.3) \times 10^{-14}$ erg cm^{-2} s^{-1}Å^{-1} (Arkhipova and Noskova 1991). It was the sum of the radiation from the erupted hot component and the continuum of the gaseous envelope.

We present our continuum measurements for HM Sge over the observing period 1994–2002 in Table 5. The accuracy of the estimated continuum intensities is different for different parts of the spectrum; it varies within the range 10–40%, with the error increasing with wavelength.

The continuum flux in the range λ4200–5000 Å was essentially constant, $F_{\rm cont} = (1.3–1.5) \times 10^{-14}$ erg cm^{-2} s^{-1}Å^{-1}, over the entire observing period 1994–2002; this was a factor of 2 lower than the flux observed ten years ago. However, the continuum intensity in the red spectral range was variable and significantly increased with wavelength, which can be interpreted as a manifestation of the cool component's continuum. The continuum of the red component was particularly strong in 1996–1999: the nebular emission lines at $\lambda > 7000$ Å range were lost in the absorption bands of the Mira star. Near $\lambda \sim 1\ \mu$m, the continuum intensity of HM Sge during this period was a factor of 5 to 10 higher than the continuum intensity in other years.

Table 5 gives the pulsations phases ϕ for the Mira star computed with the $540^{\rm d}$ period from Whitelock (1988). The monochromatic continuum fluxes at wavelengths $\geq$6400 Å follow this period; the amplitude of the light curves increases considerably with wavelength, which confirms that the near-IR continuum largely belongs to the cool component of the binary. Figure 5 illustrates the phase curve with the pulsation period of the color index $\mathrm{CI} = -2.5\log(I(8200)/I(9200))$ computed by using the data from Table 5.

Note that Rudy *et al.* (1999) presented the continuum fluxes near $\lambda \sim 1\ \mu$m estimated from the spectroscopic observations in the range $\lambda\lambda$0.9–1.3 μm performed with the 3-m Lick Observatory telescope:

$$\text{July 6, 1988,} \quad \text{JD 47349,}$$
$$F_{\rm cont} = 5 \times 10^{-14}\ \text{erg cm}^{-2}\ \text{s}^{-1}\ \text{Å}^{-1}, \quad \phi = 0.91,$$
$$\text{July 13, 1989,} \quad \text{JD 47721,}$$
$$F_{\rm cont} = 22 \times 10^{-14}\ \text{erg cm}^{-2}\ \text{s}^{-1}\ \text{Å}^{-1}, \quad \phi = 0.60.$$

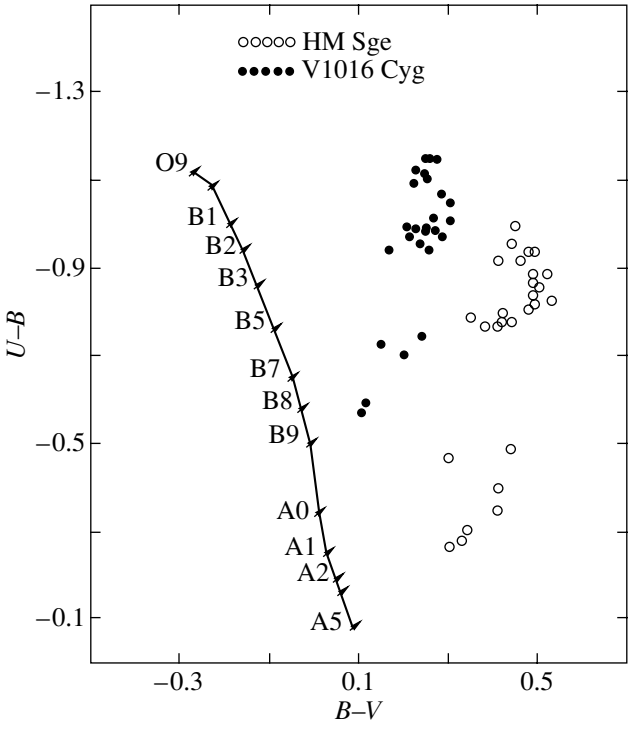

Fig. 3. Tracks of HM Sge and V1016 Cyg in the two-color ($U-B$, $B-V$) diagram.

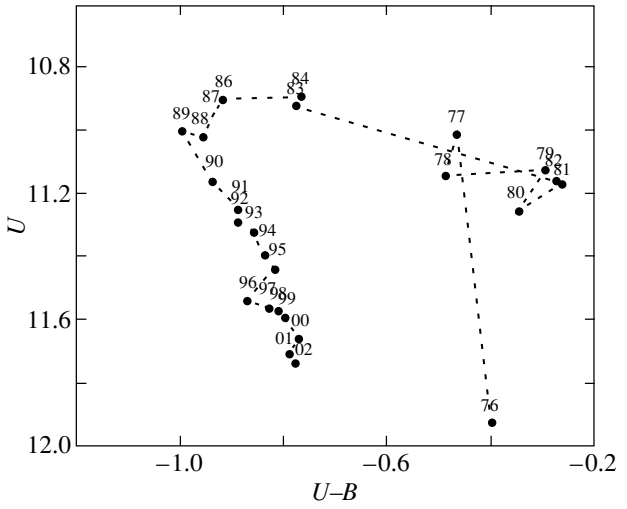

Fig. 4. Relation between the U magnitude and the $U-B$ color.

These estimates are close to our results of the period 1993–1995 obtained at approximately the same phases. Rudy *et al.* (1999) estimated the spectral type of the cool component in the system HM Sge from the VO band near 1.05 μm as M5–M7. At phases close to maximum light, our spectra clearly show the TiO λ7100, 7590, 8430, 8860 Å, ZrO λ8194, 8210, 9300–9330 Å, CaH λ6700 Å absorption bands. At shorter wavelengths, the absorption bands of the cool component do not show up because of the significant contribution from the nebular continuum and the hot component to the combined continuum in this range.

Note that, in addition to the continuum variations with the pulsation period of the Mira star, deep IR continuum intensity minima separated by an interval of ~2300 days (6.3 yr) were observed in 1995 and 2001. Munari (1988) found a similar period for V1016 Cyg and interpreted it as the result of variable obscuration of the cool companion by dust during its orbital motion. Backward extrapolation with a 2300-day period yields two epochs, 1976 and 1982, when the IR observations of HM Sge revealed dust density maxima or M-band brightness maxima (Taranova and Shenavrin 2000). This may stem from the orbital motion of the components, but further observations are needed.

In general, it should be noted that the Mira's near-IR continuum was clearly seen over the past decade, which may be indicative of the overall decrease in the optical depth of the dust envelope in the 1990s compared to the late 1970s.

Changes of emission lines in the spectrum of HM Sge after 1985. Our CCD spectroscopic observations in 1994–2002 were performed mainly in four spectral ranges covering the interval λ4000–10 000 Å. The enhanced contribution of the Mira star, especially at $\lambda > 7000$ Å, makes it impossible to reliably measure the emission-line fluxes over the entire range under study. Table 6 contains the observed absolute emission-line fluxes over the spectral range $\lambda\lambda$4100–7751 Å. The accuracy of measuring the fluxes in lines strongly depends on their intensities, the spectral range, and other factors, and is within 10–30%.

We compared the absolute fluxes in several lines with those observed in 1987–1988 (Arkhipova and Noskova 1991; Schmid and Schild 1990) and given in the last column of Table 6.

Over this period, the Hβ flux decreased by a factor of 1.5 to 2, being, on average, $F\beta = (12.5 \pm 2.5) \times 10^{-12}$ erg cm^{-2} s^{-1}. The Hα flux also decreased by almost a factor of 2.

The absolute flux in the [O III] λ4363 Å line systematically decreased over the period of our observations; in 2002, it was a factor of three lower than that in 1987–1988. Over this period, the Hγ flux decreased by a factor of 1.5. Thus, the intensity ratio of the λ4363 and λ4340 Å lines decreased by a factor of 2. Published data on the ratio of the fluxes in the Hγ and λ4363 Å lines for the period 1976–2002 are presented in Table 7. Its first two columns give the dates at which the spectra were taken and the corresponding Julian dates JD; the third column lists

Table 3. CCD spectroscopic observations of HM Sge

Date	JD 2400000+	n	Spectral range, Å	Standards
May 8, 1994	49481	3	4000–9400	50 Boo
June 15, 1994	49519	4	4000–10000	50 Boo
September 5, 1994	49601	3	4000–10000	50 Boo, HD 353437
July 16, 1995	49915	5	4000–10000	BS 5867
September 25, 1995	49986	4	4000–10000	BS 5867
October 9, 1996	50366	4	4000–10000	50 Boo
August 19, 1998	51045	4	4000–10000	50 Boo, HD 353437
August 8, 1999	51399	4	4000–10000	50 Boo
July 29, 2000	51755	4	4000–10000	50 Boo
June 25, 2001	52086	2	4000–7800	50 Boo, HD 353437
August 23, 2001	52145	4	4000–10000	HD 353437
October 13, 2001	52196	4	4000–10000	HD 353437
May 12, 2002	52407	9	4000–9500	HD 353437
September 3, 2002	52521	5	4000–9500	HD 353437

Table 4. Data for the standard stars

Standard	V	$B-V$	$U-B$	Spectral type	Reference
BS 5718=50 Boo =HD 136849	5.37	−0.06	–	B9V	Voloshina *et al.* 1982
BS 5867 =HD 141003	3.67	+0.06	–	A2IV	Voloshina *et al.* 1982
HD 353437="a"* =BD+16°3972	9.47	+0.24	−0.16	B2V	Arkhipova and Noskova 1991

* In our previous paper (Arkhipova and Noskova 1991), standard "a" was erroneously designated as HD 186295. In fact, HD 186295=BD+2°3972 bears no relation to standard "a."

the line intensity ratios. Figure 6 shows how this ratio has varied since the beginning of our observations of HM Sge from 1976 to 2002 inclusive.

Note the large decrease of the fluxes in the He I lines: λ5876 Å (a factor of 2 to 3), λ6678 Å (a factor of 2 to 4), and λ7065 Å (a factor of 6 to 10). In the latter case, the significant decrease in flux may be due to the growth of the contribution of the continuum that increases with wavelength and the significant errors of its subtraction.

The absolute fluxes in the He II λ4686 and λ5412 Å lines decreased, on average, by 20% compared to those in 1987–1988, although their ratios to Hβ increased by approximately 20%.

The fluxes in the [Fe VII] λ5721 and λ6086 Å lines decreased by almost a factor of 2 compared to those in 1987–1988. The blend of λ4942 Å with the [Ca VII] line grew by a factor of 1.7, probably because [Ca VII] strengthened. However, the estimate of the flux in the

Table 5. Observed continuum fluxes from HM Sge, $F_c \times 10^{14}$ erg cm^{-2} s^{-1}Å^{-1}

JD 24400000+	ϕ	λ, Å											
		4200	4600	5100	5800	6100	6600	7000	7400	8200	8800	9200	10000
49481	0.86	1.5	1.5	1.7	1.8	1.9	2.1	2.2	2.2	2.5	3.0	–	–
49519	0.93	1.5	1.5	1.8	2.1	2.2	2.3	2.4	2.8	3.6	4.0	6.6	8.8
49601	0.08	1.5	1.6	1.7	1.8	–	–	–	2.1	2.6	2.7	2.9	4.0
49915	0.66	1.5	1.5	1.6	1.9	2.0	2.1	2.3	2.6	4.4	5.9	9.9	18
49986	0.80	1.4	1.4	1.5	1.7	1.7	1.8	1.9	2.0	3.3	3.6	6.5	8.6
50366	0.50	1.4	1.4	1.4	1.8	2.1	2.6	3.8	5.5	10	14	30	50
51045	0.76	1.4	1.4	1.5	1.7	1.9	2.6	3.0	3.5	12.4	20	30	45
51399	0.41	1.4	1.6	1.9	2.4	2.5	3.0	6.1	8.4	20	30	53	75
51755	0.07	1.4	1.6	1.9	2.3	2.3	2.3	2.5	2.7	3.9	3.9	5.0	7.6
52086	0.69	1.4	1.5	1.6	1.7	1.8	2.0	2.6	–	–	–	–	–
52145	0.79	1.4	1.4	1.4	1.6	1.6	1.8	1.8	2.2	4.2	6.7	9.4	15
52196	0.89	1.4	1.4	1.4	1.6	1.6	1.7	1.7	1.8	2.8	3.2	5.7	8.7
52407	0.28	1.4	1.4	1.5	1.6	1.6	1.7	1.7	3.1	11	14	23	–
52521	0.49	1.4	1.4	1.5	1.6	1.6	1.7	1.9	2.5	6.4	8.2	16	–

λ4942 Å line is rather unreliable, since this line lies in the wing of the strong [O III] λ4959 Å line.

Pacheco *et al.* (1989) and Schmid and Schild (1990) provided the intensities for the [Fe VI] λ5631 line but not for the neighboring [Ca VII] λ5616 Å line (the observations of 1987–1988). In our spectra, the λ5616 Å line is a factor of 2 to 3 stronger than the λ5631 Å line. In the echelle spectrum taken in 1992 at the Special Astrophysical Observatory (SAO; Klochkova, private communication, 1993), the [Ca VII] line was also much stronger than the [Fe VI] line. The λ5616 Å line may still have been invisible in 1987–1988.

The fluxes in the λ6300 [O I] and λ6312 [S III] lines were equal in 1985–1987 (Pacheco *et al.* 1989; Schmid and Schild 1990). At present, the λ6300 line is a factor of 1.5 to 2 more intense than the λ6312 line. In general, however, the λ6300 flux (and the λ6363 [O I] flux) decreased by a factor of 1.5 to 2, while the flux in the [S III] line decreased by a factor of 2 to 4.

The sharp strengthening of the Raman O VI λ6825 Å line after 1996, characteristic of the spectra of symbiotic stars, is noteworthy. In our spectra, this line had an intensity <0.4% and 2–3% of the Hβ intensity before 1996 and after 1998, respectively; i.e., its flux increased by a factor of 5 to 10. However, the λ6825 Å emission was also seen in the SAO echelle spectrum in 1992. Another Raman line, λ7082, falls within the wing of the intense He I λ7065 emission line, and its flux can be estimated as being less than 1% of the Hβ flux only in two or three spectrograms.

The O I λ8446 Å line was clearly weaker than the neighboring Paschen lines in our spectra before 1996; this line is difficult to estimate in the period 1996–1999, because it falls at the edge of the TiO absorption band. However, it is clearly seen in 2000–2002 and is a factor of 3 more intense than the neighboring P_{17} λ8467 Å Paschen line.

EVOLUTION OF THE PARAMETERS OF THE GASEOUS ENVELOPE AND THE HOT COMPONENT

The approximately twofold decrease in the hydrogen-line fluxes from the nebula in the late 1990s compared to those in the period 1985–1987 is most likely due to the decrease in the electron density of the gaseous envelope by a factor of about 1.3 to 1.5, and

Table 7. Variations in the intensity ratio of the λ4363 [O III] and Hγ lines from 1976 until 2000

Date	JD 2400000+	$I(4363)/I(4340)$	Reference
December 19, 1976	43132	0.75	Arkhipova *et al.* (1979)
December 1976	~43130	0.75	Ciatti *et al.* (1977)
June 8, 1977	43303	0.54	Stauffer (1984)
June 1977	~43310	0.41	Davidson *et al.* (1978)
October 5, 1977	43422	0.37	Belyakina *et al.* (1978)
June 11, 1978	43671	1.08	Stauffer (1984)
August 11, 1978	43732	1.20	Stauffer (1984)
May 2, 1979	43996	1.41	Stauffer (1984)
May 22, 1979	44016	1.25	Stauffer (1984)
August 22, 1979	44108	1.39	Stauffer (1984)
August 24, 1979	44110	1.38	Stauffer (1984)
November 16, 1979	44163	1.56	Blair *et al.* (1981)
May 3, 1980	44363	1.61	Stauffer (1984)
May 19, 1980	44379	1.58	Stauffer (1984)
July 7, 1980	44428	1.59	Stauffer (1984)
September 6, 1980	44489	1.60	Stauffer (1984)
March 6, 1981	44670	1.68	Stauffer (1984)
June 6, 1982	45127	1.72	Stauffer (1984)
August 2, 1984	45915	1.31	Arkhipova and Noskova (1991)
August 3, 1985	46281	1.28	Arkhipova and Noskova (1991)
August 15, 1987	47023	1.35	Arkhipova and Noskova (1991)
November 15, 1987	47115	1.57	Schmid and Schild (1990)
June 22, 1988	47365	1.60	Pacheco (1992)
August 5, 1988	47379	1.33	Arkhipova and Noskova (1991)
August 22, 1989	47761	1.37	Arkhipova and Noskova (1991)
November 10, 1990	48206	1.38	Noskova, unpublished
July 20, 1991	48458	1.36	Noskova, unpublished
July 7, 1992	48811	1.28	Noskova, unpublished
July 10, 1993	49179	1.22	Noskova, unpublished
May 8, 1994	49481	1.06	This paper
June 15, 1994	49519	1.05	This paper
July 28, 1994	49562	1.28	Noskova, unpublished
July 15, 1995	49915	0.98	This paper
July 18, 1995	49917	1.17	Noskova, unpublished
July 25, 1995	49924	1.10	Noskova, unpublished
September 25, 1995	49986	1.05	This paper
October 9, 1996	50366	0.93	This paper
August 9, 1998	51045	0.80	This paper
August 8, 1999	51399	0.76	This paper
July 29, 2000	51755	0.72	This paper
June 25, 2001	52086	0.72	This paper
August 23, 2001	52145	0.60	This paper
October 13, 2001	52196	0.68	This paper
May 12, 2002	52407	0.67	This paper
September 3, 2002	52521	0.68	This paper

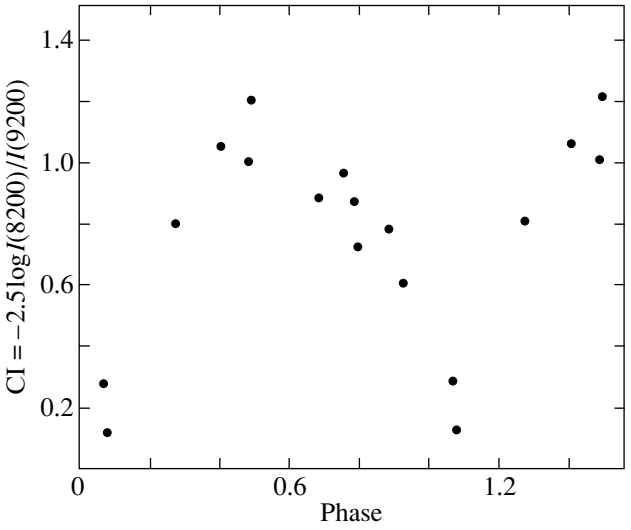

Fig. 5. Phase curve of the continuum color index CI = $-2.5\log(I(8200)/I(9200))$ with the pulsation period of the Mira star, $P = 540^{\rm d}$.

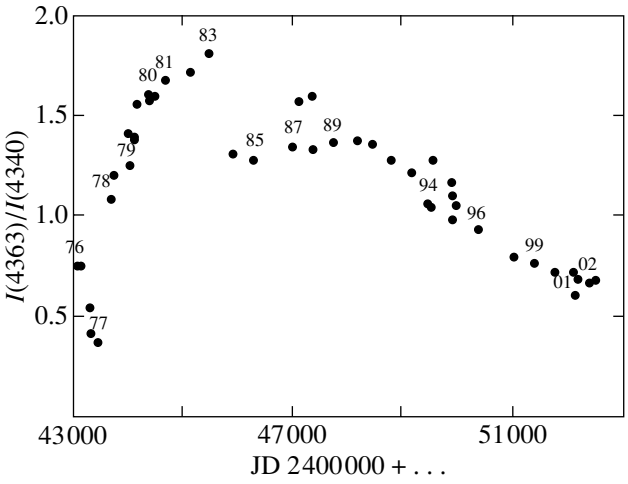

Fig. 6. Evolution of the intensity ratio of the λ4363 Å and Hγ lines from 1976 to 2002.

the intensity variations in the lines of neutral helium and other species is attributable to the increase in the degree of ionization of the nebula. The latter, in particular, is suggested by the increase in the intensity ratio of the λ4686 He II and Hβ lines, the relative strengthening of the [Fe VII] lines as the [Fe VI] lines weaken, etc.

In order to estimate the parameters of the nebula, it is extremely important to know the ratio of the auroral line and the nebular lines of doubly ionized oxygen, $R = I(4363)/I(N1 + N2)$. Its variation with time and its relationship to the U magnitude and the $U-B$ color are shown in Fig. 7. At densities of the gaseous envelope of HM Sge $N_{\rm e} \geq 10^6$ cm^{-3} (Blair *et al.* 1981; Pacheco *et al.* 1989; Arkhipova and Noskova 1991), this ratio significantly depends on two parameters, the electron temperature $T_{\rm e}$ and the electron density $N_{\rm e}$. The almost threefold decrease in the ratio from 1984 to 2002 is mainly attributable to the cooling of the nebula, because the gas density decreased by no more than 30–50% over this period. According to Pacheco *et al.* (1989), the envelope's electron temperature in the formation region of the [O III], [Fe VI], and [N II] lines in 1985–1986 was $T_{\rm e} = 14\,000$–$15\,000$ K. Mueller and Nussbaumer (1985) estimated the temperature in the [Ne V] line region to be 15 000 K, although our data (Arkhipova and Noskova 1991) yield a temperature closer to 19 000 K.

Taking $T_{\rm e} = 15\,000$ K in the period 1985–1987, we obtain $N_{\rm e} \sim 3 \times 10^6$ cm^{-3} for $R = 0.14$ (the value corrected for extinction with $E(B-V) = 0.6$ is $R_0 = 0.21$ (Arkhipova 1983)). In 2002, $R = 0.05$ at $N_{\rm e} \sim 2 \times 10^6$ cm^{-3} corresponds to $T_{\rm e} = 11\,000$ K. Thus, the electron temperature of the nebula near HM Sge decreased by about 4000 K over almost 20 yr.

As was mentioned above, the star's continuum in the blue spectral range (4200–5000 Å) was flat in the period 1994–2002, and its intensity in 2002 was a factor of 2 lower than that in 1986–1988. Arkhipova and Noskova (1991) showed that the observed continuum and the equivalent widths of the Hα–Hϵ hydrogen lines in 1986–1988 could be well fitted by the sum of emissions from a hot star with a temperature of 10^5 K and a hydrogen–helium envelope optically thin in plasma lines with a density $N_{\rm e} \sim 10^6$ cm^{-3} and an electron temperature of 10 000 K; the contribution of the star to the continuum at a wavelength of 5000 Å was 40% of the total flux at this wavelength. If, however, we take the electron temperature to be 15 000 K and the ionized and neutral helium abundances in accordance with the chemical composition of the envelope derived by Pacheco *et al.* (1989), then the mean observed equivalent widths of the Hβ and Hγ lines in the mid-1980s ($W(\text{H}\beta) = 700 \pm 20$ Å, $W(\text{H}\gamma) = 246 \pm 20$ Å) can be reconciled with the "hot star + gaseous envelope" model for the star's relative contribution of 0.4.

Of the total continuum flux at $\lambda = 5000$ Å, $F_1 = 2.8 \times 10^{-14}$ erg cm^{-2} s^{-1} Å^{-1}, the hot star and the nebular continuum in the mid-1980s accounted for $F_{1\star} = 1.1 \times 10^{-14}$ erg cm^{-2} s^{-1} Å^{-1} and $F_n = 1.7 \times 10^{-14}$ erg cm^{-2} s^{-1} Å^{-1}, respectively. The computed and observed Balmer jumps were 0.56 and 0.45 ± 0.20 (Arkhipova and Noskova 1991), respectively.

A similar procedure that we applied to the equivalent widths of the Hβ and Hγ lines observed in 2002

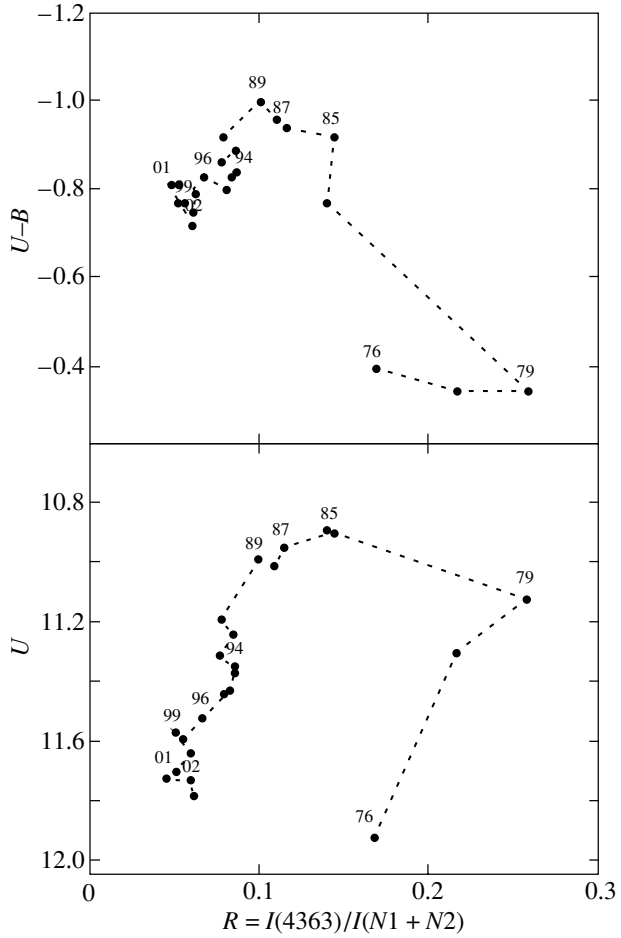

Fig. 7. $R = I(4363)/I(N1 + N2)$ versus U magnitude and $U-B$ color.

($W(\mathrm{H}\beta) = (820 \pm 50)$ Å and $W(\mathrm{H}\gamma) = (320 \pm 20)$ Å at the effective temperature T_e=11 000 K) leads to a model where the contribution from the star at $\lambda =$ 5000 Å was 35%. At the total continuum intensity $F_2 = 1.4 \times 10^{-14}$ erg cm^{-2} s^{-1} Å^{-1}, the hot star accounted for $F_{2\star} = 0.5 \times 10^{-14}$ erg cm^{-2} s^{-1} Å^{-1}. The hot component faded optically by almost 1^m over 20 yr. The relative contribution of the envelope increased with time, probably not only in the continuum, but also in the emission lines, despite the decrease in its absolute fluxes.

CONCLUSIONS

Below, we summarize our main results:

(1) In 1994–2002, we continued our photoelectric UBV observations of the symbiotic nova HM Sge. We showed that its brightness in the B and V bands continued to decline at a rate of $0^m.05$ per year. The $B-V$ and $U-B$ color indices mainly reflected the change in the effect of emission lines and, in part, the change in the contribution of the erupted component.

(2) The 1994–2002 spectroscopic observations in the red and near-IR range ($6100 < \lambda < 10\,000$ Å) revealed the continuum of the red component (the Mira star): the continuum intensity varied significantly with phase of the 540-day pulsation period, with the amplitude increasing with wavelength. In general, the optical depth of the dust envelope around the Mira star appeared to have decreased appreciably. In addition, we observed two minima of the IR-continuum intensity separated by a period of about six years. They may be attributable to changes in the visibility conditions for the inhomogeneous dust envelope around the Mira star during its orbital motion or, less likely, to its activity.

(3) The intensity of the emission spectrum of the gaseous envelope has evolved significantly in the last 20 yr. Compared to the 1985–1987 data, the absolute flux decreased by a factor of about 2 in hydrogen lines and by a factor of 3 or more in neutral helium lines, because the degree of ionization of helium increased. The absolute fluxes in He II lines changed only slightly, although compared to Hβ, the He II lines grew stronger by approximately 20%. The forbidden [O III], [Fe VI], and [Fe VII] lines weakened by a factor of about 2, but the weakening of the auroral lines of these ions was much larger. [Ca VII] lines appeared and became noticeable. The flux in the Raman O VI λ6825 Å line increased significantly (by a factor of 5 to 10). The degree of ionization of the nebula continued to increase, most likely because the temperature of the exciting star rose.

(4) As previously, the star's continuum in the blue spectral range remained flat, but its intensity decreased by a factor of 2 in 20 yr. The relative contribution from the continuum of the hot component decreased, which corresponds to its fading by about 1^m near λ5000 Å.

(5) The parameters of the star's gaseous envelope have changed noticeably: the electron density decreased by a factor of about 1.5, while the electron temperature in the [O III]-line region dropped from 14 000–15 000 K to 11 000 K. The observed intensity ratio of the auroral and nebular O III lines decreased from $R = 0.14$ in 1986 to $R = 0.05$ in 2002.

ACKNOWLEDGMENTS

This study was supported by the Federal Science and Technology Astronomy Program (project no. 40.022.1.1.1103).

REFERENCES

1. V. P. Arkhipova, Tr. Gos. Astron. Inst. im. Shternberga **53**, 85 (1983).
2. V. P. Arkhipova and R. I. Noskova, Pis'ma Astron. Zh. **17**, 440 (1991) [Sov. Astron. Lett. **17**, 188 (1991)].
3. V. P. Arkhipova, O. D. Dokuchaeva, and V. F. Esipov, Astron. Zh. **56**, 313 (1979) [Sov. Astron. **23**, 174 (1979)].
4. V. P. Arkhipova, O. D. Dokuchaeva, and R. I. Noskova, Pis'ma Astron. Zh. **20**, 723 (1994) [Astron. Lett. **20**, 623 (1994)].
5. T. S. Belyakina, R. E. Gershberg, and N. I. Shakhovskaya, Pis'ma Astron. Zh. **4**, 406 (1978) [Sov. Astron. Lett. **4**, 219 (1978)].
6. T. S. Belyakina, V. P. Arkhipova, O. D. Dokuchaeva, and R. I. Noskova, Izv. Krymsk. Astrofiz. Obs. **78**, 43 (1988).
7. W. P. Blair, R. E. Stensel, G. Shaviv, and W. A. Feibelman, Astron. Astrophys. **99**, 73 (1981).
8. F. Ciatti, A. Mammano, and A. Vitone, Astron. Astrophys. **61**, 459 (1977).
9. K. Davidson, R. M. Humphreys, and K. M. Merrill, Astrophys. J. **220**, 239 (1978).
10. O. D. Dokuchaeva, Inf. Bull. Var. Stars, No. 1189 (1976).
11. V. G. Klochkova, private communication (2003).
12. U. Munari, Astron. Astrophys. **207**, L8 (1988).
13. B. E. A. Mueller and H. Nussbaumer, Astron. Astrophys. **145**, 144 (1985).
14. R. I. Noskova, Pis'ma Astron. Zh. **22**, 841 (1996) [Astron. Lett. **22**, 755 (1996)].
15. S. Parimucha, V. P. Arkhipova, D. Chochol, *et al.*, Contrib. Astron. Obs. Skalnate Pleso **30**, 99 (2000).
16. J. A. F. Pacheco and R. D. D. Costa, Astron. Astrophys. **257**, 619 (1992).
17. J. A. F. Pacheco, S. J. Codina-Landaberry, and D. F. Lopes, Astrophys. J. **337**, 520 (1989).
18. R. J. Rudy, S. R. Meier, G. S. Rossano, *et al.*, Astrophys. J., Suppl. Ser. **121**, 533 (1999).
19. J. R. Stauffer, Astrophys. J. **280**, 695 (1984).
20. H. M. Schmid and H. S. Schild, Mon. Not. R. Astron. Soc. **246**, 84 (1990).
21. O. G. Taranova and V. I. Shenavrin, Pis'ma Astron. Zh. **26**, 695 (2000) [Astron. Lett. **26**, 600 (2000)].
22. I. B. Voloshina, I. N. Glushneva, V. T. Doroshenko, *et al., Spectrophotometry of Brightest Stars* (Nauka, Moscow, 1982) [in Russian].
23. P. Whitelock, *IAU Coll. No. 103: The Symbiotic Phenomenon,* Ed. by J. Mikolajewka *et al.* (Kluwer Acad., Dordrecht, 1988), p. 47.

Translated by N. Samus'

Astronomy Letters, Vol. 30, No. 4, 2004, pp. 268–275. Translated from Pis'ma v Astronomicheskiĭ Zhurnal, Vol. 30, No. 4, 2004, pp. 307–314.

MHD Waves in Coronal Loops with a Shell

B. B. Mikhalyaev[1]* and A. A. Solov'ev[2]**

[1]*Kalmyk State University, Russia*

[2]*Pulkovo Astronomical Observatory, Russian Academy of Sciences, Pulkovskoe shosse 65, St. Petersburg, 196140 Russia*

Received May 22, 2003

Abstract—We consider a model of a coronal loop in the form of a cord surrounded by a coaxial shell. Two slow magnetosonic waves longitudinally propagate within a thin flux tube on the $m = 0$ cylindrical mode with velocities close to the tube velocities in the cord and the shell. One wave propagates inside the cord, while the other propagates inside the shell. A peculiar feature of the second wave is that the plasma in the cord and the shell oscillates with opposite phases. There are two fast magnetosonic waves on each of the cylindrical modes with $m > 0$. If the plasma density in the shell is lower than that in the surrounding corona, then one of the waves is radiated into the corona, which causes the loop oscillations to be damped, while the other wave is trapped by the cord, but can also be radiated out under certain conditions. If the plasma density in the shell is higher than that in the cord, then one of the waves is trapped by the shell, while the other wave can also be trapped by the shell under certain conditions. In the wave trapped by the shell and the wave radiated by the tube, the plasma in the cord and the shell oscillates with opposite phases.

Key words: *Sun, coronal loops, oscillations, damping.*

INTRODUCTION

Numerous observations in various wavelength ranges reveal a complex pattern of wave processes in the solar atmosphere. Intensity modulation of type-IV radio bursts with periods on the order of several hundred seconds in the decimeter range and on the order of several seconds in the meter range (Meerson *et al.* 1978) is observed; the number of oscillations can reach several hundred. The intensity modulation is attributed, in particular, to the magnetohydrodynamic (MHD) oscillations of the loops themselves (Meerson *et al.* 1978; Zaitsev and Stepanov 1982, 1989; Kopylova *et al.* 2002). Modulation of the radio emissions that are probably generated inside spatially close optically thin and optically thick sources with opposite modulation phases is occasionally observed (Qin *et al.* 1996). This phenomenon can be most naturally explained by the fact that the radiating loop consists of two parts with different plasma densities and that the oscillations in them are in antiphase.

The Extreme Ultraviolet Imaging Telescope (EIT) onboard the SOHO satellite has revealed regions of enhanced intensity in coronal loops in the 195 Å line that propagate along the loop. Similar propagating structures have also been discovered by the Transition Region and Coronal Explorer (TRACE) ultraviolet space telescope in the 171 Å line (De Moortel *et al.* 2000, 2002; Nakariakov *et al.* 2000; Tsiklauri and Nakariakov 2001). Their propagation speeds lie within the range 65 to 165 km s^{-1}; i.e., they are close to the sound speed at typical loop temperatures (Tsiklauri and Nakariakov 2001). The viewpoint that these structures are associated with slow magnetosonic waves propagating along coronal loops prevails among all the existing explanations of this phenomenon. Analysis of the SOHO/EIT and TRACE data obtained on May 13, 1998, revealed the simultaneous existence of two such waves in the same loop that propagated at speeds of 95 and 110 km s^{-1} (Robbrecht *et al.* 2001). The loop was assumed to have a complex internal structure and to consist of the central part (cord) and the surrounding shell; the cord and the shell are at different temperatures, with the temperature changing sharply at the boundary between them. Thus, there are two distinctly different sound speeds in the loop.

In recent years, the TRACE observations (Aschwanden *et al.* 1999; Nakariakov *et al.* 1999) of transverse coronal loop oscillations have attracted particular attention, because, in a sense, they opened a new page in solar physics. The oscillations that have long been studied by theorists in searching for

*E-mail: phys@kalmsu.ru
**E-mail: solov@kalmsu.ru

the physical cause of coronal heating and coronal emission modulation have for the first time become directly observable in ultraviolet heliograms. It has become possible not only to determine the oscillation periods and geometrical sizes of loops, but even to measure the amplitude of their transverse oscillations and damping rates.

The very simple model of a uniform magnetic flux tube (Meerson *et al.* 1978; Wilson 1980; Spruit 1982; Edwin and Roberts 1982; Roberts *et al.* 1984) is commonly used to theoretically analyze the oscillation properties of coronal loops. In this model, the loop is a circular tube inside and outside which the plasma density and the magnetic field strength are uniform. Their values and the gas pressures are different, but they correspond to the transverse equilibrium condition for the tube. In the approximation of a thin tube, where its radius is much smaller than the length of the wave under consideration, i.e., $k_z a \ll 1$, where a is the tube radius, and k_z is the longitudinal (along the tube axis) wave number, the dispersion relation for cylindrical waves with numbers $m > 0$ (for example, the $m = 1$ wave is the kink mode) is (Edwin and Roberts 1982; Spruit 1982; Roberts *et al.* 1984)

$$\rho_{0i}(\omega^2 - V_{\mathrm{A}i}^2 k_z^2) + \rho_{0e}(\omega^2 - V_{\mathrm{A}e}^2 k_z^2) = 0. \quad (1)$$

Here, ρ_{0i} and ρ_{0e} are the plasma densities in the tube and its surroundings, respectively. The oscillations have the pattern of a fast magnetosonic wave that was trapped by the tube and that propagates inside it. For the $m = 0$ wave that describes the sausage mode in the limit $k_z a \to 0$, the following relation holds (Spruit 1982; Roberts *et al.* 1984):

$$\omega^2 - C_{\mathrm{T}i}^2 k_z^2 = 0, \quad (2)$$

where $C_{\mathrm{T}i}$ is the tube velocity inside the tube. The oscillations have the pattern of a slow magnetosonic wave that also longitudinally propagates inside the tube if the plasma temperature inside the tube is higher than the plasma temperature in the surrounding space.

This is a greatly simplified loop model. It does not allow us to consider many physical effects, for example, the radiation of MHD waves into the surrounding space, which is an efficient damping mechanism of its oscillations. Therefore, oscillation energy dissipation mechanisms related to the anomalously high viscosity of the medium (Nakariakov *et al.* 1999), the resonant absorption of energy in a narrow layer between the loop and the surrounding corona (Ruderman and Roberts 2002), or the radiation of acoustic waves (Stenuit *et al.* 1998, 1999) are invoked to account for the rapid damping of the transverse loop oscillations observed with TRACE.

In this paper, we suggest a model of a coronal loop in the form of a magnetic flux tube that consists of a cord and the surrounding coaxial shell. This model is more realistic, because, to the first approximation, it takes into account the high degree of nonuniformity in the radial distribution of loop parameters. The oscillation spectrum in a tube with a shell is much richer than that for a uniform tube. The following physical effects mentioned above that were observed in the corona can be explained by studying the MHD waves that exist in such a tube: the antiphase oscillations of the denser and more rarefied parts of the loop, the existence of two slow magnetosonic waves propagating along the loop, and the damping of transverse loop oscillations.

This paper has the following structure: In the first section, we describe the model of a tube with a shell, write out the equations, and discuss the form of cylindrical MHD modes. In the second section, we describe the cylindrical $m = 0$ modes in the thin-tube approximation, derive the dispersion relation, and determine the conditions under which the waves can propagate in a particular region. A similar analysis for the cylindrical modes with $m > 0$ is performed in the third section. The transverse oscillations of coronal loops mentioned above are described by the $m = 1$ mode; we give the damping rate for this mode. In the fourth section, we present our results and discuss their application to solar coronal phenomena.

THE LOOP MODEL AND BASIC EQUATIONS

Let us consider a cylinder of radius a with a radially nonuniform plasma density distribution that, for simplicity, will be fitted by a step function of the form

$$\rho_0(r) = \begin{cases} \rho_{0i}, & r < b \\ \rho_{0m}, & b < r < a. \end{cases}$$

where b is the radius of the separated central part that we call a cord. The plasma density ρ_{0i} in the cord is assumed to be higher than the plasma density in the space surrounding the cylinder, which we denote by ρ_{0e}. The $b < r < a$ region between the cord and the surroundings of the cylinder is called a shell. Below, the subscripts i, m, e denote the values pertaining to the cord, the shell, and the surroundings of the tube, respectively. The magnetic field in all of these three regions is assumed to be uniform and directed along the cylinder axis; the magnetic field strengths are denoted by B_{0i}, B_{0m}, B_{0e}. The value of B_{0e} gives the strength of the external magnetic field. Thus, we consider a complex magnetic flux tube that consists of the cord and the shell. The magnetostatic equilibrium condition for the tube in an external magnetic field is

$$p_{0i} + \frac{B_{0i}^2}{8\pi} = p_{0m} + \frac{B_{0m}^2}{8\pi} = p_{0e} + \frac{B_{0e}^2}{8\pi}. \quad (3)$$

The quantities p_{0i}, p_{0m}, p_{0e} denote the gas pressures; they are constant. The Alfvén and sound speeds are $V_{Ai}, C_{si}, V_{Am}, C_{sm}, V_{Ae}, C_{se}$. In coronal conditions, we may assume that $V_{Ai} < V_{Ae}$ and $C_{si} > C_{se}$.

In each region, we will consider small perturbations described by the linearized equations of ideal MHD:

$$\rho_0 \frac{\partial \mathbf{v}}{\partial t} = -\nabla p + \mathrm{curl}\mathbf{B} \times \mathbf{B}_0/4\pi, \quad (4)$$
$$\frac{\partial p}{\partial t} + \gamma p_0 \mathrm{div}\mathbf{v} = 0,$$
$$\frac{\partial \mathbf{B}}{\partial t} = \mathrm{curl}(\mathbf{v} \times \mathbf{B}_0),$$

where $\mathbf{B}_0, p_0, \rho_0$ are the unperturbed magnetic field strength, plasma pressure, and density; and $\mathbf{B}, p, \mathbf{v}$ are the perturbations of magnetic field strength, pressure, and velocity, respectively. We will represent the solutions as cylindrical waves. In this case, the perturbations of radial velocity v_r, pressure p, and longitudinal magnetic field strength B_z can be expressed in terms of functions of the form $f(r,t) = f(r)\cos(m\phi)\cos(k_z z)\exp(-i\omega t)$, where ω is the oscillation frequency, and k_z is the longitudinal (along the tube axis) wave number. The components v_ϕ, v_z, B_r, B_ϕ are also nonzero and have a similar structure (they are involved in system (4), appearing in the perturbation vectors). However, since we do not use their explicit expressions, we do not write them out separately. The perturbation of total pressure is $P(r) = p(r) + B_0 B_z(r)/4\pi$, where $p(r)$ is the gas pressure perturbation, and $B_0 B_z(r)/4\pi$ is the magnetic pressure perturbation. We find from the system of equations (4) for $v_r(r)$ and $P(r)$ that

$$v_r(r) = -\frac{i\omega}{(\omega^2 - V_\mathrm{A}^2 k_z^2)\rho_0}\frac{dP(r)}{dr}, \quad (5)$$

and the function $P(r)$ satisfies the equation

$$r^2\frac{d^2P}{dr^2} + r\frac{dP}{dr} + (k^2r^2 - 1)P = 0, \quad (6)$$

where we use the notation

$$k^2 = \frac{(\omega^2 - V_\mathrm{A}^2 k_z^2)(\omega^2 - C_\mathrm{s}^2 k_z^2)}{(V_\mathrm{A}^2 + C_\mathrm{s}^2)(\omega^2 - C_\mathrm{T}^2 k_z^2)}, \quad (7)$$
$$C_\mathrm{T}^2 = \frac{V_\mathrm{A}^2 C_\mathrm{s}^2}{V_\mathrm{A}^2 + C_\mathrm{s}^2}.$$

The parameter k has the meaning of a radial wave number. The quantity C_T is called the tube velocity. Depending on the relationship between the wave phase velocity ω/k_z and the speeds $V_\mathrm{A}, C_\mathrm{s}, C_\mathrm{T}$, either $k^2 > 0$ or $k^2 < 0$; i.e., the radial wave number can take on real or purely imaginary values. In this case, the solution of Eq. (6) can be expressed in terms of the solutions of the Bessel equation or the modified Bessel equation, describing the bulk or surface wave, respectively.

We write the solution of Eqs. (5)–(6) in the three regions via $\{v_{ri}(r), P_i(r)\}$, $\{v_{rm}(r), P_m(r)\}$, $\{v_{re}(r), P_e(r)\}$ and subject them to the boundary conditions

$$v_{ri}(b) = v_{rm}(b), \quad v_{rm}(a) = v_{re}(a), \quad (8)$$

$$P_i(b) = P_m(b), \quad P_m(a) = P_e(a), \quad (9)$$

from which we will then determine the dependence of ω on k_z, i.e., the dispersion relation. Since the form of the dispersion relation depends on the cylindrical mode number m, we will consider the $m = 0$ and $m > 0$ modes separately.

SLOW MAGNETOSONIC WAVES

Let us consider the zero ($m = 0$) cylindrical mode that describes the sausage disturbances. According to (5)–(6), the solution in the cord can be expressed in terms of $R(k_i r)$, where $R(z)$ is either the Bessel function $J_0(z)$ if the wave is a bulk one or the modified Bessel function $I_0(z)$ if the wave is a surface one:

$$v_{ri}(r) = -i\omega\exp(i\alpha)X_{0i}\frac{R'(k_i r)}{R'(k_i b)}, \quad (10)$$
$$P_i(r) = \exp(i\alpha)X_{0i}\frac{\rho_{0i}(\omega^2 - V_{\mathrm{A}i}^2 k_z^2)}{k_i}\frac{R(k_i r)}{R'(k_i b)}.$$

The necessity of introducing the additional phase factor $\exp(i\alpha)$ is explained below. If the wave is a surface one, i.e., if the condition $k^2 < 0$ is satisfied for the cord, then by k_i we will mean $\sqrt{-k^2}$. The same will be borne in mind when describing the waves in other regions.

By analogy, we represent the solution in the surrounding space as

$$v_{re}(r) = -i\omega X_{0e}\frac{Q'(k_e r)}{Q'(k_e a)}, \quad (11)$$
$$P_e(r) = X_{0e}\frac{\rho_{0e}(\omega^2 - V_{\mathrm{A}e}^2 k_z^2)}{k_e}\frac{Q(k_e r)}{Q'(k_e a)}.$$

Here, we take either $H_0^{(1)}(z)$ or $K_0(z)$ as $Q(z)$.

In this representation of the solutions, the radial velocities on the cord and shell surfaces are

$$v_{ri}(b) == \omega X_{0i}\cos(m\phi)\cos(k_z z)$$
$$\times \exp(-i\omega t - i\pi/2 + i\alpha),$$
$$v_{re}(a) = \omega X_{0e}\cos(m\phi)\cos(k_z z)\exp(-i\omega t - i\pi/2).$$

Thus, we see that the coefficients X_{0i} and X_{0e} have the meaning of oscillation amplitudes on the cord and

shell surfaces, and α is the phase shift of the cord oscillations relative to the shell oscillations.

We write the solution in the shell as

$$v_{rm}(r) = -i\omega(AU'(k_m r) + CV'(k_m r)), \quad (12)$$

$$P_m(r) = \frac{\rho_{0m}(\omega^2 - V_{\mathrm{A}m}^2 k_z^2)}{k_m}(AU(k_m r) + CV(k_m r)).$$

Here, $U(z)$ and $V(z)$ are the two linearly independent solutions of Eq. (6) in the $b < r < a$ region; we also define them via the solutions of either the Bessel equation or the modified Bessel equation.

We obtain from the boundary conditions (8)–(9)

$$\exp(i\alpha)X_{0i} = AU'(k_m b) + CV'(k_m b), \quad (13)$$

$$X_{0e} = AU'(k_m a) + CV'(k_m a);$$

$$\exp(i\alpha)X_{0i}\frac{\rho_{0i}}{k_i}(\omega^2 - V_{\mathrm{A}i}^2 k_z^2)\frac{R(k_i b)}{R'(k_i b)} \quad (14)$$

$$= \frac{\rho_{0m}}{k_m}(\omega^2 - V_{\mathrm{A}m}^2 k_z^2)(AU(k_m b) + CV(k_m b)),$$

$$X_{0e}\frac{\rho_{0e}}{k_e}(\omega^2 - V_{\mathrm{A}e}^2 k_z^2)\frac{Q(k_e a)}{Q'(k_e a)}$$

$$= \frac{\rho_{0m}}{k_m}(\omega^2 - V_{\mathrm{A}m}^2 k_z^2)(AU(k_m a) + CV(k_m a)).$$

We will consider conditions (13)–(14) in the thin-tube approximation by assuming that $k_z a << 1$; i.e., the tube radius is much smaller than the lengths of the waves under consideration. It then follows from (7) that $ka \ll 1$ and $kb \ll 1$ for all of the three regions, and instead of the solution of the Bessel equation and the modified Bessel equation, we may restrict ourselves to several terms of their expansion into a series. Retaining only the principal expansion terms, we can obtain

$$\frac{J_0(k_i b)}{k_i J_0'(k_i b)} \approx -\frac{I_0(k_i b)}{k_i I_0'(k_i b)} \approx -\frac{2}{k_i^2 b},$$

$$\frac{H_0^{(1)}(k_e a)}{k_e H_0^{(1)'}(k_e a)} \approx \frac{K_0(k_e a)}{k_e K_0'(k_e a)} \approx a\ln(k_e a).$$

It thus follows that the form of the solution in the surrounding space in the zero approximation does not affect the form of the dispersion relation.

We obtain from (13) and (14)

$$\mu\exp(i\alpha)X_{0i}\rho_{0i}(\omega^2 - V_{\mathrm{A}i}^2 k_z^2)\frac{1}{k_i^2 b} \quad (15)$$

$$= \nu\rho_{0m}(\omega^2 - V_{\mathrm{A}m}^2 k_z^2)\frac{aX_{0e} - b\exp(i\alpha)X_{0i}}{k_m^2(a^2 - b^2)},$$

$$X_{0e}\rho_{0e}(\omega^2 - V_{\mathrm{A}e}^2 k_z^2)\frac{1}{2}\ln(\frac{k_e a}{2})$$

$$= \nu\rho_{0m}(\omega^2 - V_{\mathrm{A}m}^2 k_z^2)\frac{aX_{0e} - b\exp(i\alpha)X_{0i}}{k_m^2(a^2 - b^2)}.$$

Here, $\mu = -1$ for the bulk wave in the cord, $\mu = 1$ for the surface wave in the cord, $\nu = -1$ for the bulk wave in the shell, and $\nu = 1$ for the surface wave in the shell. Setting the determinant of system (15) equal to zero, in the limit $k_z \to 0$, we obtain the equation

$$\frac{(\omega^2 - V_{\mathrm{A}i}^2 k_z^2)}{k_i^2}\frac{(\omega^2 - V_{\mathrm{A}m}^2 k_z^2)}{k_m^2} = 0;$$

whence it follows that

$$(\omega^2 - C_{\mathrm{T}i}^2 k_z^2)(\omega^2 - C_{\mathrm{T}m}^2 k_z^2) = 0. \quad (16)$$

Relation (16) gives the limiting velocities of the two zero cylindrical or sausage modes for $k_z a \to 0$. Since the modes propagate with velocities close to the tube velocities, they are slow magnetosonic (SMS) waves. Comparing (16) and (2), we see that an additional mode emerges when passing from a uniform tube to a tube with a shell.

Observations reveal the existence of two SMS waves that simultaneously propagate along the coronal loop with similar velocities (95 and 110 km s^{-1}) (Robbrecht *et al.* 2001). The tube velocities of our model may well play the role of these velocities. At a characteristic coronal temperature of 1.0×10^6 K, the sound speed is 117.4 km s^{-1}; for an Alfvén speed of 330 km s^{-1}, formulas (7) then yield a tube velocity of 110.6 km s^{-1}. For a temperature of 0.7×10^6 K at the same Alfvén speed, the tube velocity is found to be 94.1 km s^{-1}. Thus, the existence of two speeds can be explained by different plasma temperatures in the cord and the shell. We conclude that these observations provide circumstantial evidence for the existence of coronal loops in the form of a cord surrounded by a shell.

For a wave with a phase velocity $C_{\mathrm{T}i} < \omega/k_z < C_{si}$, the condition $k_i^2 > 0$ is satisfied; it is a bulk wave in the cord. Since the Alfvén speeds in the corona are much higher than the sound speed, the tube velocities are close to the corresponding sound speeds; the signs of k_m^2 and k_e^2 then depend on the relationship between the sound speeds in the cord, the shell, and the surroundings. Since the temperature in the cord is higher than the temperature in the surrounding corona, $k_e^2 < 0$ and the wave does not propagate in the external corona. For the shell, $k_m^2 < 0$, irrespective of the relationship between the sound speeds in the cord and the shell, provided that the temperatures in the cord and the shell differ significantly, so that the $(C_{\mathrm{T}i}, C_{si})$ and $(C_{\mathrm{T}m}, C_{sm})$ intervals do not overlap. Thus, the first wave is a bulk one only inside the cord; it is trapped by the cord. For the second wave with a phase velocity $C_{\mathrm{T}m} < \omega/k_z < C_{sm}$, we can similarly

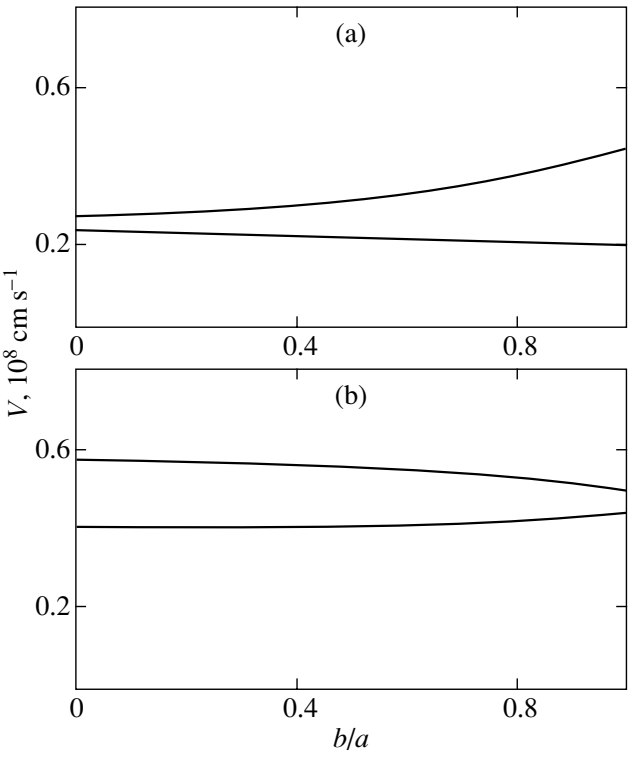

Fig. 1. Phase velocities $V = \omega/k_z$ of the FMS waves trapped by the tube versus ratio b/a of the cord and shell radii. As an example, we consider $V_{Ai} = 0.35 \times 10^8$ cm s^{-1} and $V_{Ae} = 0.70 \times 10^8$ cm s^{-1} with $V_2 = 0.44 \times 10^8$ cm s^{-1}. The following cases are presented separately: (a) $V_{Am} = 0.20 \times 10^8$ cm s^{-1}, where $V_1 = 0.25 \times 10^8$ cm s^{-1} and $V_3 = 0.27 \times 10^8$ cm s^{-1}; (b) $V_{Am} = 0.50 \times 10^8$ cm s^{-1}, where $V_1 = 0.41 \times 10^8$ cm s^{-1} and $V_3 = 0.58 \times 10^8$ cm s^{-1}.

show that it is a bulk wave only inside the shell; it may be called the wave trapped by the shell.

Since the first wave is a bulk one in the cord, we should take $\mu = -1$ in Eqs. (15). Clearly, in this case, the phase factor is $\exp(i\alpha) = 1$, implying that the cord and the shell oscillate with the same phase. The situation with the second wave propagating in the shell is different. Here, $\mu = 1$, and, necessarily, $\exp(i\alpha) = -1$, i.e., the phase shift is π; therefore, the cord and the shell oscillate with opposite phases. Such an effect is consistent with observational data (Qin *et al.* 1996), which points to the existence of antiphase oscillations in optically thin and optically thick regions. We suggest that there is modulation of the radio emission generated in a coronal loop with dense and rarefied parts, i.e., composed of a cord and a shell.

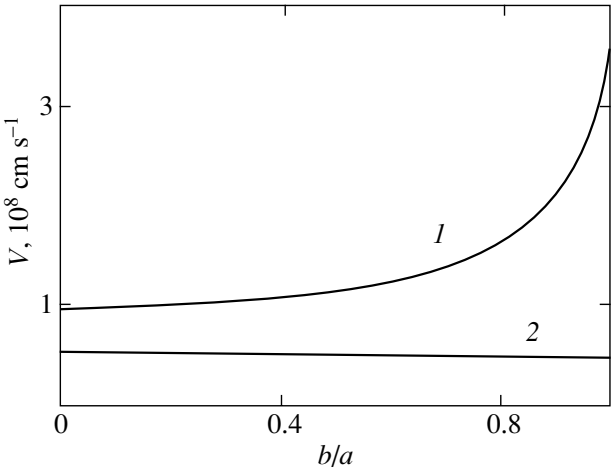

Fig. 2. Phase velocities of the FMS waves versus ratio b/a for $V_{Am} > V_{Ae}$. We consider $V_{Ai} = 0.39 \times 10^8$ cm s^{-1}, $V_{Ae} = 0.70 \times 10^8$ cm s^{-1}, and $V_{Am} = 3.5 \times 10^8$ cm s^{-1}: curve *1* for the faster FMS wave radiated into the corona; curve *2* for the slower FMS wave trapped by the tube.

FAST MAGNETOSONIC WAVES

Let us consider the cylindrical modes with numbers $m > 0$. The $m = 1$ mode describes the transverse (kink) tube oscillations. In this case, the boundary conditions (8)–(9) in the thin-tube approximation lead to the equations

$$\exp(i\alpha)X_{0i}\rho_{0i}(\omega^2 - V_{Ai}^2k_z^2) = \rho_{0m}(\omega^2 - V_{Am}^2k_z^2) \times \frac{(2a^{m+1}b^{m-1}X_{0e} - (a^{2m} + b^{2m})\exp(i\alpha)X_{0i})}{(a^{2m} - b^{2m})}, \quad (17)$$

$$-X_{0e}\rho_{0e}(\omega^2 - V_{Ae}^2k_z^2) = \rho_{0m}(\omega^2 - V_{Am}^2k_z^2) \times \frac{((a^{2m} + b^{2m})X_{0e} - 2a^{m-1}b^{m+1}\exp(i\alpha)X_{0i})}{(a^{2m} - b^{2m})};$$

whence the following dispersion relation can be derived:

$$(a^{2m} - b^{2m})(\rho_{0m}^2(\omega^2 - V_{Am}^2k_z^2)^2 + \rho_{0i}(\omega^2 - V_{Ai}^2k_z^2)\rho_{0e}(\omega^2 - V_{Ae}^2k_z^2)) + (a^{2m} + b^{2m})\rho_{0m}(\omega^2 - V_{Am}^2k_z^2)(\rho_{0i}(\omega^2 - V_{Ai}^2k_z^2) + \rho_{0e}(\omega^2 - V_{Ae}^2k_z^2)) = 0. \quad (18)$$

The waves with this dispersion relation are fast magnetosonic (FMS) waves. Its solutions yield the limiting phase velocities of the two FMS waves for $k_z \to 0$. These velocities depend on the ratio of the cord and shell radii, b/a; the dependences are plotted in Figs. 1 and 2. At $V_{Am} < V_{Ai}$, the velocity of the faster wave changes from V_3 to V_2 as b changes from

0 to a, while the velocity of the slower wave changes from V_1 to $V_{\mathrm{A}m}$. Here,

$$V_1^2 = \frac{\rho_{0m}V_{0m}^2 + \rho_{0i}V_{0i}^2}{\rho_{0m} + \rho_{0i}},$$
$$V_2^2 = \frac{\rho_{0i}V_{0i}^2 + \rho_{0e}V_{0e}^2}{\rho_{0i} + \rho_{0e}},$$
$$V_3^2 = \frac{\rho_{0m}V_{0m}^2 + \rho_{0e}V_{0e}^2}{\rho_{0m} + \rho_{0e}}.$$

At $V_{\mathrm{A}i} < V_{\mathrm{A}m} < V_{\mathrm{A}e}$, the velocity of the faster wave changes from V_3 to $V_{\mathrm{A}m}$, while the velocity of the slower wave changes from V_1 to V_2.

At $V_{\mathrm{A}m} > V_{\mathrm{A}e}$, one FMS wave propagates radially, i.e., is radiated by the tube; its phase velocity exceeds the Alfvén speed in the surrounding space (Fig. 2). As b changes from 0 to a, it changes from V_3 to $V_{\mathrm{A}m}$. The phase velocity of the second FMS wave changes from V_1 to V_2. It can also be radiated out when the following condition is satisfied:

$$V_1 > V_{\mathrm{A}e}. \quad (19)$$

Otherwise, it is trapped by the cord.

The conditions $\omega/k_z > V_{\mathrm{A}i}$ and $\omega/k_z > V_{\mathrm{A}e}$ are satisfied for the radiated waves. In this case, it follows from (17) that $\exp(i\alpha) = -1$. This implies that $\alpha = \pi$ and the cord and the shell oscillate with opposite phases. A similar situation takes place for $V_{\mathrm{A}m} < V_{\mathrm{A}i}$, when the conditions $\omega/k_z < V_{\mathrm{A}i}$ and $\omega/k_z < V_{\mathrm{A}e}$ are satisfied for the wave trapped by the shell. The slower mode is always trapped by the shell, while the faster mode can be trapped if the following condition is satisfied:

$$V_3 < V_{\mathrm{A}i}. \quad (20)$$

The fast mode generated in the tube and then radiated into the surrounding space may be responsible for the damping of the tube oscillations. Observations reveal that the transverse oscillations of coronal loops are rapidly damped (Aschwanden *et al.* 1999; Nakariakov *et al.* 1999). Theoretically, the damping manifests itself by the presence of an imaginary part in the solution of the dispersion relation. Formula (18) gives the dispersion relation in the zero approximation; when deriving it, we retained only the principal terms of the expansions of our solutions of Eq. (6). In the zero approximation, as we saw, the solution of the dispersion relation is real; hence, the damping appears in the first approximation as a weak effect.

To obtain the first approximation, we must retain the next expansion terms in the solutions of Eq. (6). If we write $\omega = \omega_0(1 + \epsilon)$, where ω_0 is the zero approximation, then $\epsilon \ll 1$ gives the first correction. The quantity $Q = 1/(2|Im\epsilon|)$ is the Q factor of the oscillations. We can derive from the dispersion relation in the first approximation (Solov'ev *et al.* 2003)

$$8V^2 Im\epsilon\{(a^2 - b^2)[\rho_{0i}\rho_{0e}(2V^2 - V_{\mathrm{A}i}^2 - V_{\mathrm{A}e}^2) + 2\rho_{0m}^2(V^2 - V_{\mathrm{A}m}^2)] + (a^2 + b^2)[\rho_{0m}\rho_{0i}(2V^2 - V_{\mathrm{A}i}^2 - V_{\mathrm{A}m}^2) + \rho_{0m}\rho_{0e}(2V^2 - V_{\mathrm{A}e}^2 - V_{\mathrm{A}m}^2)]\}$$
$$+ \pi k_e^2 a^2\{(a^2 - b^2)[\rho_{0i}\rho_{0e}(V^2 - V_{\mathrm{A}i}^2)(V^2 - V_{\mathrm{A}e}^2) - \rho_{0m}^2(V^2 - V_{\mathrm{A}m}^2)^2] + (a^2 + b^2)\rho_{0m}(V^2 - V_{\mathrm{A}m}^2) \times [\rho_{0e}(V^2 - V_{\mathrm{A}e}^2) - \rho_{0i}(V^2 - V_{\mathrm{A}i}^2)]\} = 0.$$

Here, V denotes the phase velocity of the FMS wave, ω/k_z.

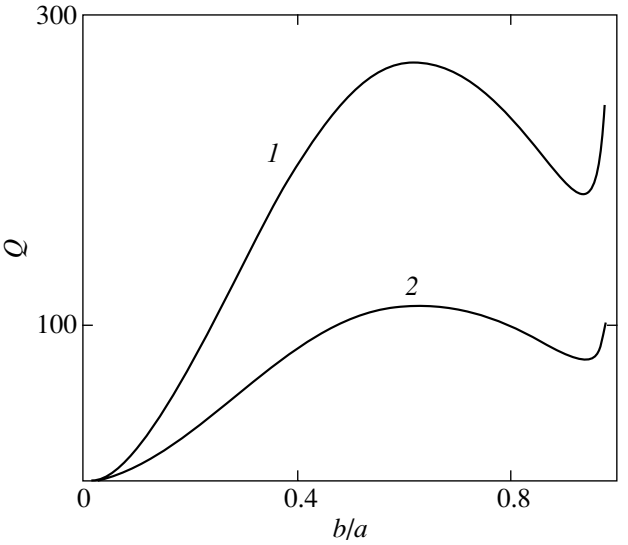

Fig. 3. Q factor of the tube oscillations on the radiated FMS mode versus ratio b/a: curve *1* for $b = 2000$ km and curve *2* for $b = 3100$ km.

We determined the Q factor for the following Alfvén speeds in the unperturbed media: $V_{\mathrm{A}e} = 0.7 \times 10^8$ cm s^{-1} in the external region, in agreement with observations (Nakariakov *et al.* 1999); and $V_{\mathrm{A}i} = 0.39 \times 10^8$ cm s^{-1} and $V_{\mathrm{A}m} = 3.5 \times 10^8$ cm s^{-1} in the cord and the shell, respectively. A factor of 5 difference between the Alfvén speeds in the shell and the surrounding space leads to a factor of 25 difference between the plasma densities; the density in the shell is lower than the density in the surrounding space by this factor. It is well known that the plasma density in solar loops can exceed the plasma density in the surrounding corona by as large as a factor of 8 to 18 (Aschwanden 2001). We assume that the density in the shell could be lower by the same factor. For the longitudinal wave number $k_z = \pi/L$ of the oscillations observed in a loop of length $L = 130\,000$ km with a period of $T = 256$ s (Nakariakov

et al. 1999), $k_z = 0.024 \times 10^{-8}$ cm^{-1}; for the phase velocity of the observed oscillations, we then obtain $V = 1.02 \times 10^8$ cm s^{-1}. At the chosen Alfvén speeds, the radiation condition for the slow mode is not satisfied; in the conditions under consideration, the slow mode is trapped by the cord. The Q factor of the oscillations on the fast mode for $b = 3100$ km and $a = 129\,000$ km is $Q \approx 40$ (Fig. 3). This value is equal in order of magnitude to the Q factors estimated from observations; we may at least assert that the radiation of MHD waves by the loop into the surrounding corona contributes significantly to the damping of its oscillations.

DISCUSSION

We have considered the propagation of MHD waves within a coronal loop in the form of a two-part magnetic flux tube in the approximation of ideal plasma. The loop consists of a dense hot cylindrical cord surrounded by a rarefied concentric shell. The plasma and the magnetic field are assumed to be uniform in the cord, the shell, and the surroundings of the tube. This model, which incorporates the radial loop inhomogeneity, is more realistic than the commonly used model of a uniform tube and allows us to successfully describe several interesting physical effects observed in the solar corona.

There are two slow magnetosonic waves on the $m = 0$ cylindrical mode within a thin magnetic flux tube with a shell that propagate along the tube with velocities close to the tube velocities in the cord and the shell. One of them is trapped by the cord (i.e., is a bulk wave in the cord and a surface wave in the shell), while the other is trapped by the shell. In the second wave, the plasma oscillations in the cord and the shell differ in phase by half the period.

There are two fast magnetosonic waves on the cylindrical modes with $m > 0$. If the Alfvén speed in the shell is lower than the Alfvén speed in the surrounding corona, i.e., if the shell is denser than the corona surrounding the loop, then both waves are trapped by the tube. If the Alfvén speed in the shell is lower than the Alfvén speed in the cord, then at least one wave is trapped by the shell and propagates only inside the shell; the second wave is trapped by the shell if condition (20) is satisfied. A characteristic property of these waves is that the plasma in the cord and the shell oscillates with opposite phases. If the Alfvén speed in the shell is higher than the Alfvén speed in the surrounding corona, i.e., if the shell is rarefied compared to the corona, then the faster wave is radiated outward. The slower wave can also be radiated if condition (19) is satisfied. For the radiated waves, the oscillations are also shifted in phase by half the period.

Our model of a coronal loop offers a new theoretical interpretation of several physical effects observed in the solar corona.

First, the presence of two slow magnetosonic waves allows us to interpret the phenomenon described by Robbrecht *et al.* (2001)—the simultaneous propagation of the regions of enhanced intensity along the loop with similar velocities (95 and 110 km s^{-1})—as a manifestation of the above two oscillation modes.

Second, the antiphase radio pulsations with a period of 1.5 s detected by Qin *et al.* (1996) at two wavelengths, 9.375 GHz (optically thick source) and 15 GHz (optically thin source), can be explained by the fact that they are modulated by the cord and shell oscillations with opposite phases. The radial loop oscillation period on the $m = 0$ mode can be estimated from the loop radius a and the Alfvén speed V_A; it is $a/V_A \approx 1$ s, in agreement with observations.

Third, the radiative properties of a loop with a shell differ significantly from those of a uniform loop. The fast magnetosonic wave radiated into the surrounding space ensures effective radiative damping of the system oscillations even in the absence of viscosity (Solov'ev *et al.* 2002, 2003).

ACKNOWLEDGMENTS

This work was supported by the Russian Foundation for Basic Research (project no. 02-02-16156).

REFERENCES

1. M. J. Aschwanden, Astrophys. J. **560**, 1035 (2001).
2. M. J. Aschwanden, L. Fletcher, C. J. Schrijver, *et al.*, Astrophys. J. **520**, 880 (1999).
3. P. M. Edwin and B. Roberts, Sol. Phys. **88**, 179 (1982).
4. Yu. G. Kopylova, A. V. Stepanov, and Yu. T. Tsap, Pis'ma Astron. Zh. **28**, 870 (2002) [Astron. Lett. **28**, 783 (2002)].
5. B. I. Meerson, P. V. Sasorov, and A. V. Stepanov, Sol. Phys. **58**, 165 (1978).
6. I. De Moortel, J. Ireland, and R. W. Walsh, Astron. Astrophys. **355**, L23 (2000).
7. I. De Moortel, J. Ireland, A. W. Hood, and R. W. Walsh, Astron. Astrophys. **387**, L13 (2002).
8. V. M. Nakariakov, L. Ofman, and E. E. DeLuca, Science **285**, 862 (1999).
9. V. M. Nakariakov, E. Verwichte, D. Berghmans, and E. Robbrecht, Astron. Astrophys. **362**, 1151 (2000).
10. Z. Qin, C. Li, Q. Fu, and Z. Gao, Sol. Phys. **163**, 383 (1996).
11. E. Robbrecht, E. Verwichte, D. Berghmans, *et al.*, Astron. Astrophys. **370**, 591 (2001).
12. B. Roberts, P. M. Edwin, and A. O. Benz, Astrophys. J. **279**, 857 (1984).

13. M. S. Ruderman and B. Roberts, Astrophys. J. **577**, 475 (2002).
14. A. A. Solov'eva, B. B. Mikhalyaev, and E. A. Kirichek, Fiz. Plazmy **28**, 758 (2002).
15. A. A. Solov'eva, B. B. Mikhalyaev, and E. A. Kirichek, Fiz. Plazmy **29**, 1130 (2003).
16. H. S. Spruit, Sol. Phys. **75**, 3 (1982).
17. H. Stenuit, R. Keppens, and M. Goossens, Astron. Astrophys. **331**, 392 (1998).
18. H. Stenuit, W. J. Tirry, R. Keppens, and M. Goossens, Astron. Astrophys. **342**, 863 (1999).
19. D. Tsiklauri and V. M. Nakariakov, Astron. Astrophys. **379**, 1106 (2001).
20. P. R. Wilson, Astron. Astrophys. **87**, 21 (1980).
21. V. V. Zaitsev and A. V. Stepanov, Pis'ma Astron. Zh. **8**, 248 (1982) [Sov. Astron. Lett. **8**, 132 (1982)].
22. V. V. Zaĭtsev and A. V. Stepanov, Pis'ma Astron. Zh. **15**, 154 (1989) [Sov. Astron. Lett. **15**, 66 (1989)].

Translated by V. Astakhov

Astronomy Letters, Vol. 30, No. 4, 2004, pp. 276–281. Translated from Pis'ma v Astronomicheskiĭ Zhurnal, Vol. 30, No. 4, 2004, pp. 315–320.

A High-Resolution Study of Jupiter at a Frequency of 30 GHz

Yu. N. Parijskij[1*], N. N. Bursov[1], A. B. Berlin[2], N. A. Nizhelskii[1], M. G. Mingaliev[1], P. A. Tsybulev[1], A. V. Bogdantsov[1], E. K. Majorova[1], O. M. Pilipenko[3], A. A. Balanovskii[1], and G. V. Zhekanis[1]

[1]*Special Astrophysical Observatory, Russian Academy of Sciences, Nizhniĭ Arkhyz, Karachaevo-Cherkesskaya Republic, 357169 Russia*

[2]*Special Astrophysical Observatory, St. Petersburg Branch, Russian Academy of Sciences, Pulkovo, St. Petersburg, 196140 Russia*

[3]*Saturn Research and Production Association, pr. Pyatidesyatiletiya Oktyabrya 2-b, Kiev, 148 Ukraine*

Received July 1, 2003

Abstract—We present the results of our study of Jupiter and its radiation belts with a resolution of 6 arcsec at a frequency of 30 GHz using the RATAN-600 radio telescope and a MARS matrix radiometer with a sensitivity of about 6 mK $s^{-1/2}$. We monitored the integrated emission from the Jovian disk with a signal-to-noise ratio of more than 1000 for 30 days and showed its radio emission to be highly stable ($\approx$1%). Based on daily data for the one-dimensional radio brightness distribution over the disk, we mapped the longitudinal radio brightness distribution over 100 rotation periods of Jupiter around its axis. Neither hot nor cold spots with a temperature contrast of more than 1 K were detected; their contribution to the total radio flux from the Jovian disk was no more than 0.2%. The one-dimensional latitudinal (longitude-averaged) distribution obtained on VLA with a similar resolution is shown to be an order of magnitude less uniform than the one-dimensional longitudinal (latitude-averaged) distribution obtained on RATAN-600. We have studied the radiation belts at such high frequencies for the first time and estimated their intensities and variability levels under the effect of external factors. The variable component of the radiation belts was shown to have not exceeded 0.5% of the integrated spectrum of Jupiter over the entire period of its observations. We estimated the contribution of the Galilean satellites ("Galilean noise") in low-resolution observations; the accuracy of allowing for this noise is determined by the accuracy of estimating the temperatures of the satellites at the observing frequency. The uncertainty in the total flux does not exceed 0.1%. © *2004 MAIK "Nauka/Interperiodica".*

Key words: *Jupiter, radiation belts.*

INTRODUCTION

Improvements in the quality of the RATAN-600 surface, the introduction of a new, higher-precision control system of the radio telescope, and the mounting at the focus of the first version of a matrix radiometer at the limiting wavelength of the design range (1 cm) have allowed the radio brightness distribution over the disk of Jupiter to be studied with a resolution close to that achieved on VLA at a wavelength of 2 cm (de Pater *et al*. 2001). The goal of the observations was to separate the radio emission components at the shortest wavelength to date (the disk, the atmospheric features, and the radiation belts) and to obtain data on the stability of their emission on timescales comparable to the rotation period of Jupiter around its axis. The observations were carried out on the initiative of the Planck Surveyor Mission group (Denmark) in connection with a discussion of the possibility of using Jupiter as a reference source at wavelengths of 1 cm or shorter when studying the beams of spaceborne radio telescopes. Observations of Jupiter with high angular and time resolutions at short centimeter wavelengths are also of considerable interest in the physics of this planet, including the establishment of the role of nonstationary dust injections that lead to a redistribution of the relative roles of ammonia and water clouds and the determination of the acceleration efficiency of solar-wind cosmic rays (CRs) in the Jovian magnetosphere. The higher the frequencies at which the Jovian radiation belts are observed, the greater the requirements on the acceleration mechanisms of the primary, fairly soft CRs in the solar wind. Whereas at decimeter wavelengths the problem of their acceleration is rather simple, at 1 cm a highly efficient mechanism that increases their

*E-mail: par@sao.ru

energy by two orders of magnitude is needed (de Pater *et al.* 2001).

OBSERVATIONS

The observations were carried out on the northern sector of RATAN-600 (Khaikin *et al.* 1972; Korol'kov and Parijskij 1979) with an aperture of about 450 m using a working model of the MARS-2 (MAtrix Radiometer System) matrix radiometer at a wavelength of 1 cm, an upgraded version of the MARS-1 (see Berlin *et al.* 2000). The resolution of the radio telescope at this wavelength is about 6 arcsec, which allowed us to obtain more than 15 independent points in the brightness distribution over the Jovian disk near the conjunction of Jupiter with Earth and to separate the disk emission from the radiation belts and the stationary emission of the Jovian atmosphere from isolated hot or cold spots on it (such as the Great Red Spot). We used three microwave channels of the matrix radiometer, each having two waveguide inputs for scanning or switching to a reference channel. The central radiometer was used in the single-horn mode with switching to the sky-looking horn, while the other two radiometers were used in the scanning mode with a beam separation of $\approx 20''$. The observations were carried out from December 10 through December 14, 2002, and from February 10 through March 10, 2003, in the standard mode of source drift through the radio telescope beam at the meridian. Each day, we recorded five drift curves at 1 cm (one with the central radiometer, two with the eastern radiometer, and two with the western radiometer in the scanning mode). Thus, we obtained about 200 one-dimensional radio images of the planet. The sensitivity of each channel was ≈ 6 mK $s^{-1/2}$, which allowed us to obtain information on the flux density from the planetary disk with a signal-to-noise ratio of more than 1000 for a single observation in one channel. For more detailed information about RATAN-600 and the MARS matrix radiometer, see the webpage of the Special Astrophysical Observatory, Russian Academy of Sciences, http://www.sao.ru. The two-dimensional RATAN-600 beam for the mode observations used was computed using new algorithms that showed close agreement with the experiment (Majorova and Trushkin 2002). We also used the reference object 3C 454.3 at a declination close to Jupiter to control the timing of the records and the beam size. This object was disregarded during flux density calibration, because it was variable. The daily measured antenna temperature was controlled on the temperature scale using a highly stable internal reference signal. The stability of this reference signal in the radiometers was additionally controlled by special algorithms. We also used the archive of the RATAN-600 automatic control system to allow for the actual errors in the RATAN-600 aperture by a simple correction for the losses on the surface elements that were not used in the aperture. This correction did not exceed 1–2%. We did not attempt to make absolute flux density measurements. Absorption variations in the Earth's atmosphere could be the major sensitivity-limiting factor. However, the achieved accuracy proved to be sufficient for our main task of revealing the effect of spatial variations in the brightness temperature of the Jovian atmosphere on the disk-averaged temperature of the planet's side facing the observer as well as for the first estimation of the contribution of the radiation belts to the total radio flux from Jupiter at such a short wavelength. Moreover, our method of establishing the role of small-scale radio brightness variations over the Jovian disk essentially requires no absolute measurements. It suffices to estimate (or set an upper limit on) their amplitude normalized to the antenna temperature at the center of the disk.

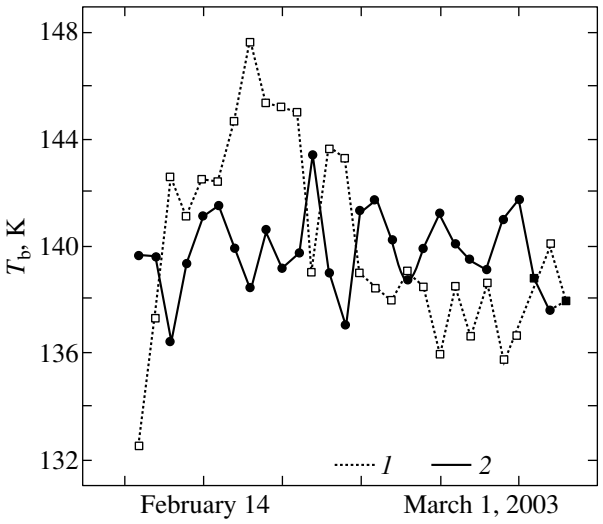

Fig. 1. Effective temperature of the Jovian disk on each day from February 10 through March 10, 2003, before (*1*) and after (*2*) the removal of the "monthly" component. The dispersion decreased from 2.6 to 1%.

RESULTS

All of the drift curves of Jupiter through the RATAN-600 beam in the single-horn mode reveal the disk (strip-integrated because of the knife-edge beam shape near the central cross section) and weak emission (at a 1.5% level of the antenna temperature at the center) outside the disk. The disk emission is easily separated due to the high resolution.

The formal rms deviation from the mean throughout the observations was 2.6%. The main contribution comes from the monthly (more precisely,

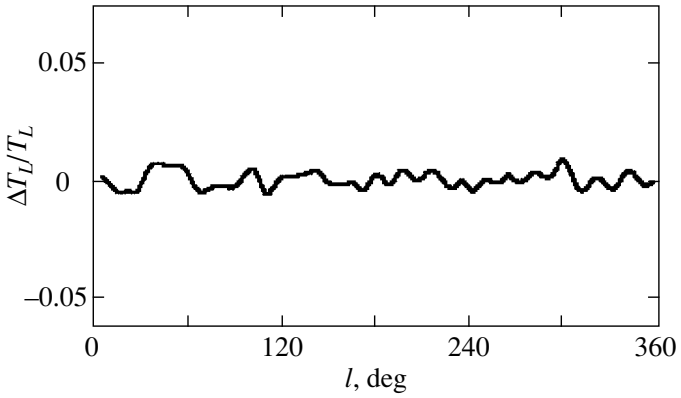

Fig. 2. The first attempt to reconstruct the complete longitudinal radio brightness distribution over the Jovian disk in the interval $0° < l < 360°$ from the data spanning a large number of days. The disk brightness variations strip-integrated over latitude are along the vertical axis.

27 days) period that is equal to the solar rotation period. However, the temperature variation of the ambient medium exhibits a similar pattern of variation with time. The latter, in turn, can be reflected on the absorption in the Earth's atmosphere whose water content changes when passing through its zero temperature. Longer-duration studies are required to elucidate the nature of the large-scale (in time) variation of the temperature at the disk center. Here, we restricted our analysis to estimating the stability of the emission from Jupiter on short timescales comparable to one day and determined mainly by its axial rotation. Having removed the variations on timescales longer than one week, we found that the flux density from the Jovian disk was stable to within 1.6%, and that the difference in the antenna temperatures between adjacent days in stable periods of clear cold weather did not exceed 1%.

Figure 1 shows the variations in effective disk temperature over the entire period and from day to day after the removal of all harmonics with periods longer than one day. The absolute value of the observing-period-averaged effective temperature of the disk was taken from the survey data by de Pater and Dickel (1986).

Since Jupiter rotates with a period of 9 h 55 min, different parts of the Jovian atmosphere face the Earth on each day, and we can estimate the extent to which the 1-cm flux from the Jovian atmosphere averaged over the longitude intervals facing the observer is constant even from Fig. 1.

Using the high resolution of the radio telescope, we attempted to estimate the contribution from possible bright and dark spots on the disk of Jupiter with a contrast of more than 1–2 K. As is well known, the northern and southern latitude belts in the Jovian atmosphere were detected at centimeter wavelengths with a contrast of 10–30 K in 1986 (see, e.g., de Pater and Dickel 1986). These data were obtained on VLA with a resolution close to the RATAN-600 resolution, but at longer wavelengths (2–6 cm). The latitudinal radio temperature distribution was averaged over a broad longitude interval in connection with the standard image synthesis technique used in studying Jupiter at a number of hour angles over 8 h, which is comparable to the rotation period of Jupiter. Therefore, the latitudinal radio brightness distribution is averaged (strip-integrated over all Jovian longitudes; see, e.g., de Pater and Dickel 1986). RATAN-600 makes it possible to obtain the longitudinal radio brightness distribution almost instantaneously, in 3 s, but averaged (strip-integrated) over the latitude, because of the knife-edge beam. Indeed, although the rotation axis of Jupiter during the observations deviated from the north–south direction by several degrees, given the finite resolution of the radio telescope (6 arcsec), we recorded the Jovian emission averaged over all latitudes. The tilt of the axis resulted in a loss of resolution: at each latitude, slightly different longitudes fell within the beam.

We searched for bright (dark) spots using the Mexican Hat technique. This is one of the most simple and efficient techniques for separating small-size features against an irregular background. In essence, it suffices to obtain the second derivative of the one-dimensional drift curve. For our purposes, this technique is particularly efficient, because the second derivative completely eliminates the main stable part of the radio brightness distribution over the Jovian disk whose strip integration is a second-order curve (half-ellipse) with a high accuracy, and only the constant part remains after double differentiation . Given the finite resolution, the interval $+30° < l < -30°$ from the central meridian proved to be accessible to daily studies with a relative temperature resolution of no less than 1% (1.5 K). We managed to double this

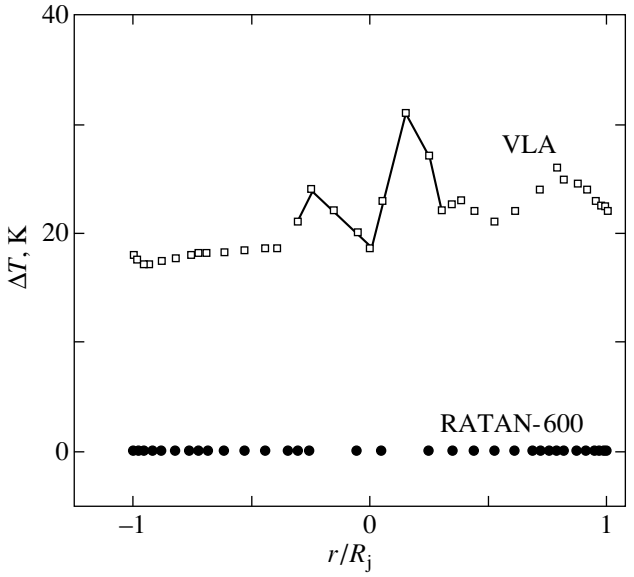

Fig. 3. Comparison of the RATAN-600 data on the longitudinal (strip-integrated over latitude) radio brightness distribution with the 2-cm VLA data on the latitudinal (strip-integrated over longitude) radio brightness distribution.

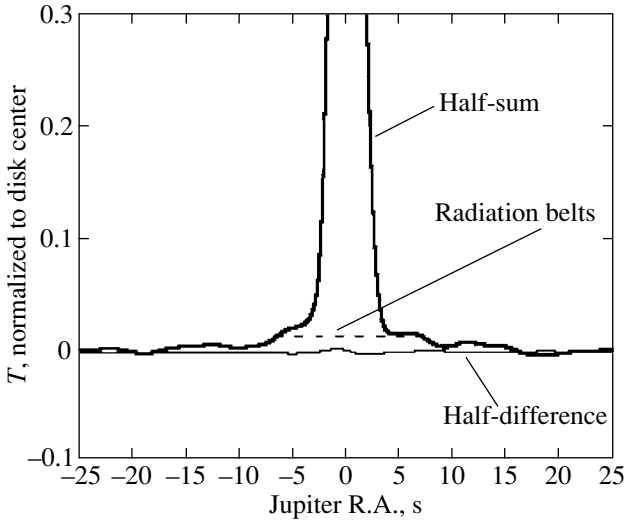

Fig. 4. Sum and difference of the two sets of observations in February–March 2003. The dashed line indicates the region near the disk where the emission from the radiation belts is noticeable.

accuracy by repeating the frames, on average, four times over the observing period. The observations spanning many days enabled us to reconstruct the longitudinal brightness distribution at all longitudes from 0° to 360° and to reveal features with a size of about 0.1 of the Jovian disk (which is close to the size of the Great Red Spot), but at radio wavelengths.

Having processed the data for all the days of our observations and having plotted the second derivatives on the same figure, we found that the region near the central meridian was not distorted by edge effects where the elliptical law of the strip-integrated disk emission was violated, and about half of the disk could be used with confidence to search for bright (dark) features on each day. The dispersion on the Jovian disk turned out to be virtually the same as the dispersion outside the disk and the radiation belts. This suggests that the small-scale variations in radio brightness increase the radiometer noise only slightly and are much smaller than 0.1%. Throughout the observations, we detected features with an amplitude above 3σ only twice, but they were not repeated in the subsequent maps of the same longitude intervals. In any case, the contribution of such features to the total radio flux from Jupiter is much less than 0.05%. Our main conclusion is as follows: the longitudinal (strip-integrated over latitude) radio brightness distribution at 1 cm obtained on RATAN-600 is much more uniform than the latitudinal (strip-integrated over longitude) distribution obtained on VLA (de Pater *et al.* 2001), as shown by Figs. 2 and 3.

Concurrently, we showed that the longitudinal variations of microwave cloud belts detected on VLA are small and do not exceed 1–3 K.

The Jovian radiation belts emit weak radiation at short centimeter wavelengths; the shorter the wavelength, the smaller their contribution to the total radio flux from Jupiter: the flux density from the disk increases as the square of the frequency, while the flux density from the radiation belts decreases with frequency (Bolton *et al.* 2002). As is well known, in several cases, a strip-integrated image allows the contribution of the weak diffuse emission near a bright object to be estimated more accurately than does a two-dimensional aperture-synthesis image. To improve the accuracy, we selected about 24 high-quality daily drift curves and verified that the background under the Jovian disk seen in Fig. 4 is present on all drift curves. The difference between adjacent days and between the two 12-day sets of observations does not exceed the radiometer noise.

Thus, we may conclude that the background is stable for one month with an accuracy of ~5% of its value, i.e., with an accuracy of ~0.05% of the total flux from Jupiter, irrespective of its nature. The location of this background emission relative to the Jovian disk, its angular size, and its total flux density are consistent with its interpretation as the emission from the radiation belts studied at longer wavelengths (with linear extrapolation of the flux density using all of the measurements from 21 to 6 cm) (Bolton *et al.* 2002). Nevertheless, to elucidate the nature of this background, we must formally take into account

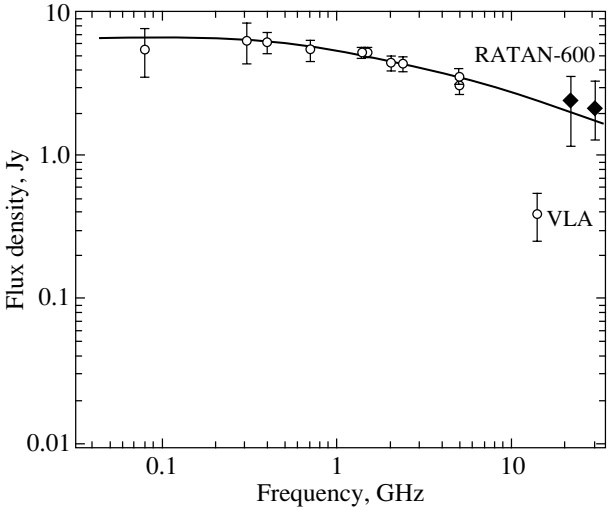

Fig. 5. Spectrum of the Jovian radiation belts as constructed from the data by de Pater *et al.* (2001) and Bolton *et al.* (2002) and new RATAN-600 data at 30 GHz (1 cm).

the contribution of instrumental scattering, which is present to some extent in any measurements. The structure of the instrumental background depends on the characteristic scales of the wavefront perturbations in the aperture of the radio telescope. Inaccurate focusing primarily leads to a large-scale quadratic error that increases the level of the nearest side lobes. This effect was checked on a reference object, and convolving its image with the Jovian disk yielded no observable background. The errors typical of multielement antennas that are related to the inaccurate positions of the reflecting elements give a Gaussian background with an angular scale of $\sim \lambda/a$, where a is the element width, equal to 2 m. The width of this background is an order of magnitude larger than the sizes of the radiation belts. Its contribution was also estimated from the scattering of the emission from the Moon. Finally, the main component of the observed scattered background near Jupiter has similar angular sizes at the different wavelengths (1.38, 2.7, 3.9, 7.6 cm) used in some of the observing periods, which conflicts with diffraction effects of any nature. The effects of atmospheric noise and random errors of the automatic control system are excluded, because the background shape and amplitude are repeatable on all of the observing days. We also studied the role of the Galilean noise due to the emission from the Galilean satellites with their total flux density close to 1 Jy, which accounts for almost 1% of the disk flux density. On each day, we computed a model drift curve of the satellites through the two-dimensional RATAN-600 beam and constructed their expected background on the average drift curve. However, this background is more than an order of magnitude weaker than that observed. The radio flux density at 1 cm outside the Jovian disk is ~2 Jy, and the spectrum of the radiation belts, including the data obtained in recent years, is shown in Fig. 5.

CONCLUSIONS

The emission from the Jovian atmosphere at a wavelength of 1 cm is fairly stable, and the radio flux density variations do not exceed 1–2% for its various orientations with respect to the observer. Many of these variations may be associated with the absorption variations in the Earth's atmosphere. Our study of the radio brightness distribution over the disk of Jupiter has shown that there are no hot or cold GRS-type spots with a temperature contrast of more than 1–3 K at a wavelength of 1 cm. This value is much lower than the contrast of the cloud (northern and southern) belts in the atmosphere of Jupiter, where it reaches 10–30 K (de Pater and Dickel 1986). The simplest explanation of the background emission near the Jovian disk, which extends to distances of up to three Jovian diameters, is the detection of radiation belts at 1 cm. These are the shortest-wavelength measurements of the radiation belts. In this interpretation, their spectrum agrees with the 6–31 cm data and, within the error limits, with the 3.8-cm data, but conflicts with the most recent 2-cm data (Bolton *et al.* 2002). The latter data have been obtained with incomplete filling of the UV plane, which usually results in an underestimation of the total flux density. Electrons with an energy of ≈100 MeV and the mechanisms responsible for their acceleration are required to explain the emission from the radiation belts at such short wavelengths. The matrix radiometer has proven to be efficient in studying the major planets. We plan to continue our study of Jupiter at short wavelengths on the basis of our experience in 2003 and using the polarization technique for separating the radiation belts.

ACKNOWLEDGMENTS

This work was supported in part by the Russian Foundation for Basic Research (project no. 02-02-17819) and the St. Petersburg Center of Science. Yu.N. Parijskij and N.N. Bursov wish to thank the administration of the Center for Theoretical Astrophysics of Denmark for providing technical facilities for data reduction and for some stimulating discussions.

REFERENCES

1. A. B. Berlin, G. M. Timopheeva, N. N. Nizhelsky, *et al.*, Astron. Astrophys. Trans. **19**, 559 (2000).
2. S. Bolton, M. Janssen, R. Thorn, *et al.*, Nature **415**, 987 (2002).
3. S. E. Khaikin, N. L. Kaidanovskii, Yu. N. Parijskij, and N. A. Esepkina, Izv. Glavn. Astron. Obs. Pulkovo **188**, 3 (1972).
4. D. V. Korolkov and Yu. N. Parijskij, Sky Telesc. **57**, 324 (1979); http://www.sao.ru.
5. E. K. Majorova and S. A. Trushkin, Bull. Spets. Astrofiz. Obs. **54**, 89 (2002).
6. I. de Pater, D. Dunn, P. Romani, and K. Zahnle, Icarus **149**, 66 (2001).
7. I. De Pater and J. Dickel, Astrophys. J. **308**, 459 (1986).
8. I. De Pater and J. Lissauer, *Planetary Science* (Cambridge Univ. Press, 2001), Vol. 330.

Translated by G. Rudnitskiĭ